

**543**

# **Guideline for Numerical Electromagnetic Analysis Method and its Application to Surge Phenomena**

**Working Group  
C4.501**

**June 2013**



# GUIDE FOR NUMERICAL ELECTROMAGNETIC ANALYSIS METHODS: APPLICATION TO SURGE PHENOMENA AND COMPARISON WITH CIRCUIT THEORY-BASED APPROACH

Cigré WG C4.501

## Members

A. Ametani, Convenor (JP), M. Paolone, Secretary (IT), K. Yamamoto, Secretary (JP), Prof. Maria Teresa Correia de Barros (PT), A. M. Haddad (UK), J.L. He (CN), M. Ishii (JP), T. Judendorfer (AT), W. Jung-Wook (KR), A. J. F. Keri (US), C. A. Nucci (IT), Dr. Marjan Popov (NL), F. Rachidi (CH), M. Rubinstein (CH), E. Shim (KR), J. Smajic (CH), K. Tanabe (JP), L. Tang (US), P. Yutthagowith (TH)

## Corresponding member

Y. Baba (JP)

## Copyright © 2013

“Ownership of a CIGRE publication, whether in paper form or on electronic support only infers right of use for personal purposes. Are prohibited, except if explicitly agreed by CIGRE, total or partial reproduction of the publication for use other than personal and transfer to a third party; hence circulation on any intranet or other company network is forbidden”.

## Disclaimer notice

“CIGRE gives no warranty or assurance about the contents of this publication, nor does it accept any responsibility, as to the accuracy or exhaustiveness of the information. All implied warranties and conditions are excluded to the maximum extent permitted by law”.



ISBN : 978-2-85873-237-1

# Guide for numerical electromagnetic analysis methods: application to surge phenomena and comparison with circuit theory-based approach

## Table of Contents

EXECUTIVE SUMMARY .....	5
1 INTRODUCTION .....	5
2 CIRCUIT THEORY-BASED APPROACHES: ADVANTAGES AND LIMITATIONS.....	6
2.1 Introduction.....	6
2.2 Example of Modelling Transients using EMTP .....	7
2.3 LIMITATIONS OF EMTP.....	10
2.3.1 Lightning current and impedance .....	10
2.3.2 AC source voltage .....	10
2.3.3 Tower models .....	11
2.3.3.1 Modelling problems of vertical earthed structures.....	11
2.3.3.2 Impedance and admittance formulas.....	12
2.3.3.3 Frequency-dependent effect of a tower.....	13
2.3.3.4 Influence of surge impedance and frequency-dependent effect.....	13
2.3.3.5 TEM propagation mode.....	14
2.3.4 Tower footing impedance.....	14
2.3.4.1 Linear footing impedance.....	14
2.3.4.2 Current-dependent nonlinearity .....	14
2.3.4.3 Non-uniform and frequency-dependent characteristics .....	14
2.3.5 Archon flashover model .....	14
2.3.6 Transmission lines, feeders, gas-insulated busses .....	15
2.3.6.1 Frequency-dependent transmission line impedance.....	15
2.3.6.2 Finite length of a line and a gas-insulated bus.....	16
2.3.6.3 Gantry tower feeding a substation – Inclined conductor.....	17
2.3.6.4 Stratified soil.....	18
2.3.6.5 Earth-return admittance .....	18
2.3.6.6 Complex permittivity .....	18
2.3.7 Corona wave deformation .....	18

2.3.8 Phase-to-phase lightning surge.....	20
2.4 Comparison of simulation results obtained by means of EMTP-type and NEA methods .....	20
2.4.1 Transient responses of a grounding electrode.....	20
2.4.2 Transient responses of a vertical earthed structure .....	21
2.4.3 Archon voltage during a back-flashover .....	23
2.5 Concluding Remarks .....	24
3 THEORY OF NUMERICAL ELECTROMAGNETIC ANALYSIS FOR TRANSIENTS .....	25
3.1 Introduction about the numerical electromagnetic analysis .....	25
3.1.1 Basic equations in electromagnetics.....	25
3.1.2 Classification of electromagnetic calculation techniques .....	29
3.2 Circuit-theory based approach and transmission line (TL) models .....	31
3.3 Numerical solution of Maxwell's differential equations .....	31
3.3.1 Finite-difference time-domain method (FDTD) .....	31
3.3.2 Transmission line matrix 'TLM' .....	37
3.3.3 Finite-element method in time domain (FEMTD).....	37
3.4 Integral equation based approach.....	43
3.4.1 Method of moment (MoM).....	43
3.4.2 Partial element equivalent circuit (PEEC) method.....	46
4 Specific characteristics of various methods .....	48
4.1 Absorbing boundary conditions of Finite Difference Time Domain (FDTD).....	48
4.2 Method of Moments (MoM).....	50
4.3 Partial Element Equivalent Circuit (PEEC) .....	52
4.3.1 Formulation of the quasi-static PEEC method in the time domain.....	53
4.3.2 Transmission Line Model (TLM) .....	54
4.4 On the representation of metallic conductors.....	55
4.5 On the representation of soil-ionization phenomena.....	56
5 Application examples.....	59
5.1 Surge characteristics of transmission towers.....	59
5.2 Surge characteristics of grounding electrodes.....	62
5.2.1 Vertical grounding rods .....	62
5.2.2 Horizontal grounding electrodes .....	64
5.2.3 Complex grounding configurations .....	66
5.3 Lightning surge calculation in substations .....	69
5.3.1 Air-Insulated Substations .....	69
5.3.2 Influence of grounding on lightning surge calculation in substations .....	70
5.4 Surge voltages on overhead lines .....	72
5.4.1 Lightning-induced surges on distribution lines computed by means of the MoM .....	72
5.4.2 LEMP and induced surges calculation by means of the FEMTD in overhead lines above a lossy ground .....	75
5.4.3 Influence of grounding on surge propagation in overhead transmission lines.....	80
5.5 Propagation characteristics of PLC signals along power coaxial cables .....	82
5.6 Lightning surge characteristics of a wind-turbine tower.....	83
5.7 Full-Maxwell 3D simulations of very fast transients (VTFs) in GIS.....	88
6 Representative simulation tools.....	92
6.1 Numerical Electromagnetic Code (NEC) .....	92
6.2 Virtual Surge Test Lab (VSTL).....	92

6.3 Parallel Finite Integral Transient Program (FIT3D-NOG/PFIT).....	92
6.4 Current Distribution, Electromagnetic Fields, Grounding and Soil Structure Analysis (CDEGS).....	92
6.5 XFDTD.....	92
6.6 MAGNA/TDM .....	92
6.7 Transmission Line Matrix (TLM) .....	92
6.8 COMSOL (FEM).....	93
6.9 Power Lines Lightning Performance Analysis Software (PLLP) .....	93
6.10 Power System Grounding Analysis Software (PSGAS) .....	93
6.11 Sigma Slp.....	93
7 Conclusion .....	93
8 Bibliography/References.....	94

## EXECUTIVE SUMMARY

The aim of this document is to provide an extended description and application guide of methods belonging to the so-called Numerical Electromagnetic Analysis (NEA) applied to the calculation of electromagnetic transients in power systems.

As known, the accurate computation of electromagnetic transients is a fundamental requirement of several studies in the area of power systems. Lightning and switching studies are, for instance, typical subjects where the accuracy of transient's computation has a direct influence to the proper sizing of components like insulators and breakers. Traditional approaches adopted since now were based on the combination of circuit and transmission lines theories. These approaches, analytically and numerically validated by numerous contributions to the literature, rely on specific assumptions that are inherently relaxed by NEA methods. Indeed, NEA methods mostly rely on the numerical solution of the full-wave Maxwell's equations and, in this respect, the assessment of their accuracy, as well as the description of the various numerical methodologies, have motivated the preparation of this Technical Brochure.

In this context, this guide will first discuss the general aspects and limitations associated to classical circuit and transmission lines theories. In particular, the guide will make reference to the modelling approaches used to represent the most typical power system components, like transmission lines, grounding systems, towers etc., within EMTP-like simulation tools (Electromagnetic Transient Program). A first comparison with the most typical NEA methods is presented in order to discuss the main differences and better support the contents of this guide.

Then, the guide focuses on the analytical formulation of the most used NEA methods like, the Finite-Difference Time-Domain (FDTD), the Transmission Line Matrix 'TLM', the Finite-Element Method in Time Domain (FEMTD), the Method of Moment (MoM) and the Partial Element Equivalent Circuit (PEEC) method.

A further remark refers to the comparative analysis of NEA vs EMTP-like simulation approaches. Such an assessment, addressed in this document in various sections, aims at stressing the advantages and drawbacks of both methods. Indeed, NEA methods, although characterized, in general, by better accuracies, result into non-negligible computation times that require the availability of specific computation environments. Such a characteristic is due to the inherent numerical complexity of NEA solvers that require the treatment of large amount of data that, additionally, have an influence on the results accuracy. To this end, the last part of the guide refers to the benchmarking of the various NEA methods by means of typical test cases. In this respect, the members of the Cigré WG C4.501 agreed to include a specific section of the brochure aimed at providing the NEA-computed electromagnetic transients with reference to the most typical test cases like: (i) lightning surge calculation in substations, (ii) influence of grounding on lightning surge calculation in substations, (iii) surge voltages on overhead lines, (iv) lightning-induced surges on distribution lines, (v) LEMP and induced surges calculation in overhead lines above a lossy ground and (vi) simulations of very fast transients (VTFs) in GIS. Additionally, as NEA methods represent power tools for the computation of parameters of power systems components, the guide has also provided benchmarking examples for the following assessments: (a.) surge characteristics of transmission towers, (b.) surge characteristics of grounding electrodes, vertical grounding rods, horizontal grounding electrode and complex grounding configurations, (c.) influence of grounding on surge propagation in overhead transmission lines, (d.) propagation characteristics of PLC signals along power coaxial cables, (e.) lightning surge characteristics of wind-turbine towers.

## 1 INTRODUCTION

Full-wave numerical electromagnetic analysis methods (henceforth called NEA) allow the direct numerical solution of Maxwell's equations either in frequency or in time domains. These methods are becoming a promising approach for the numerical solution of complex transient phenomena that cannot be straightforwardly solved by means of circuit-theory-based<sup>1</sup> simulation tools such as the Electromagnetic Transient Program (EMTP). Indeed, circuit-theory based approaches cannot, in principle, solve transients that involve non-TEM propagation modes. Typical

---

<sup>1</sup> Throughout this document, we consider the term 'circuit-theory approach' in a general sense that includes the transmission line theory.

examples are transients associated with a direct lightning strike to a vertical earthed structure, or transients across a transmission line archorn . Additionally, circuit-theory based approaches present major difficulties for the solution of transients in complex media (e.g. grounding electrode, cables semi-conducting layers, etc.). Finally, it is worth noting that circuit-theory approaches require the prior knowledge of the circuit parameters that are often hard to estimate. On the other hands, NEA methods are inherently solving this problem although require major computational efforts and a non-straightforward definition of both sources and boundary conditions.

The aim of this document is twofold: (1) to present a critical assessment of existing modelling methods of power system components obtained by using conventional circuit-theory based approaches, and (2) to describe the theory of NEA and its application to the analysis of transient surges in power systems.

The document is organized as follows.

- Chapter 2 presents a general overview of the circuit theory-based approach, discussing its validity and limitations. In particular, examples of modeling methods using EMTP are described and reference is made to experimental data.
- Chapter 3 describes the theory of numerical electromagnetic analysis method for electromagnetic transients. The basis of the method is outlined first, and various NEA methods are categorized and described.
- In chapter 4, specific characteristics of various NEA methods are discussed. Special emphasis is devoted to the effect of cell size, time step, and absorbing boundary conditions on the accuracy of the results.
- In Chapter 5, representative applications of numerical electromagnetic computation methods to analysing surges are reviewed.
- Chapter 6 reports on some representative simulation tools of NEA methods.
- Finally, Chapter 7 presents a summary and conclusions.

## 2 CIRCUIT THEORY-BASED APPROACHES: ADVANTAGES AND LIMITATIONS

This chapter presents an overview of circuit theory approaches, emphasizing their advantages and limitations, with special reference to the Electromagnetic Transients Program (EMTP). A comparative analysis between simulation results obtained by circuit theory-based approach and numerical electromagnetic analysis is presented and discussed.

### 2.1 Introduction

For the last 30 years, the electromagnetic transients program (EMTP) originally developed by the Bonneville Power Administration, US Department of Energy [1, 2], has been considered to be the most powerful tool to carry out a predictive calculation of lightning overvoltages for insulation design and coordination of both substations and transmission lines. However, it is well known that EMTP is based on the circuit theory<sup>2</sup> that is based on a number of assumptions among which the TEM wave propagation. In addition, it requires the prior knowledge of circuit parameters [3].

Examples of transients involving non-TEM propagation modes include: (i) digital control circuits (quite common in power stations/substations as well as intelligent buildings) coupled with electromagnetic disturbances originated by lightning and switching manoeuvres [4]; (ii) travelling wave propagation of a partial discharge on a gas-insulated bus involving [5]; (iii) archorn flashover on a transmission tower [6]. These phenomena involve non-TEM propagation mode in a very high frequency range, and cannot be analysed by a conventional circuit theory-based approach such as EMTP. In view of the above, numerical electromagnetic analysis methods are becoming an alternative and effective approach to analyse transients involving non-TEM propagation [7, 8].

---

<sup>2</sup> Again, it is worth repeating that circuit theory should be considered in this document in the general sense, including transmission line theory.

This chapter describes modelling methods and related problems of EMTP and discusses the limitations of EMTP – and, in general, circuit codes - for transient surge analysis. Simulation examples by EMTP and a numerical electromagnetic analysis method are also presented and relevant differences between the results discussed.

## 2.2 Example of Modelling Transients using EMTP

This section aims at illustrating a typical modeling methodology for the calculation of lightning surges due to a direct lightning strike of overhead transmission lines by using EMTP.

As an example, Figure 2.1 shows the typical model configuration of a transmission line for lightning surge simulations performed by using EMTP (adapted from typical model representation suggested in Japan [3]) [9-12].

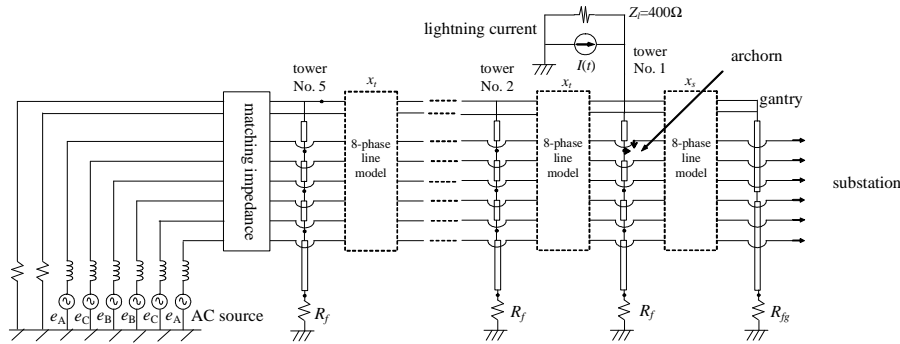


**Figure 2.1: Simplified illustration of the recommended model system for a lightning surge simulation. Adapted from [3]**

*Number of towers:* five towers from a substation gantry are typically considered as travelling waves reflected from the different towers are capable of affecting the lightning surge voltages at the substation location (see Figure 2.1). The maximum time that corresponds to this first reflection can be estimated as follows: when lightning strikes the first tower at  $t=0$ , the reflected surge from the last tower arrives at the substation entrance after two travel times  $T$  corresponding to the distance between the first and the last tower. (For example, a distance  $x_t = 300$  m corresponds to the time  $T \approx 10 \mu s$  (assuming a propagation at the speed of light). Thus, a simulation result is accurate up to  $10 \mu s$ , which is enough in general to observe the maximum overvoltage and the time to the peak.)

*Line terminations:* the left side of the last tower is represented by a multiphase matching impedance, which is calculated as the characteristic impedance matrix including the mutual impedance of the transmission line at the dominant transient frequency  $f_t$  defined by [13]:

$$\begin{aligned} f_t &= 1/4\tau : \text{open-circuited line} \\ &= 1/2\tau : \text{short-circuited line} \\ &\approx 1/3\tau : \text{matching termination line} \end{aligned} \tag{2.1}$$

where  $\tau = x_0/c$ ,  $x_0 = 5x_t + x_s$  : total line length

An AC voltage source is connected to the other side of the matching impedance as illustrated in Figure 2.1 to take into account the effect of the AC steady state voltage on the lightning surges.

*Lightning current and lightning channel impedance:* the lightning current is represented by a current source in parallel with an impedance representing the lightning channel. The source is characterized by the following typical parameters: wave-front duration  $T_f = 1 \mu s$  and a wave-tail  $T_r = 70 \mu s$ . Occasionally a concave current of which the waveform is defined in the following equation is adopted to represent a real lightning current more accurately [14, 15].



$$I(t) = \{1 - \cos(\omega t)\} \text{ for } t \leq T_f \quad (2.2)$$

= linearly decreasing function for  $t > T_f$

where  $I_0$ : peak current,  $\omega = \pi/2T_f$ , i.e.  $f = 1/4T_f$

It is worth mentioning that other possible representations of the lightning current waveshape are possible by using the so-called Heidler function [16].

Typical values of lightning current amplitudes are given in Table 2.1 for various transmission voltages [15].

The impedance of the lightning channel, derived by Bewley in [17], is typically assumed equal to  $400 \, \Omega$  [14] although higher values (in the order of  $1 \, \text{k}\Omega$ ) are usually used in Cigré, IEEE and IEC standards.

**Tower and gantry:** a transmission tower is represented by four distributed-parameter lines [18] as illustrated in Figure 2.2, where

$Z_{t1}$ : tower top to the upper phase arm=upper to middle=middle to lower,

$Z_{t4}$ : tower to tower bottom

Table 2.1 gives typical values of the surge impedance.

The propagation velocity  $c$  of a traveling wave along a tower is assumed equal to:

$$c_0 = 300 \, \text{m}/\mu\text{s} : \text{light speed in free space} \quad (2.3)$$

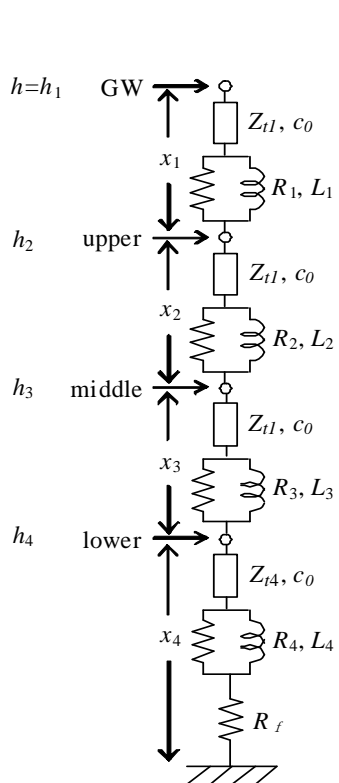


Figure 2.2: A model circuit of a tower

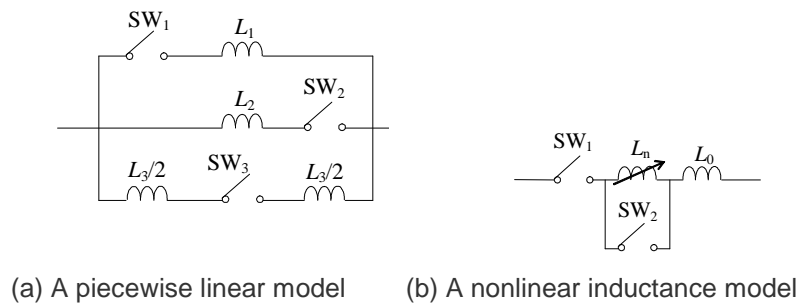


Figure 2.3: An archon flashover model

system voltage [kV]	lightning current [kA]	tower height / geometry [m]				surge imp. [Ω]		footing res. [Ω]
		$h$	$x_1$	$x_2$	$x_3$	$Z_{t1}$	$Z_{t4}$	$R_f$
1100	200	107	12.5	18.5	18.5	130	90	10
500	150	79.5	7.5	14.5	14.5	220	150	10
275	100	52.0	9.0	7.6	7.6	220	150	10
154(110)	60	45.8	6.2	4.3	4.3	220	150	10
77(66)	30, 40	28.0	3.5	4.0	3.5	220	150	10-20

Table no. 2.1: Recommended values of lightning parameters

To represent travelling wave attenuation and distortion, an  $RL$  parallel circuit is added to each part as illustrated in Figure 2.2. The values of the  $R$  and  $L$  are defined using the following expressions

$$\begin{aligned} R_i &= \Delta R_i \cdot x_i, L_i = 2\tau R_i \\ \Delta R_1 &= \Delta R_2 = \Delta R_3 = 2Z_{t1}\ln(1/\alpha_1)/(h-x_4) \\ \Delta R_4 &= 2Z_{t4}\ln(1/\alpha_1)/h \end{aligned} \quad (2.4)$$

where  $\tau = h/c_0$  : travelling time along the tower

$\alpha_1 = \alpha_4 = 0.89$  : attenuation along the tower

$h$  : tower height

The substation gantry is represented by a single lossless distributed line.

*Tower footing impedance*: the tower footing impedance, according to studies carried out in Japan [14], can be modeled as a simple linear resistance  $R_f$ , although a current-dependent nonlinear resistance is also taken into account by the IEEE and the CIGRE [9-12]. Examples of typical values of tower footing resistances for each voltage class are given in Table 2.1.

*Archorn flashover*: an archorn flashover is represented either by a piecewise linear inductance model with time controlled switches as illustrated in Figure 2.3(a) or by a nonlinear inductance in Figure 2.3(b) based on a leader progression model [19], [20]. The parameters  $L_i$  ( $i = 1$  to 3) and  $t_i - t_{i-1}$  assuming the initial time  $t_0 = 0$  in Figure 2.3(a) are determined from measured V-I characteristic of an archorn flashover. Then the first EMTP simulation with no archorn flashover is carried out and presented in Figure 2.1, and the first flashover phase and the initial time to close the switch for the phase are determined from the simulation results of the voltage waveforms across all the archorns. By adopting the above parameters, a second EMTP simulation only with the first phase flashover is carried out to determine the second flashover phase. By repeating the above procedure until no flashover occurs, a lightning surge simulation by the piecewise linear model is completed. Thus, a number of pre-calculations are necessary in the case of multiphase flashovers, while the nonlinear inductance model needs no pre-calculation and is easily applied to multiphase flashovers. The detail of the leader progression model is explained in [19], and that of the nonlinear inductance model in [20].

*Transmission line*: as transmission lines are composed by different conductors (both active conductors and shielding wires, e.g. twin-circuit vertical configuration with two ground wires), it is recommended to represent the line by a frequency-dependent EMTP model that takes into account all the line conductors. Reasonable approximations could also be obtained by using distributed-line models with a fixed propagation velocity, attenuation and surge impedance (i.e. fixed-parameter distributed-line model explained in Sec. 4.2.2.4 of [2]).

*Corona wave deformation*: although the representation of corona is taken into account in CIGRE and IEEE standards [9-12], it is usually neglected as the resulting wave deformation obtained by neglecting this phenomenon results into conservative overvoltages, except for the case of induced voltages (Reference to Nucci et al.).

*Surge arresters*: an inductance of a lead wire and the arrester itself is connected in series to the arrester model, because it affects a transient voltage and current of the arrester. Also, stray capacitance of the arrester should be considered, if necessary. To represent a very fast impulse characteristic of the arrester, an IEEE model [21] or a model of a nonlinear resistance with a nonlinear inductance [22] is occasionally adopted. The latter model takes into account the hysteresis of an arrester V-I characteristic by adding the nonlinear inductance to the nonlinear resistance in series. Other simplified models of surge arresters, suitable for insulation coordination studies and requiring less data, have been presented in the literature (e.g. [23]).

*Substation gas insulated bus and cable*: a cable and a gas-insulated bus are represented either as three single-phase distributed-parameter lines with relevant coaxial mode surge impedances and propagation velocities or as a

three-phase distributed-parameter lines. As gas-insulated substations involve, in general, a large number of gas-insulated buses/lines; the pipes are, in most cases, not considered by assuming their voltages being equal to zero.

*Circuit breaker, disconnecter, transformer, bushings:* circuit breakers (CB) and disconnectors are represented by lumped capacitances between the poles and the ground. Transformers are typically represented by phase-to-ground capacitances unless transferred surges to the secondary circuit are of interest. Also bushings are represented by capacitances and, occasionally, by using distributed parameters lines.

*Grounding mesh:* a grounding mesh is in general not considered in a lightning surge simulation, and it is assumed as a zero-potential surface. When dealing with an incoming surge to a low-voltage control circuit, the transient voltage of the grounding mesh should not be assumed zero, and its representation becomes an important and difficult subject (e.g. [24]).

## 2.3 LIMITATIONS OF EMTP

ElectroMagnetic Transient Programs (EMTP) is a family of simulation environments capable of providing time-domain numerical solutions of a given power system by using the electrical circuit theory based on an assumption of transverse electro-magnetic (TEM) mode of propagation. Thus, the EMTP-type cannot be straightforward used to simulate phenomenon associated with non-TEM propagation modes. Additionally, in these approaches the a-priori knowledge of circuit parameters and voltage/current forcing functions is required.

### 2.3.1 Lightning current and impedance

Advanced methodologies associated to measurements of lightning performances of power systems have shown that lightning current waveforms cannot be represented as simple double exponential and/or ramp waveforms [25], [26]. Unless a measured waveform or a specific waveform is given, the EMTP can not handle a lightning current.

The lumped lightning-path impedance (typically assumed equal to 400  $\Omega$ ) was derived by Bewley in [17]. However, such a value seems to be incorrect as the velocity of the lightning current wave-front is assumed equal to the speed of light in free space. On the contrary, Diesendorf suggested to modify this value in the range between 1000 to 2000  $\Omega$  [27]. On the other hand, there is a measured lightning current waveform which includes reflection of a current wave at a junction point of a lightning channel and a phase conductor of a UHV-designed line on the occasion of a shielding failure [28]. From the tower footing lightning current waveform in Figure 6 of this reference, the relative impedance of the lightning channel to that of a 8-conductor phase wire is known to be about 800 to 1200  $\Omega$  at the moment of about 100  $\mu$ s after the lightning strike.

### 2.3.2 AC source voltage

An AC source voltage is often neglected in a lightning surge simulation. However, it has been found that the ac source voltage affects archorn phase flashover especially in case of a rather small lightning current. Figure 2.4 shows a measured result of archorn flashover phases as a function of the AC source voltage on a 77 kV transmission line in Japan [29]. The measurements were carried out in two 77 kV substations by surge recorders installed in the substations. From the recorded voltages and currents, Figure 2.4 was obtained. The figure clearly shows that the archorn flashover phase is quite dependent on the AC source voltage, i.e. a flashover occurs at a phase of which the AC voltage is in the opposite polarity of a lightning current. Table 2.2 shows a simulation result of archorn peak voltages (archorn not operating) on (a) the 77kV line and (b) a 500kV line [30]. The simulation was carried out in using circuit similar to the one of Figure 2.1, but adding other five towers instead of the gantry and the substation.

The parameters are the same as those of Table 2.1 for a 77 kV system except the assumed 40 kA lightning current amplitude based on field measurement [29]. By comparing the results of the 500kV line with those on the 77kV line it is possible to observe that the lower phase archorn voltage is relatively smaller than the other phase archorn voltages. Thus, an archorn flashover phase on an EHV line is rather independent from the AC source voltage, and the lower phase flashover is less probable than the other phase flashover. On the contrary, flashover probability is rather the same on each phase and the relevant flashover is dependent on the AC source voltage of the phase characterized by the lower voltage value.

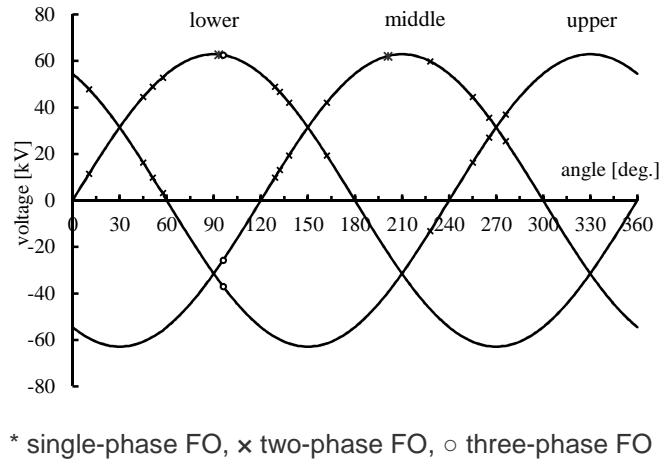


Figure 2.4: Measured results of archorn flashover phases on a 77kV transmission line

transmission voltage	maximum voltage [kV] / time of appearance [ $\mu$ s]	
	77kV	500kV
upper	873.0 / 1.012	4732 / 1.025
middle	820.2 / 1.024	4334 / 1.073
lower	720.0 / 1.035	3423 / 1.122

Table no. 2.2: Maximum archorn voltages and the time of appearance

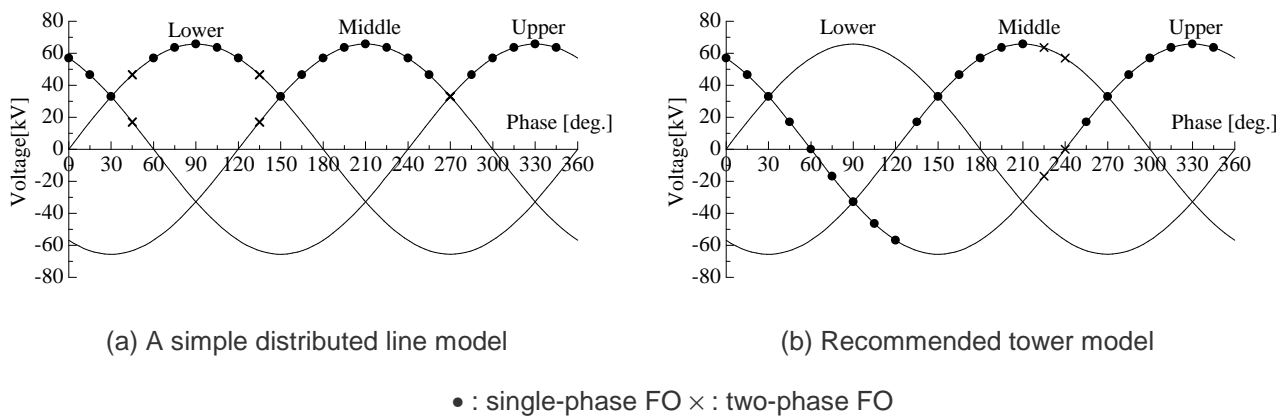


Figure 2.5: Simulation results of archorn flashover phases corresponding to Figure 2.5

### 2.3.3 Tower models

#### 2.3.3.1 Modelling problems of vertical earthed structures

This subsection briefly illustrates the problems related to the modelling of vertical earthed structures, with particular reference to transmission line towers, by making reference to the recommendations described in [14], [18].

Figure 2.5 shows simulation results of archorn flashover phases by a simple distributed line “tower model” i.e. neglecting the RL circuit in Figure 2.2 with the parameters in Table 2.1, and by the recommended model illustrated in Figure 2.2. The simulation circuit is the same as that described for Table 2.2 in the previous section. This figure

should be compared with the field test result shown in Figure 2.4. It is clear that the recommended model can not duplicate the field test result, while the simple distributed line model shows a good agreement with the field test result. The reason for the poor accuracy of the recommended model is that the model was developed originally for a 500kV line on which the lower phase flashover was less probable as explained in the previous section. Thus, the recommended tower model tends to result in lower flashover probability of the lower phase archorn. An  $R$ - $L$  parallel circuit between two distributed lines in Figure 2.2 represents travelling wave attenuation and distortion along a tower. The  $R$  and  $L$  values were determined originally based on a field measurement ( $\alpha$  in eq. (2.4)), and thus those are correct only for the tower on which the measurement was carried out. Sometimes, the  $R$ - $L$  circuit generates unreal high frequency oscillation. This indicated a necessity of further investigation of the  $R$ - $L$  circuit.

### 2.3.3.2 Impedance and admittance formulas

A number of tower models have been proposed, but most of them are not general, i.e. a tower model shows a good agreement with a specific case explained in the paper where the model is proposed. The following IEEE/CIGRE formula of the tower surge impedance is well-known and is widely adopted in a lightning surge simulation [10, 11].

$$Z_t = 60 \ln[\cot\{0.5 \tan^{-1}(R/h)\}] \quad (2.5)$$

where  $R = (r_1 h_1 + r_2 h + r_3 h_2)$  : equivalent radius of the tower represented by a truncated cone,  $h = h_1 + h_2$

$r_1, r_2, r_3$ : tower top, midsection and base radii [m]

$h_1$ : height from midsection to top [m]

$h_2$ : height from base to midsection [m]

When the tower is not a cone but a cylinder, then the above equation is rewritten by :

$$Z_t = 60 \ln(h/r) \quad (2.6)$$

where  $r$  : radius of a cylinder representing a tower

Ref.	height $h$ [m]	radius $r$ [mm]	measured $Z_{mes}$ [ $\Omega$ ]	Ametani Ref. [27]	Jordan <sup>*1</sup> Ref. [28]	Wagner <sup>*2</sup> Ref. [29]	Sargent <sup>*3</sup> Ref. [30]	Hara <sup>*4</sup> Ref. [31]
[31]	15.0	25.4	320.0	323.0	322.9	445.2	385.2	325.2
	15.0	2.5	459.0	462.0	462.0	584.4	524.4	464.4
	9.0	2.5	432.0	431.3	431.3	553.7	493.7	433.7
	6.0	2.5	424.0	407.0	407.0	529.4	469.4	409.4
	3.0	50.0	181.0	187.2	185.7	308.0	248.0	188.0
	3.0	25.0	235.0	228.0	227.2	349.6	289.6	229.6
	3.0	2.5	373.0	365.5	365.4	487.8	427.8	367.8
	2.0	2.5	345.0	341.2	341.1	463.5	403.5	343.5
[30]	0.608	43.375	112.0	104.7	98.4	220.8	160.8	100.8
	0.608	9.45	180.0	191.2	189.8	312.2	252.2	192.2
	0.608	3.1125	250.0	256.9	256.5	378.9	318.9	258.9
average of absolute error [%]				2.5	2.7	44.8	22.6	2.8

\*1 :  $Z_j = 60 \ln(h/r) - 60 = 60 \ln(h/er)$ , \*2 :  $Z_w = 60 \ln(2\sqrt{2}h/r) = Z_j + 122.4$ , \*3 :  $Z_s = Z_w - 60 = Z_j + 62.4$ , \*4 :  $Z_h = Z_w - 120 = Z_j + 2.4$

**Table no. 2.3: Measured and calculated surge impedances of vertical conductors**

Table 2.3 compares various tower models (surge impedance) with measured results [31]. As is clear from the average error to the measured results given at the bottom of the table, Ametani's formula shows the highest accuracy [31]. Hara's empirical formula also shows a quite high accuracy [32]. The IEEE/CIGRE model shows a rather poor accuracy.

The recommended value of a tower surge impedance for each voltage class in Table 2.1 was determined by field measurements in Japan. Although the surge impedance is a representative value, the results of Table 2.3 shows that such a value can not be applied to every tower.

Wave deformation on tower structures (L- or T-shape iron conductor) can be included in a lightning surge analysis, if required, based on the approach in [33].

### 2.3.3.3 Frequency-dependent effect of a tower

The frequency-dependent effect of a tower is readily taken into account in a transient simulation by combining the frequency-dependent tower impedance [31] with Semlyen's or Marti's line model [34], [35] in the EMTP [36].

### 2.3.3.4 Influence of surge impedance and frequency-dependent effect

It should be pointed out that the influence of surge impedance and frequency-dependent effects of tower are heavily dependent on the modelling of the tower footing impedance which will be discussed in the following section. When the footing impedance is represented by a lumped resistance or by a lumped capacitance, then the influence of the tower surge impedance and the frequency-dependent effect of a travelling wave along the tower becomes rather evident. On the contrary, those cause only a minor effect when the footing impedance is represented either by an inductive model or by a nonlinear resistance. Figure 2.6 shows an example of what was mentioned above [8], [37]. The measurement was carried out on a 500 kV tower by applying a current in Figure 2.6(a-1) to the top of the tower. The tower top voltage predicted by a distributed-line model with a constant tower surge impedance and no R-L circuit, Figure 2.6(c-1), differs from that by the frequency-dependent tower model, Figure 2.6(b) which agrees with the measured result, in the case of the footing impedance being a resistance. On the contrary, in the case of an inductive footing model, the tower top voltage obtained by the distributed-line model shows a rather good agreement with the measured result. It should be also noted that some 10% variation of the tower surge impedance does not affect the result in the inductive footing impedance case.

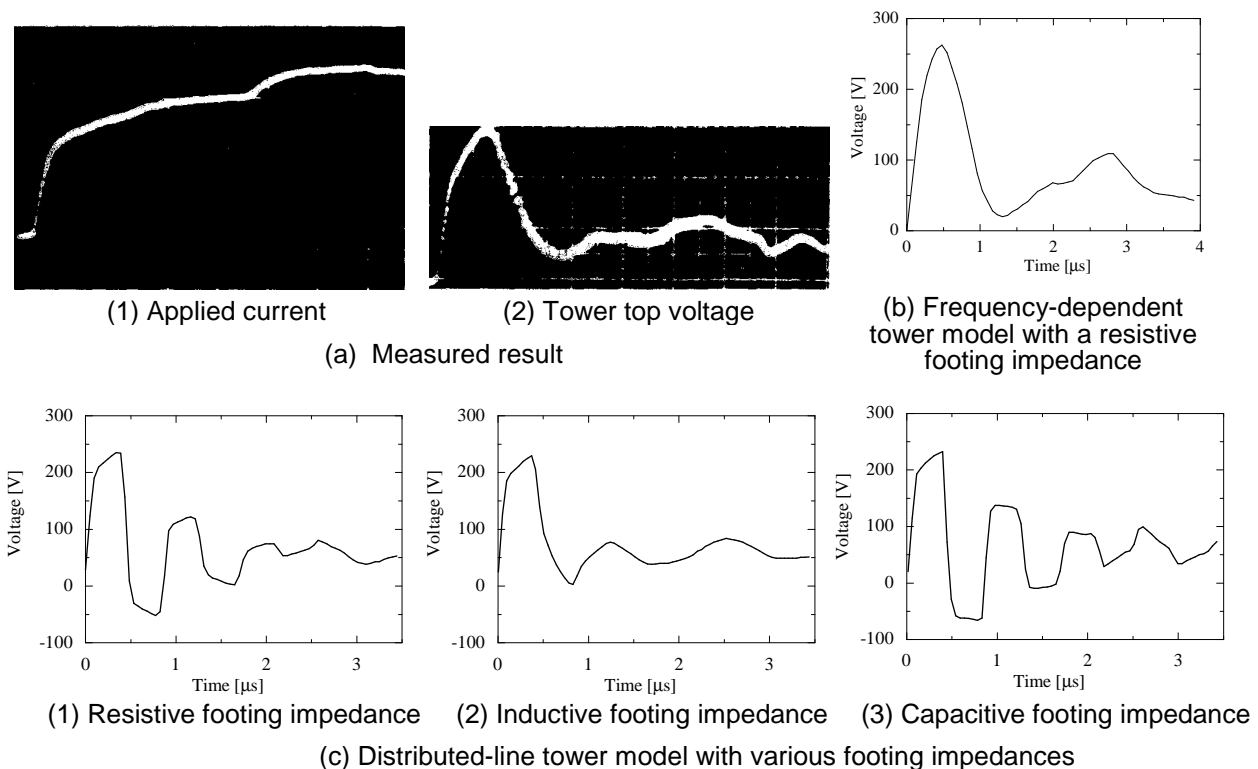


**Figure 2.6: Influence of a tower model on the tower top voltage**

Thus, it is concluded that the frequency-dependent effect of wave propagation along a tower can be neglected and the value of the surge impedance is not significant unless a tower footing impedance is represented by a resistive or a capacitive model.

#### **2.3.3.5 TEM propagation mode**

All the above discussions are based on TEM mode propagation of an electromagnetic wave along a vertical tower. It has been pointed out in many publications that the electromagnetic wave along the tower is not the TEM mode especially at the time of lightning instance to the tower [7], [37]. The same is applied to the lightning channel impedance.

### **2.3.4 Tower footing impedance**

#### **2.3.4.1 Linear footing impedance**

It has been known, in general, that tower footing impedances tend to be capacitive in the case of high resistive soil, and inductive for the case of low resistive soil. A major problem that concerns the correct representation of the tower footing impedance is that such a parameter can be resistive, inductive and capacitive depending on the season and the weather when the relevant measurements are made (i.e. the impedance is temperature- and soil moisture-dependent). For the above reason, a resistive model is usually adopted.

#### **2.3.4.2 Current-dependent nonlinearity**

A number of papers have discussed the current-dependence of a tower footing impedance, and have proposed various models of the nonlinear footing impedance. It has been a common understanding that the current-dependence decreases a lightning surge voltages at the tower and substation. Therefore a simulation neglecting the current dependence gives conservative results. Also in this case a resistive model is usually adopted. There are a number of publications dealing with a non-linear ground impedance and soil ionization which can be used in the EMTP.

#### **2.3.4.3 Non-uniform and frequency-dependent characteristics**

All grounding electrodes, either horizontal (counterpoise) or vertical, presents a non-uniform electromagnetic characteristic [38], which correspond to a so-called critical length of the electrode [17, 39, 67, 156-161]. The characteristic can be taken into account in an EMTP simulation by adopting a model circuit described in [37] together with the frequency-dependent effect. However, this approach requires specific measurements to be performed on the grounding electrode under study.

A general solution for a transient response of a grounding electrode is rather easily obtained by a numerical electromagnetic analysis method such as a finite-difference time-domain (FDTD) method [7], [40], [41] including non-TEM mode propagation.

### **2.3.5 Archon flashover model**

The literature on the subject describes several archon flashover models. To investigate the accuracy, phase-wire voltages at the first tower of Figure 2.1 are calculated by various archon models and are compared [20], [42]. A switch (time-controlled) model and a flashover switch model show not satisfactory agreement especially in the wave-front with the nonlinear inductance model of which the accuracy has been confirmed to be high in comparison with an experimental result [20]. A  $v$ - $t$  characteristic model and a piecewise linear inductance model show a reasonable accuracy except that the maximum voltage of the former is greater and that of the latter is lower than that calculated by the nonlinear inductance model. It might be noteworthy that a current and energy consumed by an arrester in a substation are dependent on an archon model. The switch and the flashover switch models result in much higher energy consumed by an arrester.

An archon flashover might be affected by transient electromagnetic coupling between a lightning path, a tower and phase conductors which are perpendicular to the tower and the lightning channel. Such coupling can not be handled by the EMTP and is easily solved by a numerical electromagnetic analysis [7], [8], [43].



## 2.3.6 Transmission lines, feeders, gas-insulated busses

### 2.3.6.1 Frequency-dependent transmission line impedance

Although a frequency-dependent line model, i.e. Semlyen's or Marti's model [34], [35] is recommended, the maximum error of Marti's model, by making reference to a 1100 kV un-transposed vertical twin-circuit line, is observed to be about 15 % at the wave-front of an impulse voltage in comparison with a field test result (see [44] for further details, surge waveform are shown in Figure 2.7 in comparison with EMTP simulation result). The estimation of possible errors occurred by using these models in lightning overvoltage simulations is not straightforward, because it involves a nonlinearity due to an archorn flashover dependent on a lightning current, an AC source voltage, a flashover phase and so on. It is worth noting that this is an important subject to be investigated in future research studies.

A quite often raised issue concerning the use of the EMTP is that Carson's and Pollaczek's formulas, i.e. the line/cable constants, cannot be used in the high frequency range and thus a revised high frequency formula [45-49] should be, in principle, developed. However it is important to note that, although Carson's and Pollaczek's formulas cannot be used into the high frequency region, at the same time the EMTP can not be used in the same high frequency region in which the transmission line approach becomes questionable. Indeed, the EMTP is based on the circuit theory derived from a TEM mode of wave propagation which is the same as the basic assumption of Carson's, Pollaczek's and Schelkunoff's impedances and the admittance conventionally used in most of the existing circuit analysis computer programs. Therefore, the EMTP cannot be used when the formulas cannot be used, and vice versa. Remind that a high-frequency admittance formula is also required when the high-frequency impedance formula is to be used [50]

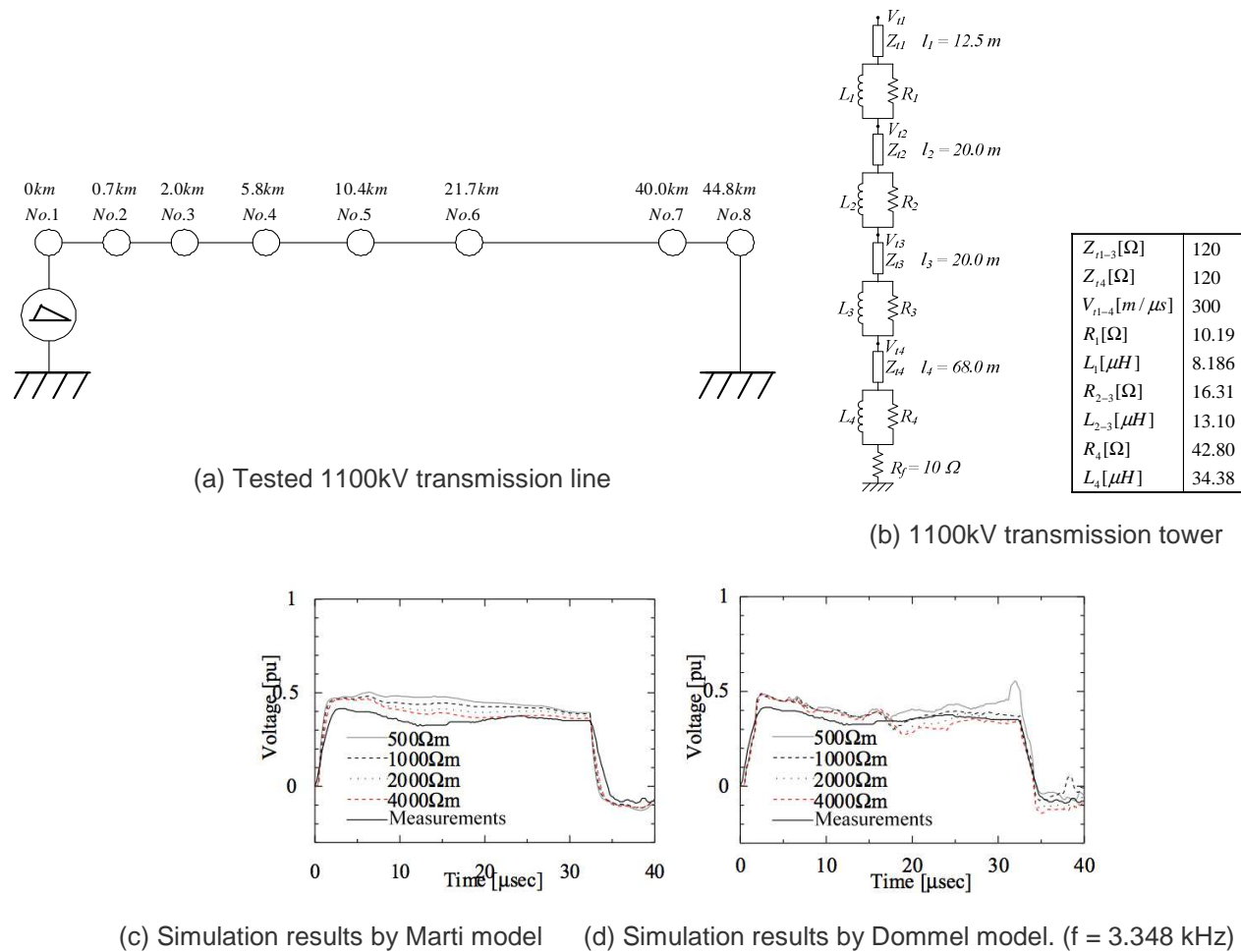


**Figure 2.7: Surge characteristics on an 1100kV line**



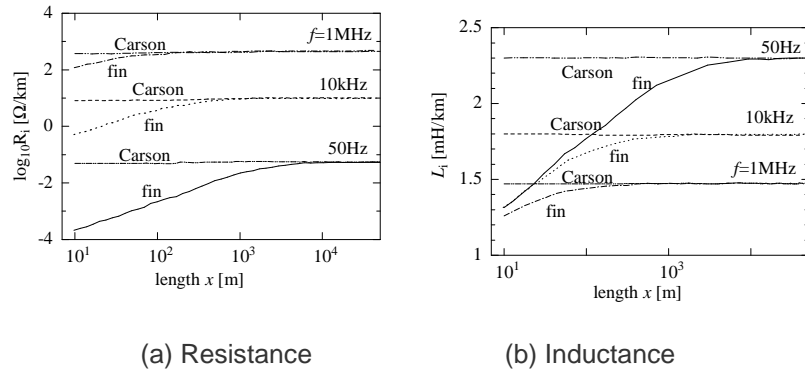


**Figure 2.8: Finite line impedance in comparison with Carson's impedance, (fin = finite line, eq. (2.8))**

### 2.3.6.2 Finite length of a line and a gas-insulated bus

Carson's and Pollaczek's earth return impedances of overhead lines and underground cables were derived based on the assumption of an infinitely long line on the basis of TEM mode propagation [45, 46, 50].

$$\text{length } x \gg \text{height } h \gg \text{radius } r \quad (2.7)$$

It should be noted that most textbook formulas of capacitances and inductances between conductors are based on the above assumptions. It is also worth noting that any capacitance formula give erroneously large value when the radius reaches the conductor's height. Correspondingly, the inductance of an infinite conductor becomes larger than that of a real finite conductor as real lines are not infinitely long. In this respect, it is important to observe that the separation distance between adjacent towers  $x$  of UHV/EHV transmission lines as well as the length of a gas-insulated bus are in the same order of their height  $h$ . If the above condition is not satisfied, Carson's and Pollaczek's impedances are not applicable. Figure 2.8 shows an example of the impedance of a finite length line evaluated by the following equation [50], [51].

$$Z_{finite} = \frac{j\omega\mu_0}{2\pi} \left\{ x \ln \frac{1 + \sqrt{1 + (d_{ij}/x)^2}}{1 + \sqrt{1 + (S_{ij}/x)^2}} + x \ln \frac{S_{ij}}{d_{ij}} - \sqrt{x^2 + d_{ij}^2} + \sqrt{x^2 + S_{ij}^2} + d_{ij} - S_{ij} \right\} [\Omega] \quad (2.8)$$

$$\text{where } d_{ij} = \sqrt{(h_i - h_j)^2 + y^2}, \quad S_{ij} = \sqrt{(h_i + h_j + 2h_e)^2 + y^2}$$

$y$ : horizontal separation between conductors  $i$  and  $j$

$h_i, h_j$ : height of conductors  $i$  and  $j$

$h_e = \sqrt{\rho_e / j\omega\mu_0}$ : complex penetration depth [52]

The results of Figure 2.8 shows that Carson's impedance calculated for the infinitely long line is far greater than that of a real finite-length line when  $x/h$  is not greater enough than 1. The reason for this is readily understood from the following equation [50].

$$Z_{Car} = \int_0^{\infty} \int_0^{\infty} A(x_i, x_j) dx_i dx_j = \int_0^{\infty} B(x_i) dx_i \quad (2.9)$$

$$Z_{fin} = \int_0^{X1} \int_0^{X2} A(x_i, x_j) dx_i dx_j = \int_0^{X1} B'(x_i) dx_i \quad (2.10)$$

As is clear from the above equations,  $Z_{Car}$  involves mutual coupling from the infinitely long conductor “j”, while  $Z_{fin}$  involves mutual coupling from the conductor “j” with the finite length  $X_2$ . In fact,  $Z_{Car}$  becomes infinite due to the line infinite length, and thus “per unit length” impedance is necessarily defined. It should be noted that the per unit length impedance  $\Delta Z_{Car}$  of eq. (2.9) has included the mutual coupling from the infinitely long conductor “j”. On the contrary,  $\Delta Z_{fin}$ , if we define the per unit length impedance in eq. (2.10), includes the mutual coupling only for the finite length  $X_2$ . Thus,

$$\Delta Z_{Carson} > \Delta Z_{finite} \quad (2.11)$$

On the contrary, the per unit length admittance of an infinitely long line is smaller than that of a finite length line.

From the above discussion, it should now be clear that, in principle, Carson’s and Pollaczek’s earth return impedances may not be applied to a lightning surge analysis, because the separation distance  $x$  between adjacent towers is of the same order as the line height. The same observations can be made for a gas-insulated bus as because its length, height and radius are of the same order. This requires further important work with large impact on surge analysis.

It is worth noting that the propagation constants of a finite line is nearly the same as that of an infinitely long line, but the characteristic (surge) impedance is smaller, because of a smaller series impedance and a greater shunt admittance of the finite line. Furthermore the ratio of the surge impedances of two finite lines is nearly the same as that of two infinitely long lines. Finally, travelling wave reflection, refraction and deformation on the finite line is not much different from those on the infinitely long line.

Furthermore, the formulas neglect displacement currents. That is:

$$1/\rho_e = \sigma_e \gg \omega \epsilon_e \text{ or } f \ll 1/2\pi \epsilon_e \rho_e \quad (2.12)$$

where  $\rho_e$  : earth resistivity,  $\epsilon_e$  : permittivity,  $\omega = 2\pi f$

For example, the applicable range of a frequency in the case of  $\rho_e = 1000 \Omega m$  and  $\epsilon_e = \epsilon_0$  is given by:

$$f \ll 18 \text{ MHz or } t \gg 50 \text{ ns}$$

Even in the case of  $\rho_e = 100 \Omega m$ , a transient of 10ns time region can not be simulated by Pollaczek’s and Carson’s impedances.

Under the condition of eqs. (2.7) and (2.12) being not satisfied, only Wedepohl’s impedance formula is applicable [53]. This requires far advanced numerical integration than that applied to Pollaczek’s one.

### 2.3.6.3 Gantry tower feeding a substation – Inclined conductor

A feeding line from the first tower to the substation via the gantry in Figure 2.1 is tilted, i.e. the height is gradually decreased. As a result, its surge impedance is also decreased gradually and thus no significant reflection of traveling waves occurs along the feeding line until the substation entrance. Due to the fact that the surge impedance of a gas-insulated bus (about 70  $\Omega$ ) or a bushing is much smaller than that of an overhead line (300 to 500  $\Omega$ ), noticeable reflection appears at the substation entrance if the inclined configuration of the overhead feeding line is not considered. Indeed, it is better to consider the inclined configuration of a feeding line in case accurate simulations are required. Usually, a maximum difference of 7% in a substation entrance voltage is observed when the inclined configuration is considered [50], [54].

#### 2.3.6.4 Stratified soil

As known, the soil is typically stratified and its resistivity varies significantly between the various layers and, in particular for the top layer, depends on the weather and climate conditions. The earth-return impedance of an overhead conductor above the stratified soils was derived in [55], and the stratified earth effect was investigated in [56]. The stratified soil effect may be far more significant than accurate evaluation of the homogenous earth-return impedance of Pollaczek and Carson, and this requires a further investigation. Also, the frequency-dependency behaviour of the earth resistivity and permittivity as a function of soil humidity have been shown to be significant (e.g. [57]) and, in this respect, cannot be handled by the Pollaczek's approach.

#### 2.3.6.5 Earth-return admittance

On the contrary to the impedance, the shunt admittance of a line has not been focused in general. It should be noted that the impedance and the admittance are one pair to express the behaviour of a voltage and a current along the line, and thus the accuracy of a simulation is dependent on both the impedance and admittance. The earth-return impedance by Pollaczek and Carson corresponds to the first approximation of the shunt admittance, i.e. the admittance for a perfectly conducting earth. If a higher accuracy of a transient analysis is required, the shunt admittance for an imperfectly conducting earth should be taken into account [58], [59]. In general, for overhead lines the ground admittance plays a more or less important role as a function of the considered frequency and ground conductivity [60],[61]. For buried cables such a parameter plays a more significant role and, in general, cannot be neglected [62].

#### 2.3.6.6 Complex permittivity

Inclusion of complex permittivity into the EMTP Cable Constant Program is quite simple in theory (replace the present real permittivity  $\epsilon_r$  by complex permittivity  $\epsilon = \epsilon_r - j\epsilon_i$ ).

To a user, however, it should be noticed that both  $\epsilon_r$  and  $\epsilon_i$  are frequency- and temperature-dependent. When the frequency is less than some MHz (which is likely to happen in an EMTP calculation for both steady state and transient phenomena), then the real part  $\epsilon_r$  can be assumed to be constant (i.e. frequency- and temperature-independent). The imaginary part  $\epsilon_i$ , however, corresponds to the so-called "tan  $\delta$ " or leakage conductance, and hence is quite frequency-dependent and significantly temperature-dependent, even in the low frequency range. The following table illustrates a typical example.

material	water						paper					
T° (C)	1.5	1.5	25	25	85	85	25	25	25	82	82	82
f (Hz)	$1 \times 10^5$	$1 \times 10^8$	$1 \times 10^5$	$1 \times 10^8$	$1 \times 10^5$	$1 \times 10^8$	100	$1 \times 10^5$	$1 \times 10^8$	100	$1 \times 10^5$	$1 \times 10^8$
$\epsilon_r$	87	87	78.2	78	58	58	3.3	3.1	2.77	3.57	3.4	3.08
tan $\delta$	1900	70	4000	50	12400	30	58	200	660	170	85	680

**Table no. 2.4: Frequency- and time- dependent permittivity**

In general, the frequency- and temperature-dependence of the "tan  $\delta$ " are far more significant than those of the real part  $\epsilon_r$ . It is quite hard to obtain the data of the complex permittivity as a function of frequency and temperature. In most cases, these data are not available from a cable manufacturer.

Thus the complex permittivity capability is not included at the present stage.

By the way, the complex permittivity is handled by "Distributed Admittance" option of the CP provided that a user supplies the conductance G and the capacitance C of the cable under study.

#### 2.3.7 Corona wave deformation

The reason for corona wave deformation being not generally considered in lightning surge simulations is that simulations that neglect this phenomena are expected to provide overvoltages higher than that considering corona and, therefore, a conservative result concerning the insulation coordination. The possible errors incurred by ignoring corona are observed to be less than 10 % when lightning strikes the first tower of Figure 2.1 [14]. Although

sophisticated corona models have been proposed [63], [64], the reliability and stability in a lightning overvoltage simulation is not confirmed yet.

It is noteworthy that the corona wave deformation can result in a higher overvoltage at a substation entrance under a specific condition. Figure 2.9 shows a field test result of a normalized voltage ratio  $K$  for the negative polarity case defined in the following equation on a 6.6kV line [65], [66].

$$K = V_n / V_0 \text{ [pu]} \quad (2.13)$$

where  $V_n = V_m / E_0$  : normalized by applied voltage  $E_0$

$V_m$  : maximum phase-wire (PW) voltage at the receiving end (substation entrance)

$V_0$  : normalized voltage with no corona discharge

The experiment was carried out on a 6.6 kV line with one phase wire and one ground wire which were terminated by resistances  $R_p$  and  $R_g$  at the remote end. An impulse voltage up to 800 kV was applied to the sending end of the ground wire. The back flashover in Figure 2.9 was represented by short-circuit of the ground and phase wires. For corona wave deformation decreases a travelling wave voltage on a line, it is a common understanding that the line voltage is decreased by the corona wave deformation and thus the ratio  $K$  is less than 1. In the case of no corona discharge,  $K$  is nearly equal to 1 on a short distance line. It was observed that a measured result of  $K$  on a single-phase line was less than 1.

Figure 2.9 (a) shows that  $K$  in the case of no back-flashover becomes greater than 1 as the applied voltage is increased, i.e. corona discharge occurs. On the contrary in Figure 2.9 (b),  $K$  is less than 1. The reason for the phenomena is readily explained as a result of different attenuation on a phase wire and a ground wire due to corona discharge, and negative reflection of a heavily attenuated traveling wave on the ground wire. The phenomena are less noticeable in positive polarity cases. The detail has been explained in References [65] and [66]. The phenomena have been also realized qualitatively by an EMTP simulation. The increase of a phase-wire voltage at a substation entrance is expected to be more pronounced on an EHV/UHV transmission line on which a corona discharge hardly occurs on a phase wire because of a multiple bundled conductor, while a heavy corona discharge is expected on a ground wire.

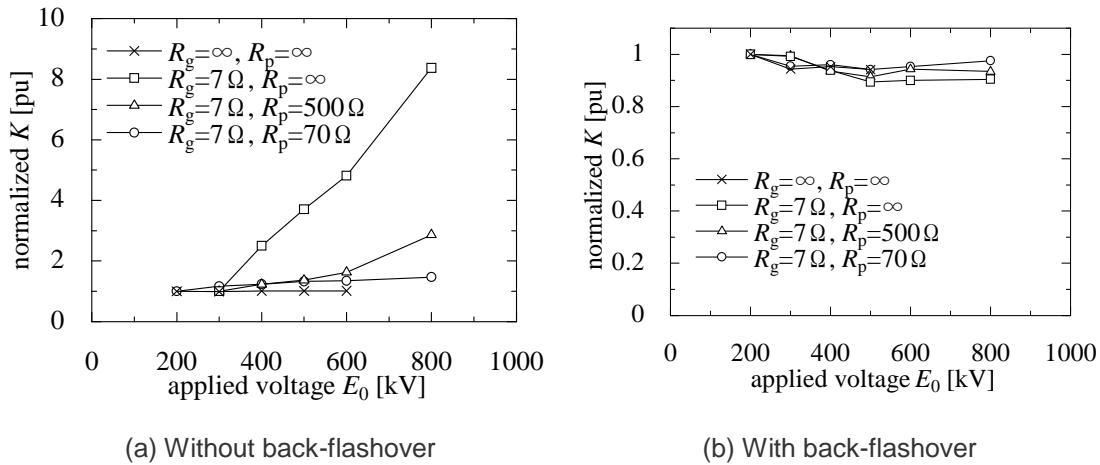


**Figure 2.9: Measured result of normalized voltage ratio  $K$  – Effect of corona wave deformation**

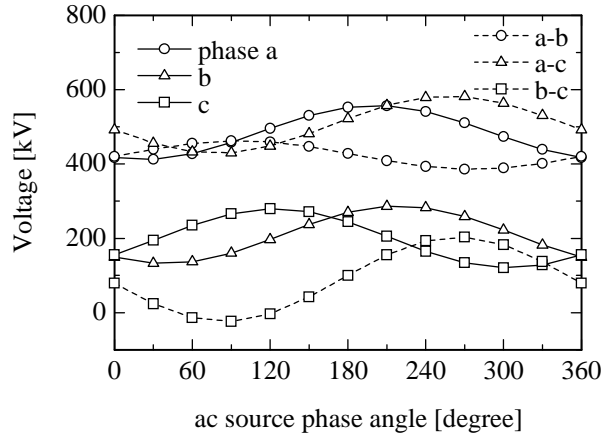


Figure 2.10: Phase-to-phase lightning surge on a 77kV line

### 2.3.8 Phase-to-phase lightning surge

Most of the previous studies on lightning overvoltages refers to ground-referenced voltage. Phase-to-phase overvoltages, however, can damage insulation between phases such as core-to-core insulation in a gas-insulated bus in which three-phase cores are enclosed in the pipe. Figure 2.10 shows an EMTP simulation result of an inter-phase lightning overvoltage at a substation entrance on a 77kV vertical twin-circuit line, when phases a and b' flashovers. The simulation was carried out on a system composed of a 10 km 245/77kV quadruple circuit line and a 10 km 77 kV line. The 77 kV line was connected to a substation through a three-phase underground XLPE cable with the length of 500 m. Because of a lower attenuation of aerial propagation modes, the phase-to-phase overvoltage becomes greater than the phase-to-earth overvoltage especially in the case of a lightning strike to a tower far from a substation.

In this respect, phase-to-phase lightning overvoltages need further investigation.

## 2.4 Comparison of simulation results obtained by means of EMTP-type and NEA methods

EMTP theory and simulation aspects have been explained in the previous sections; the same aspects of numerical electromagnetic analysis are explained in detail in Chapter 3.

### 2.4.1 Transient responses of a grounding electrode

Figure 2.11 illustrates a model circuit of a grounding electrode for an EMTP simulation whose parameters are given below [24].

$$\begin{aligned} C_1 &= C_s - C_0, \quad G_1 = G_s, \quad C_2 = nC_1 \\ C_s &= \pi \epsilon_e x / A, \quad G_s = \pi x / \rho_e A, \quad A = \ell n(2x / e \sqrt{2d \cdot r_2}) \\ C_0 &= 2\pi \epsilon_0 / \ell n(r_2 / r_1) \end{aligned} \quad (2.14)$$

where  $r_1$ : radius of a bare conductor

$d$ : buried depth of the conductor

$r_2$ :  $r_1 + \Delta$ : radius of an artificial outer insulator

$\epsilon_e$ : earth permittivity,  $\epsilon_0$ : free space permittivity

$\rho_e$ : earth resistivity,  $e=2.718\dots$ ,  $n \approx 5$

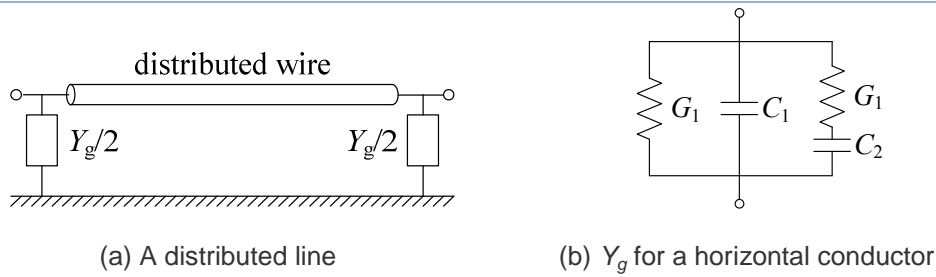


**Figure 2.11 Grounding electrode model**

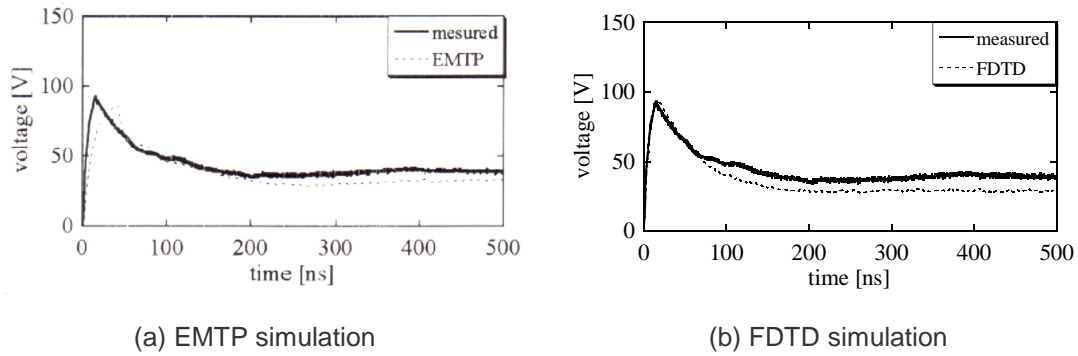


**Figure 2.12 Comparison of measured and simulation results,  $r_1=1\text{ mm}$ ,  $d=0.2\text{ m}$ ,  $x=8\text{ m}$**

$C_s$  and  $G_s$  in the above equation is well-known Sunde's formula [67] of a steady-state capacitance and conductance of a horizontal grounding electrode.

Figure 2.12 shows a comparison of EMTP and FDTD simulation results with a measured result [68]. The simulation results in Figure 2.12 show a reasonable agreement with the measured result.

It should be noted that the EMTP simulation result is quite dependent on the parameters adopted in the simulation which is a function of geometrical and physical constants of a conductor as is clear in eq. (2.14). On the contrary, an FDTD simulation depends very much on the analytical space, absorbing boundary, cell size and time step. The above observation has indicated that the EMTP has been numerically completed quite well, while the FDTD requires a further improvement of its numerical stability.

#### 2.4.2 Transient responses of a vertical earthed structure

Figure 2.13 illustrates an experimental circuit of a gas tower system, which is an 1/30th scale model of a real system, and some measured results [69]. The circuit is the same as that of a wind turbine tower (in case of no pipeline connected to the gas tower) and also the same as that of a transmission tower if the tower is represented by a cylindrical conductor [31] and ground and phase wires are added.

The tower in Figure 2.13 is represented as a distributed-parameter line with a surge impedance  $Z_0$  and a propagation velocity  $c$  of which the values are evaluated by the impedance and the admittance formulas derived in [31]. Figure 2.14 shows a simulation result by the EMTP and Figure 2.15 shows a simulation result by the FDTD.

It is observed that the simulation results in Figure 2.14 by the EMTP and in Figure 2.15 by the FDTD agree reasonably well with the measured result in Figure 2.14. A difference observed between the measured and the EMTP simulation results is estimated due to mutual coupling between the tower, the pipeline and measuring wires. Also, the frequency-dependent effect of the conductor affects the difference.

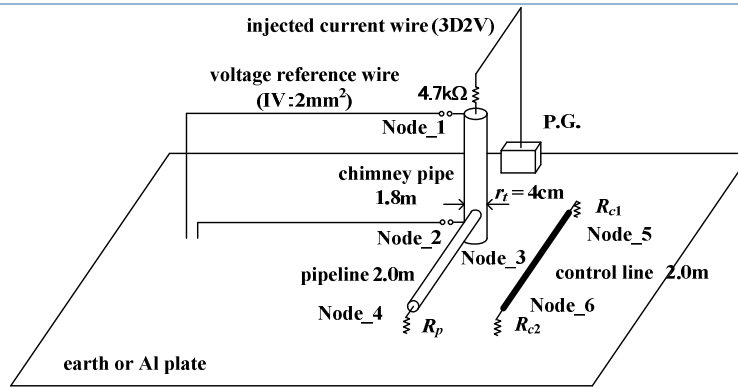


Figure 2.13: Experimental setup:  $R_p=150\Omega$

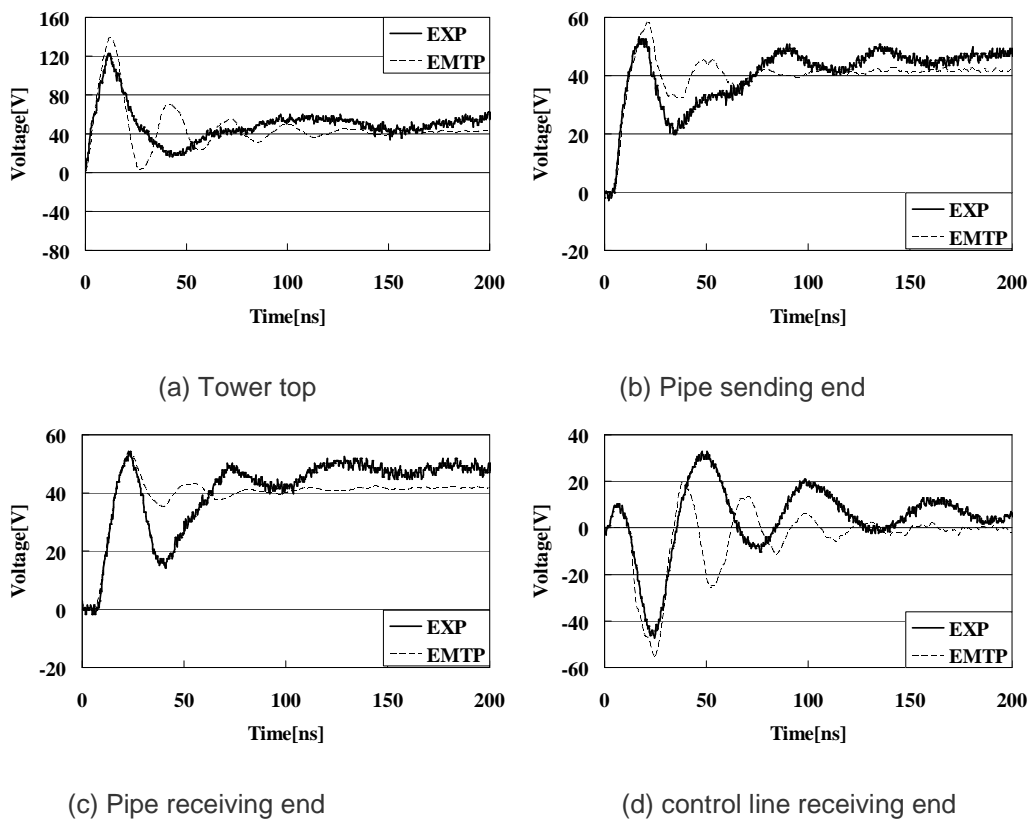
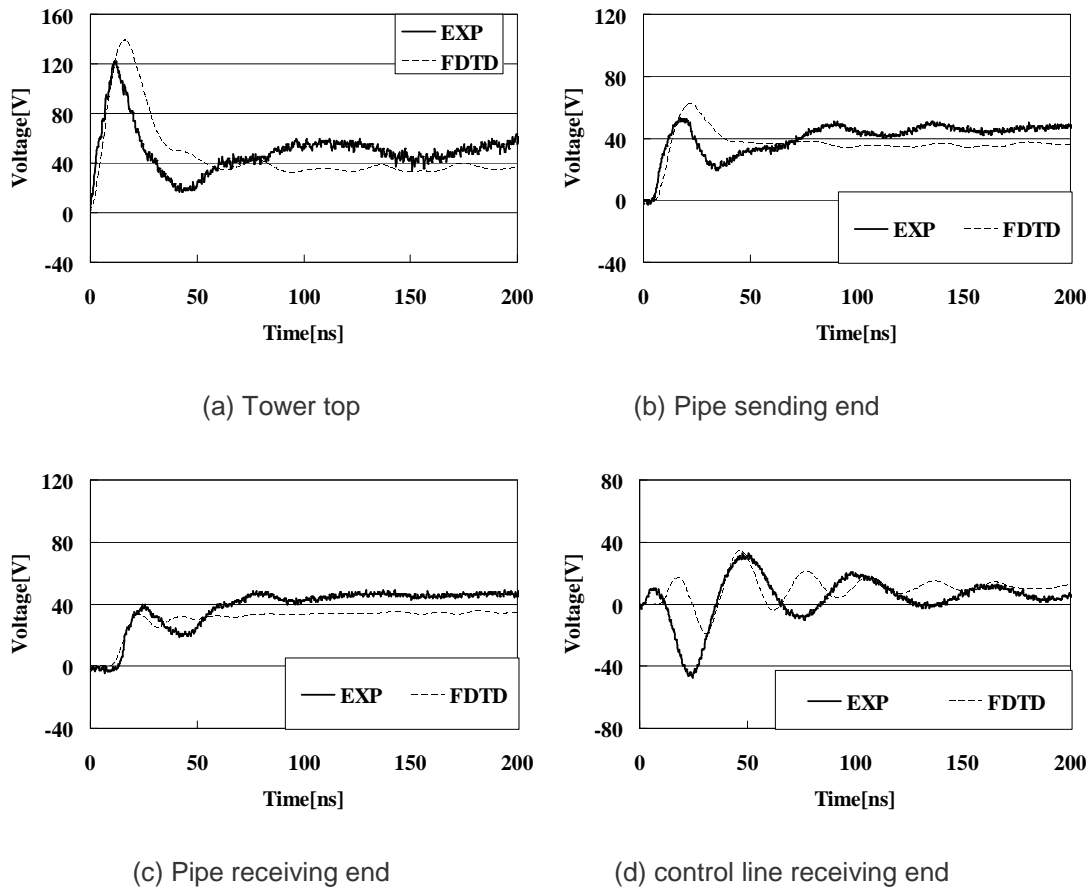


Figure 2.14: Measured and EMTP simulation results



**Figure 2.15 FDTD simulation results**

### 2.4.3 Archorn voltage during a back-flashover

The electromagnetic field around a transmission tower hit by lightning changes dynamically while electromagnetic waves make several round-trips between a shield wire and the ground. During this interval, the waveforms of archorn voltages vary complexly. For a tall structure, such as an EHV tower, the contribution of the tower surge characteristic to the archorn voltages becomes dominant because the travel time of a surge along the tower is comparable to the rise time of a lightning current. In particular, for the case of back-flashover studies on high towers, a powerful electromagnetic impulse is produced since the archorn voltage of several MV is chopped steeply. The electromagnetic impulse expands spherically and couples with the other phase lines. Such electromagnetic coupling is different from the TEM coupling and it may influence significantly the archorn voltages of other phases. This issue, however, has been paid little attention in analysing a multiphase back-flashover.

To analyze such a very-fast transient electromagnetic field around a three-dimensional conductor system, numerical electromagnetic codes are certainly appropriate. Among many available codes, results obtained by means of the Thin-Wire Time-Domain Analysis (TWTDA) code [70], [71] based on the method of moments [72] are here given. This specific code allows incorporating nonlinear effects into the analysis [8].

In this section, archorn voltages of a simulated 500 kV twin-circuit tower in Figure 2.16 (a) hit by lightning, in the case of one-phase back-flashover, are analyzed by a modified TWTDA code that includes a recently proposed flashover model [73], [74]. A similar analysis is also carried out by EMTP [1], and the results are compared with those computed by the modified TWTDA code.



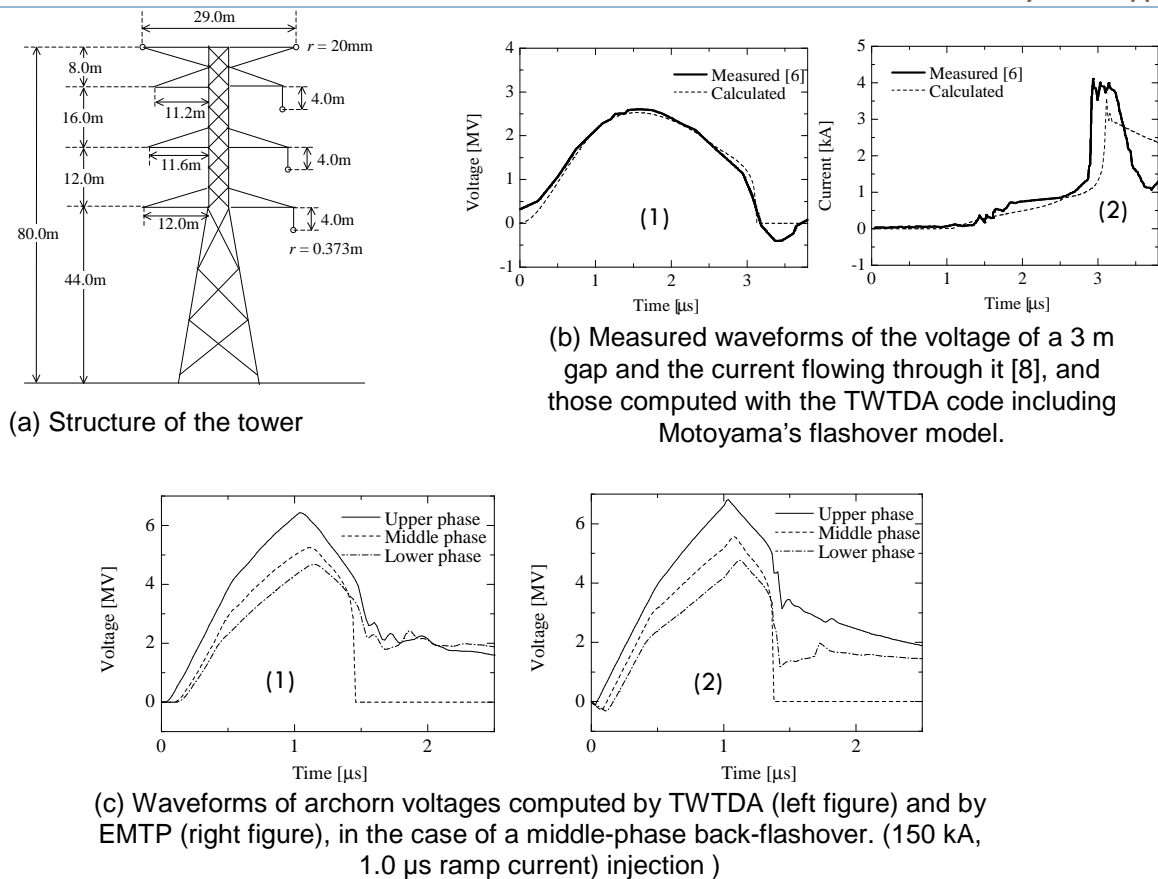


**Fig. 2.16 Archorn voltages during a back-flashover.**

Figure 2.16 (b) shows measured waveforms of the voltage of a 3 m gap representing an archorn and the current flowing through it [68], and those computed by the TWTDA code. Figure 2.16 (c) shows the archorn voltages computed by TWTDA (Figure 2.16 (c) left) and EMTP (Figure 2.16 (c) right). In the EMTP simulation, the multistory tower model [18] is used, and the leader progression flashover model [73] is represented by a general-purpose description language 'MODELS' [75] in EMTP. The archorn voltages computed by EMTP agree well with those computed by TWTDA before the back-flashover on one phase. On the other hand, after the back-flashover, the archorn voltages of the other two phases computed by EMTP decay more steeply than those computed by TWTDA, and they deviate from the results computed by TWTDA during about 1  $\mu$ s after that. The deviation is noticeable particularly in the case of the middle- or the lower-phase back-flashover although the settling values of both results are in good agreement.

One of the reasons for these discrepancies may be attributed to somewhat high lumped resistors of the multistory tower model, which are employed to reproduce the peak values of archorn voltages for step current injection into the tower top. A very steep wave, injected into the top of this tower model, propagates downward without reflection at nodes, but an upward propagating wave, which may be a reflected wave at the ground or the associated with the middle- or lower-phase back-flashover, attenuates much at these nodes. The difference of induction or coupling between the actual dynamic electromagnetic field around a tower struck by lightning and the TEM mode, which is a basis of an EMTP multi-conductor model, must be another reason.

## 2.5 Concluding Remarks

Schelkunoff's, Pollaczek's and Carson's impedances adopted in any EMTP-type simulation tools cannot be straightforward applied in case of surges that involve the presence of non-TEM propagation modes. Due to the fact that EMTP-type simulation tools are based on the circuit theory (assuming TEM propagation mode), they cannot give accurate solutions in case of high frequency transients. Also, EMTP-type tools cannot deal with a circuit of

which the parameters are unknown. Although EMTP-like approaches involve various problems and limitations, they have been widely used as powerful tools to analyze power system transients in view of their straightforward implementation and use in relation to the modelling of power systems components.

EMTP-type simulation tools can give quite reasonable results with a satisfactory accuracy in comparison with field test results. In this respect, EMTP-type simulation results have been adopted in designing power equipment and facilities, and also applied to establish a standard in insulation coordination.

On the contrary, numerical electromagnetic analysis methods can deal with transients associated with both TEM and non-TEM propagation modes. Furthermore, they do not require the knowledge of circuit parameters but the definition of geometrical and physical characteristics of a given domain. However, they require a large amount of computer resources, and existing codes are not general enough to deal with various types of transients especially when large systems needs to be studied.

It is note-worthy that input data, either physical or geometrical parameters, should be carefully examined in both of the above-mentioned simulation tools. In this respect, input data must be consistent with the assumptions and limits of the adopted tool as non-correct assumptions on these parameters can result in erroneous simulations. The uncertainties related to the non-perfect knowledge of simulation parameters, and/or domain characteristics, are typically overcome by the experience of both EMTP-type and NEA developers and users.

Typical examples are: (i) earth resistivity that varies along a transmission line and also along the depth of the earth (the stratified earth effect on a transient may be far from typical assumptions at the basis of Pollaczek's and Carson's earth-return impedance that assume a homogenous earth conductivity); (ii) stray capacitances and residual inductances of a power apparatus that are, in general, not available from a manufacturer; (iii) nonlinear characteristic of resistivity and permittivity of cable insulations and the semiconducting layers.

### 3 THEORY OF NUMERICAL ELECTROMAGNETIC ANALYSIS FOR TRANSIENTS

#### 3.1 Introduction about the numerical electromagnetic analysis

##### 3.1.1 Basic equations in electromagnetics

James Clerk Maxwell established the complete formulation of Maxwell's equations in 1873. These four equations of fours field vectors at a space point  $\mathbf{r}$  in the time domain are given in (3.1), where  $\mathbf{E}(\mathbf{r},t)$  is the electric field intensity,  $\mathbf{H}(\mathbf{r},t)$  is the magnetic field intensity,  $\mathbf{D}(\mathbf{r},t)$  is the electric flux density,  $\mathbf{B}(\mathbf{r},t)$  is the magnetic flux density.  $\mathbf{J}(\mathbf{r},t)$  is the electric current densities and  $\rho_v(\mathbf{r},t)$  are the volume electric charge density.

Maxwell's equations

Differential form	Integral form	
$\nabla \times \mathbf{E}(\mathbf{r},t) = -\frac{\partial \mathbf{B}(\mathbf{r},t)}{\partial t}$	$\oint_L \mathbf{E}(\mathbf{r},t) \cdot d\mathbf{l} = -\int_S \frac{\partial \mathbf{B}(\mathbf{r},t)}{\partial t} \cdot d\mathbf{S}$	
$\nabla \times \mathbf{H}(\mathbf{r},t) = \mathbf{J}(\mathbf{r},t) + \frac{\partial \mathbf{D}(\mathbf{r},t)}{\partial t}$	$\oint_L \mathbf{H}(\mathbf{r},t) \cdot d\mathbf{l} = \int_S (\mathbf{J}(\mathbf{r},t) + \frac{\partial \mathbf{D}(\mathbf{r},t)}{\partial t}) \cdot d\mathbf{S}$	(3.1)
$\nabla \cdot \mathbf{D}(\mathbf{r},t) = \rho_v(\mathbf{r},t)$	$\oint_S \mathbf{D}(\mathbf{r},t) \cdot d\mathbf{S} = \int_V \rho_v(\mathbf{r},t) dV$	
$\nabla \cdot \mathbf{B}(\mathbf{r},t) = 0$	$\oint_S \mathbf{B}(\mathbf{r},t) \cdot d\mathbf{S} = 0$	

The differential forms of Maxwell's equations in the frequency domain are derived by application of Fourier transformation of (3.1) and the following equations are obtained.

$$\begin{aligned}\nabla \times \mathbf{E}(\mathbf{r}) &= -j\omega \mathbf{B}(\mathbf{r}), \\ \nabla \times \mathbf{H}(\mathbf{r}) &= \mathbf{J}(\mathbf{r}) + j\omega \mathbf{D}(\mathbf{r}), \\ \nabla \cdot \mathbf{D}(\mathbf{r}) &= \rho_v(\mathbf{r}), \\ \nabla \cdot \mathbf{B}(\mathbf{r}) &= 0,\end{aligned}\tag{3.2}$$

where  $\mathbf{E}(\mathbf{r})$ ,  $\mathbf{H}(\mathbf{r})$ ,  $\mathbf{B}(\mathbf{r})$ ,  $\mathbf{D}(\mathbf{r})$ ,  $\mathbf{M}(\mathbf{r})$ ,  $\mathbf{J}(\mathbf{r})$ , and  $\rho_v(\mathbf{r})$  are complex vectors or scalar phasors, which are the Fourier transforms of the corresponding vector and scalar quantities in the time domain.

The current density  $\mathbf{J}$  and the charge density  $\rho_v$  in the above equations refer to all currents and charges. In some cases, it is found convenient to explicitly separate them into excited source current and induced (by the fields) current. For example, the current density term is  $\mathbf{J}_e + \mathbf{J}_i$ , where  $\mathbf{J}_e$  is an excited source current that exists only in the source region and  $\mathbf{J}_i$  is an induced current that may exist in the region under consideration. Similarly the charge distribution is also separated into source and induced quantities.

The relations of the electric and magnetic flux densities to the electric and magnetic field intensities are expressed by (3.3):

$$\mathbf{D}(\mathbf{r}) = \epsilon_r \epsilon_0 \mathbf{E}(\mathbf{r}), \quad \mathbf{B}(\mathbf{r}) = \mu_r \mu_0 \mathbf{H}(\mathbf{r}),\tag{3.3}$$

where  $\epsilon_r$  and  $\mu_r$  are relative permittivity and permeability, respectively,  $\epsilon_0 = 8.854 \times 10^{-12}$  F/m is the dielectric constant, and  $\mu_0 = 4\pi \times 10^{-7}$  H/m is the magnetic constant.

Maxwell's equations in the infinite homogenous space may be solved by introduction of auxiliary potential functions. The most well-known potential are the Hertz potentials which are electric scalar potential,  $\phi(\mathbf{r})$  and magnetic vector potential,  $\mathbf{A}(\mathbf{r})$ .

The definition of the auxiliary vector potential,  $\mathbf{A}(\mathbf{r})$  called magnetic vector potential is written in the following equation:

$$\mathbf{B}(\mathbf{r}) = \nabla \times \mathbf{A}(\mathbf{r}).\tag{3.4}$$

Applying (3.4) in the first equation of (3.2), the electric field intensity can be calculated as (3.5):

$$\mathbf{E}(\mathbf{r}) = -j\omega \mathbf{A}(\mathbf{r}) - \nabla \phi(\mathbf{r}),\tag{3.5}$$

where  $\phi(\mathbf{r})$  is an auxiliary scalar potential called an electric scalar potential.

For the introduction of the auxiliary potentials a unique solution is required. The form of the equation for potentials is depended on a definition that is called gauge. The most well known is Lorentz gauge which is defined in the following equation.

$$\nabla \cdot \mathbf{A}(\mathbf{r}) = -j\omega \mu \epsilon \phi(\mathbf{r}).\tag{3.6}$$

This gauge leads to decouple the auxiliary potentials and the wave equations for the both potentials are given.

$$\begin{aligned}\nabla^2 \mathbf{A}(\mathbf{r}) + \omega^2 \mu \epsilon \mathbf{A}(\mathbf{r}) &= -\mu \mathbf{J}(\mathbf{r}) \\ \nabla^2 \phi(\mathbf{r}) + \omega^2 \mu \epsilon \phi(\mathbf{r}) &= -\frac{\rho_v}{\epsilon}.\end{aligned}\tag{3.7}$$

The analytical technique for solving the wave equations was established by George Green in 1828. The technique was introduced by the Green function method that has limitation on only linear boundary-value problem since it is based on the superposition principle.

Consider the wave equations which is excited by a source in the form of Dirac delta function  $\delta(\mathbf{r}, \mathbf{r}')$ . The equation can be written in the following equation.

$$\nabla^2 g(\mathbf{r}, \mathbf{r}') + k^2 g(\mathbf{r}, \mathbf{r}') = -\delta(\mathbf{r}, \mathbf{r}'). \quad (3.8)$$

Note that  $\mathbf{r}'$  is the location of the source, and  $k = \omega\sqrt{\mu\epsilon}$ . Assuming the source located at the origin and (3.8) is rewritten the spherical coordinate as:

$$\frac{1}{r^2} \frac{\partial}{\partial r} \left( r^2 \frac{\partial}{\partial r} g(r) \right) + k^2 g(r) = -\delta(r). \quad (3.9)$$

The solution of (3.9) may be expressed by:

$$g(r) = A \frac{e^{-jkr}}{r}, \quad (3.10)$$

where A is constant, and no initial conditions are considered.

Substituting (3.10) in (3.9), the constant A can be calculated as  $\frac{1}{4\pi}$ . Thus, the solution of (3.9) is obtained in the following equation.

$$g(r) = \frac{1}{4\pi} \frac{e^{-jkr}}{r}. \quad (3.11)$$

Using (3.11), the solution at a space point  $\mathbf{r}$  for an arbitrary source point  $\mathbf{r}'$  is

$$g(\mathbf{r}, \mathbf{r}') = \frac{1}{4\pi} \frac{e^{-jk|\mathbf{r}-\mathbf{r}'|}}{|\mathbf{r}-\mathbf{r}'|}. \quad (3.12)$$

Base on the superposition principle, the potentials generated arbitrary sources can be written as:

$$\begin{aligned} \phi(\mathbf{r}) &= \int_V \frac{\rho_v(\mathbf{r}')}{\epsilon} g(\mathbf{r}, \mathbf{r}') dV, \\ A(\mathbf{r}) &= \int_V \mu \mathbf{J}(\mathbf{r}') g(\mathbf{r}, \mathbf{r}') dV. \end{aligned} \quad (3.13)$$

The auxiliary potentials in time domain can be derived by taking inverse Fourier transform of (3.13). The following equation is obtained:

$$\begin{aligned} \phi(\mathbf{r}, t) &= \frac{1}{4\pi\epsilon} \int_V \frac{\rho_v(\mathbf{r}', t')}{R} dV \\ A(\mathbf{r}, t) &= \frac{\mu}{4\pi} \int_V \frac{1}{R} \cdot \frac{\partial(\mathbf{J}(\mathbf{r}', t'))}{\partial t'} dV, \end{aligned} \quad (3.14)$$

where  $R = |\mathbf{r} - \mathbf{r}'|$ ,  $v$  is a speed of electromagnetic field in a media and  $t' = t - R/v$ .

The potentials lead to the formulation of the electric field integral equation (EFIE) and also the mixed-potential integral equation (MPIE) which will be explained in Reference [102] when those are applied to an appropriate boundary condition.

The EFIE employed in the method of moment is derived by starting on consideration of the total electric field strength  $\mathbf{E}$  at a point  $\mathbf{r}$ :

$$\mathbf{E} = \mathbf{E}^i + \mathbf{E}^s, \quad (3.15)$$

where  $\mathbf{E}^i$  is an incident electric field and  $\mathbf{E}^s$  is a scattering electric field reacted to  $\mathbf{E}^i$ .

The total electric field is corresponding to Ohm's law as the following form:

$$\mathbf{E} = \mathbf{J} / \sigma, \quad (3.16)$$

where  $\sigma$  is conductivity of considered media.

Substituting (3.15) and (3.16) into (3.5), the incident electric field can be written in the following form.

$$\mathbf{E}^i(\mathbf{r}) = \mathbf{J}(\mathbf{r}) / \sigma + j\omega\mu \int_{V'} g(\mathbf{r}, \mathbf{r}') \mathbf{J}(\mathbf{r}') dV + \frac{\nabla}{\epsilon} \int_{V'} g(\mathbf{r}, \mathbf{r}') \rho_v(\mathbf{r}') dV \quad (3.17)$$

The charge density is related to the current density via the charge conservation equation which is written by:

$$\nabla \cdot \mathbf{J} = -j\omega\rho_v. \quad (3.18)$$

Substituting (3.18) into (3.17), the result yields the incident electric field in the following form.

$$\mathbf{E}^i(\mathbf{r}) = \mathbf{J}(\mathbf{r}) / \sigma + j\omega\mu \int_{V'} g(\mathbf{r}, \mathbf{r}') \mathbf{J}(\mathbf{r}') dV - \frac{\nabla}{j\omega\epsilon} \int_{V'} g(\mathbf{r}, \mathbf{r}') \nabla \cdot \mathbf{J}(\mathbf{r}') dV \quad (3.19)$$

Based on the perfectly conducting material, the current and charge are distributed on only the surface. The tangential component of the electric field intensity on the conductor surface is calculated by:

$$-\mathbf{n} \times \mathbf{n} \times \mathbf{E}^i(\mathbf{r}) = -\mathbf{n} \times \mathbf{n} \times \left\{ j\omega\mu \int_S g(\mathbf{r}, \mathbf{r}') \mathbf{J}_s(\mathbf{r}') dS - \frac{\nabla}{j\omega\epsilon} \int_S g(\mathbf{r}, \mathbf{r}') \nabla \cdot \mathbf{J}_s(\mathbf{r}') dS \right\}, \quad (3.20)$$

where  $\mathbf{n}$  is a unit normal vector on the surface, and  $\mathbf{J}_s$  is a surface current density.

The derivation of the EFIE in the time domain starts from (3.5) which can be written in the time domain as the following equation.

$$\mathbf{E}(\mathbf{r}, t) = -\frac{\partial \mathbf{A}(\mathbf{r}, t)}{\partial t} - \nabla \phi(\mathbf{r}, t) \quad (3.21)$$

In a similar manner, the EFIE in the time domain derived from (3.14), (3.15) and (3.21) is obtained as the following:

$$\mathbf{E}^i(\mathbf{r}, t) = \mathbf{J}(\mathbf{r}', t) / \sigma + \frac{\mu}{4\pi} \int_{V'} \frac{1}{R} \cdot \frac{\partial \mathbf{J}(\mathbf{r}', t')}{\partial t'} dV - \frac{\nabla}{4\pi\epsilon} \int_{V'} \frac{\rho_v(\mathbf{r}', t')}{R} dV. \quad (3.22)$$

The charge in (3.22) can be calculated by the continuity equation as the following.

$$\rho_v(\mathbf{r}', t') = -\int_{-\infty}^{t'} \nabla \cdot \mathbf{J}(\mathbf{r}', \tau) d\tau \quad (3.23)$$

Based on the perfectly conducting material, the current and charge are distributed on only the surface. The tangential component of the electric field intensity in the time domain on the conductor surface is calculated by:

$$-\mathbf{n} \times \mathbf{n} \times \mathbf{E}^i(\mathbf{r}, t) = -\mathbf{n} \times \mathbf{n} \times \left\{ \frac{\mu}{4\pi} \int_S \frac{1}{R} \cdot \frac{\partial \mathbf{J}_S(\mathbf{r}', t')}{\partial t'} dS - \frac{\nabla}{4\pi\epsilon} \int_S \frac{\rho_S(\mathbf{r}', t')}{R} dS \right\}, \quad (3.24)$$

where  $\rho_s$  is a surface charge density which can be calculated as the following equation.

$$\rho_S(\mathbf{r}', t') = -\int_{-\infty}^{t'} \nabla \cdot \mathbf{J}_S(\mathbf{r}', \tau) d\tau \quad (3.25)$$

### 3.1.2 Classification of electromagnetic calculation techniques

Computational electromagnetics are getting increasingly attention not only in the research fields but also in the industrial fields. An electromagnetic modeling involves solving Maxwell's equations directly and/or indirectly in general. In the indirect approach, a circuit theory is employed by taking into account electromagnetic coupling by mutual inductance and capacitance among circuit elements. A method solving Maxwell's equation directly can be classified into a differential equation based method and an integral equation based method. Equations (3.1) and (3.2) are employed in the differential equation (DE) based method and an equation (3.19) or (3.22) is employed in the integral equation (IE) based method. A brief discussion on those approaches is presented in this section.

A circuit theory based method involving an equivalent circuit lumped model and/or a distributed circuit model has been a tradition of modelling electrical components. It involves partitioning the component to be analysed into several lumped and/or distributed elements. The equivalent circuit parameters like the resistance, inductance, and capacitance are calculated for each lumped and/or distributed element. The calculation of these lumped parameters is either done using analytical or numerical routines. The electromagnetic couplings between the lumped sections are considered through mutual inductances and capacitances. The lumped and/or distributed parameters are later assembled using Kirchhoff's voltage law and current law to represent the complete model.

The DE based method involves solving Maxwell's equations directly. One solves for the fields in whole space of interests. Firstly, a numerical grid or mesh of the problem space is constructed, and the fields propagate between any two points through the grid. Due to memory limitations it is impossible to mesh the entire space. Usually only a finite problem domain is meshed, and an appropriate boundary condition like the absorbing boundary condition (ABC) such as the perfect matching layer (PML), Mur's absorbing boundary and Liao's absorbing boundary is applied to simulate fields propagating to infinity. The solution involves solving large sparse matrices with large number of unknowns. Since the field propagates from a grid point to another grid point, small errors occurring at the grid points accumulate leading to large grid dispersion errors for larger simulations. This problem is usually minimized by using a finer grid, but this means a larger number of unknowns and hence large problem size (analytical space). Examples of DE techniques which are presented in this chapter include finite-difference time-domain (FDTD) method and finite element method (FEM).

The IE based method involves the integral forms of Maxwell's equation. It aims at solving for field sources (currents and potentials) on surfaces or boundaries, thus reducing the dimensionality of the whole problem domain. Like a DE based method it also involves solving matrix equations, but the matrices in this case are dense (fully populated with nonzero entries). An IE method does not require discretization of the whole problem domain, instead only the outer and interface surfaces of the problem's geometry are discretized. Therefore, the IE method will have far fewer (usually the order of magnitude fewer) unknowns than a DE method for the open space problem. Unlike a DE method, the field propagates from points A to B using exact closed form solutions, thus minimizing grid dispersion errors. Spurious resonances may occur with IE methods, some times resulting from the meshing schemes. Usually appropriate measures are taken to suppress them. Examples of IE methods which present in this chapter include the method of moment (MoM) and the partial element equivalent circuit (PEEC) method.

In fact, there are many numerical electromagnetic methods employed for electromagnetic transient calculation. However, only five well-known methods, based on field theory, FDTD, FEM, MoM and PEEC are presented in this chapter. Table 3.1 shows main features of the most common numerical electromagnetic calculation techniques in brief.

Method	Circuit theory based method	FDTD	FEM	MoM	PEEC
<b>Formulation</b>	Circuit theory	Maxwell's equation (DE)	Maxwell's equation (DE)	Maxwell's equation (IE)	Maxwell's equation (IE)
<b>Solution variables</b>	Circuit (I and/or V)	Fields (E and H)	Fields (E and H)	Circuit (I)	Circuit (I and/or V)
<b>Solution Domain</b>	TD or FD	TD or FD	TD or FD	TD or FD	TD or FD
<b>Cell geometry</b>	-	Orthogonal	Non-orthogonal	Non-orthogonal	Non-orthogonal
<b>Advantage</b>	<ul style="list-style-type: none"> <li>- Easy to use (simple equations)</li> <li>- Robust</li> <li>- Time efficiency</li> </ul>	<ul style="list-style-type: none"> <li>- Easy to use (simple equations)</li> <li>- Robust</li> <li>- Complex materials especially including ground effect</li> <li>- Provide full-wave solutions</li> </ul>	<ul style="list-style-type: none"> <li>- Cell flexibility</li> <li>- Complex materials especially including ground effect</li> <li>- Provide full-wave solutions</li> </ul>	<ul style="list-style-type: none"> <li>- Cell flexibility</li> <li>- appropriate for open space problem</li> <li>- Provide full-wave solutions</li> </ul>	<ul style="list-style-type: none"> <li>- Cell flexibility</li> <li>- Post processes for calculating V and I are not required</li> <li>- appropriate for open space problem</li> <li>- Provide full-wave solutions</li> </ul>
<b>Drawbacks</b>	<ul style="list-style-type: none"> <li>- fail in a high frequency range</li> <li>- Not providing full-wave solutions</li> </ul>	<ul style="list-style-type: none"> <li>- Cell nonflexibility</li> <li>- Storage requirements</li> <li>- Domain truncated by an appropriate boundary condition</li> <li>- Post processes for calculating V and I are required</li> </ul>	<ul style="list-style-type: none"> <li>- Solve large linear system</li> <li>- Storage requirements</li> <li>- Domain truncated by an appropriate boundary condition</li> <li>- Post processes for calculating V and I are required</li> </ul>	<ul style="list-style-type: none"> <li>- Green's function knowledge</li> <li>- Computationally heavy</li> <li>- Quite complicated when ground effect is included</li> </ul>	<ul style="list-style-type: none"> <li>- Green's function knowledge</li> <li>- Computationally heavy</li> <li>- Quite complicated when ground effect is included</li> </ul>

Table no.3.1: Main feature of the most common numerical electromagnetic calculation techniques



### 3.2 Circuit-theory based approach and transmission line (TL) models

The circuit theory based method is related to extraction of equivalent circuit lumped and/or distributed circuit elements. The electromagnetic couplings between the lumped or distributed sections are considered through mutual inductances (magnetic field coupling), mutual capacitances (electric field coupling), and mutual resistance (in a lossy media). The method basically involves discretizing the structure into sections that are electromagnetically coupled. Each section is assumed to be electrically small and can be represented by lumped or distributed circuit parameters, inductance, capacitance, and resistance ( $L$ ,  $C$ , and  $R$ ). There are three partitioning schemes, namely the inductive partitions, capacitive partition, and the resistive partitions. Each  $L$ ,  $C$  and  $R$  can be calculated by analytical formulae and/or by numerical techniques. An attempt to model a conducting object such as a tower, a transmission line, and a cable with a lumped element and distributed elements can be found in [76], [77]. The lumped and distributed parameters are assembled using Kirchhoff's voltage law and current law to represent the complete model and can be implemented into a circuit simulator for solution in the time and frequency domains.

A major problem with lumped element equivalent circuit approach is the frequency limitation. The models are limited to cases where the dimensions of the lumped sections are much smaller than the minimum wavelengths of interest. Equivalently, it is difficult for the lumped models to characterize the propagation of very fast pulses which have electromagnetic retardation within each lumped section.

For the approach of distributed parameter circuits (a transmission line model: TL), the conductors have to be very close to the return path or nearby a conducting ground plane (the height of the conductor is much smaller than the minimum wavelength). The assumption of quasi-TEM propagation is effective and that configurations can be modeled by the TL approach. The TL approach, which takes into account external electromagnetic field interaction, can be found in [78]-[80]. There are some actual configurations of problems which are more complicated and out of this assumption. Therefore, to obtain accurate results, the numerical electromagnetic solving full Maxwell's equation directly is more appropriate to analyze those problems

### 3.3 Numerical solution of Maxwell's differential equations

The most commonly used methods based on the differential equation are the finite-difference time-domain (FDTD) method and finite element method (FEM). The popularity of the FDTD method is very large compared to the FEM method. There are several reasons why the FDTD method is so popular. The most important ones are its programming simplicity and the simplicity of its numerical integration algorithm. Because of the simplicity of the method, an engineer can develop a three-dimensional (3-D) FDTD code in a relatively short amount of time. FEM offers some important advantages over the standard FDTD method. The most obvious one has to do with its use of unstructured grids. Since the grid is unstructured, it offers flexibility in modeling complex geometries. The FDTD method is a good choice when modeling geometries of low complexity, while the FEM is most appropriate when complicated geometries need to be modeled. For a complex structure, an application of the FDTD method would require a very dense grid to resolve accurate geometry.

This section describes the basic theory of two representative methods based on the differential equations, i.e. the FDTD method and the FEM in brief detail.

#### 3.3.1 Finite-difference time-domain method (FDTD)

The finite-difference time-domain (FDTD) method is one of the most commonly used techniques in electromagnetics, dating back in the 1960s, with the introduction of unstructured grids for electric and magnetic field quantities [81]. It involves the space-time discretization of the whole domain and the solution of Maxwell's differential equations in a direct discretized form. Like other DE approaches, it uses appropriate boundary conditions to truncate the problem space. In stabilities in the form of spurious resonances may arise from improper time stepping. Time step is usually done using the Courant Friedrichs Levy (CFL) criterion [82]. Problems may arise when trying to modeling across different time scales and space in a simulation. A major advantage of this approach is the treatment of non-linear phenomenon in inhomogeneous media.

In the FDTD method, finite difference equations are used to solve Maxwell's equations for a restricted computational domain. The method requires the whole computational domain to be discretized, into volume



elements (cells) for which Maxwell's equations have to be solved. The cell size should not exceed  $\lambda/10$ , where  $\lambda$  is the wavelength corresponding to the highest frequency in the excitation. After discretizing the structure, the electromagnetic field components,  $E_x$ ,  $E_y$ ,  $E_z$ ,  $H_x$ ,  $H_y$ , and  $H_z$ , are defined for the cells, as illustrated in Figure 3.1.

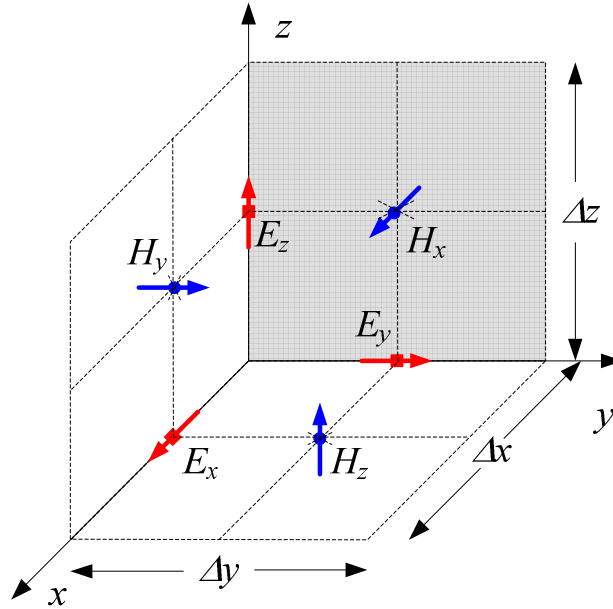


**Figure 3.1: FDTD cell with indicated electromagnetic field components**

If the field components are defined as in Figure 3.1, the resulting FDTD method is based according to the well known Yee formulation [81]. For a rectangular coordinate system the electromagnetic fields can be derived as follows.

Considering the second equation of (3.1) and using Ohm's law in (3.16) of the relation of the current density and electric field intensity, the following equation is obtained.

$$\nabla \times \mathbf{H} = \varepsilon \frac{\partial \mathbf{E}}{\partial t} + \mathbf{J} = \varepsilon \frac{\partial \mathbf{E}}{\partial t} + \sigma \mathbf{E} \quad (3.26)$$

Discretising (3.26) in time, the following equation is obtained:

$$\varepsilon \frac{\partial \mathbf{E}}{\partial t} + \sigma \mathbf{E} = \varepsilon \frac{\mathbf{E}^n - \mathbf{E}^{n-1}}{\Delta t} + \sigma \frac{\mathbf{E}^n + \mathbf{E}^{n-1}}{2} = \nabla \times \mathbf{H}, \quad (3.27)$$

where  $\Delta t$  is a selected time step.

Rearranging (3.27), the relation of electric field intensity at the time  $n$  and at the previous time step  $n-1$  is obtained as the following.

$$\mathbf{E}^n = \left( \frac{1 - \frac{\sigma \Delta t}{2\varepsilon}}{1 + \frac{\sigma \Delta t}{2\varepsilon}} \right) \mathbf{E}^{n-1} + \left( \frac{\frac{\Delta t}{\varepsilon}}{1 + \frac{\sigma \Delta t}{2\varepsilon}} \right) \nabla \times \mathbf{H} \quad (3.28)$$

Then, considering the first equation of (3.1) which is repeated here for clarity and discretising in time by shifting the half time step in the similar manner which is employed for calculating electric field intensity, the following equation is obtained.

$$\nabla \times \mathbf{E} = -\mu \frac{\partial \mathbf{H}}{\partial t}$$

$$\frac{\partial \mathbf{H}}{\partial t} = \frac{\mathbf{H}^{n+1/2} - \mathbf{H}^{n-1/2}}{\Delta t} = -\frac{1}{\mu} \nabla \times \mathbf{E} \quad (3.29)$$

Rearranging (3.29), the relation of magnetic field intensity at the time  $n+1/2$  and at the previous time step  $n-1/2$  is obtained as the following.

$$\mathbf{H}^{n+1/2} = \mathbf{H}^{n-1/2} - \frac{\Delta t}{\mu} \nabla \times \mathbf{E} \quad (3.30)$$

Finally, approximate partial derivatives in space using finite difference expressions, results in the FDTD equations from (3.28) and (3.30) can be derived  $E_x$ ,  $E_y$ ,  $E_z$ ,  $H_x$ ,  $H_y$ , and  $H_z$  as follows:

$$E_x^n \left( i + \frac{1}{2}, j, k \right) = K_1 E_x^{n-1} \left( i + \frac{1}{2}, j, k \right) + K_2 \times \left\{ H_z^{n-1/2} \left( i + \frac{1}{2}, j + \frac{1}{2}, k \right) - H_z^{n-1/2} \left( i + \frac{1}{2}, j - \frac{1}{2}, k \right) - H_y^{n-1/2} \left( i + \frac{1}{2}, j, k + \frac{1}{2} \right) + H_y^{n-1/2} \left( i + \frac{1}{2}, j, k - \frac{1}{2} \right) \right\} \quad (3.31)$$

$$E_y^n \left( i, j + \frac{1}{2}, k \right) = K_1 E_y^{n-1} \left( i, j + \frac{1}{2}, k \right) + K_2 \times \left\{ H_x^{n-1/2} \left( i, j + \frac{1}{2}, k + \frac{1}{2} \right) - H_x^{n-1/2} \left( i, j + \frac{1}{2}, k - \frac{1}{2} \right) - H_z^{n-1/2} \left( i + \frac{1}{2}, j + \frac{1}{2}, k \right) + H_z^{n-1/2} \left( i - \frac{1}{2}, j + \frac{1}{2}, k \right) \right\} \quad (3.32)$$

$$E_z^n \left( i, j, k + \frac{1}{2} \right) = K_1 E_z^{n-1} \left( i, j, k + \frac{1}{2} \right) + K_2 \times \left\{ H_y^{n-1/2} \left( i + \frac{1}{2}, j, k + \frac{1}{2} \right) - H_y^{n-1/2} \left( i - \frac{1}{2}, j, k + \frac{1}{2} \right) - H_x^{n-1/2} \left( i, j + \frac{1}{2}, k + \frac{1}{2} \right) + H_x^{n-1/2} \left( i, j - \frac{1}{2}, k + \frac{1}{2} \right) \right\} \quad (3.33)$$

$$H_x^{n+1/2} \left( i, j + \frac{1}{2}, k + \frac{1}{2} \right) = H_x^{n-1/2} \left( i, j + \frac{1}{2}, k + \frac{1}{2} \right) + K_3 \times \left\{ E_z^n \left( i, j + \frac{1}{2}, k + \frac{1}{2} \right) - E_z^n \left( i, j, k + \frac{1}{2} \right) - E_y^n \left( i, j + \frac{1}{2}, k + \frac{1}{2} \right) + E_y^n \left( i, j + \frac{1}{2}, k \right) \right\} \quad (3.34)$$

$$H_y^{n+1/2}\left(i+\frac{1}{2}, j, k+\frac{1}{2}\right) = H_y^{n-1/2}\left(i+\frac{1}{2}, j, k+\frac{1}{2}\right) + K_3 \left\{ E_x^n\left(i+\frac{1}{2}, j, k+1\right) - E_x^n\left(i+\frac{1}{2}, j, k\right) - E_z^n\left(i+1, j, k+\frac{1}{2}\right) + E_z^n\left(i, j, k+\frac{1}{2}\right) \right\} \quad (3.35)$$

$$H_z^{n+1/2}\left(i+\frac{1}{2}, j+\frac{1}{2}, k\right) = H_z^{n-1/2}\left(i+\frac{1}{2}, j+\frac{1}{2}, k\right) + K_3 \left\{ E_y^n\left(i+1, j+\frac{1}{2}, k\right) - E_y^n\left(i, j+\frac{1}{2}, k\right) - E_x^n\left(i+\frac{1}{2}, j+1, k\right) + E_x^n\left(i+\frac{1}{2}, j, k\right) \right\} \quad (3.36)$$

where  $K_1 = \frac{1 - \frac{\sigma \Delta t}{2\varepsilon}}{1 + \frac{\sigma \Delta t}{2\varepsilon}}$ ,  $K_2 = \frac{\frac{\Delta t}{\varepsilon}}{1 + \frac{\sigma \Delta t}{2\varepsilon}}$ , and  $K_3 = -\frac{\Delta t}{\mu}$ .

Initial conditions which are source excitations and special treatment on a cell for the thin wire structure [83], and lump elements must be specified for each discrete point in the discretized structure.

In lightning surge simulations, accurate modeling of a thin wire is necessary to represent transmission wires and steel frames of towers and buildings. The formulation of a thin wire of which radius is smaller than a discretized cell was proposed by T. Noda and S. Yokoyama [83] and improved by Taniguchi and Baba [84] for solving an instability problem from a thin wire of which radius is smaller than few percent of a cell size ( $0.1 \Delta s$ ).

The thin wire formulation corrects its surge impedance by modification of permittivity and permeability of the four enclosed cell around the wire. The artificial relative permittivity,  $m$  can be derived from the relation that the capacitance of a real system shall be equal of an artificial system as given in (3.37):

$$\frac{2\pi\varepsilon}{\ln(\Delta s/r)} = \frac{2\pi m\varepsilon}{\ln(\Delta s/r_0)} \text{ or } m = \frac{\ln(\Delta s/r_0)}{\ln(\Delta s/r)} \quad (3.37)$$

where  $r$  is an actual radius of the wire and  $r_0$  is an artificial radius of the wire.

From the results analyzed by Noda [83], the artificial radius of wire is related to a cell size,  $\Delta s$  as the following.

$$r_0 = 0.2298\Delta s \quad (3.38)$$

Substituting (3.38) into (3.37), the artificial permittivity is calculated as the following.

$$m = \frac{1.4705}{\ln(\Delta s/r)} \quad (3.39)$$

The artificial permittivity,  $m\varepsilon$  is applied to the four enclosed cell. To keep the speed of electromagnetic wave in the artificial enclosed cell equal to the speed in the actual media, the artificial permeability,  $\mu/m$  is also applied to the enclosed cells

A voltage source and a current source are derived readily by interpretation these into electromagnetic fields. The voltage is related to electric field intensity and the current is related to magnetic field intensity via the second equation of (2.1).

The formulation of a voltage source in the z direction is given as the following.

$$E_z^{n-1}(i, j, k + \frac{1}{2}) = \frac{V(n\Delta t)}{\Delta z} \quad (3.40)$$

The formulation of a current source in the z direction is derived by starting from the second equation of (3.1) which is repeated here.

$$\nabla \times \mathbf{H} = \epsilon \frac{\partial \mathbf{E}}{\partial t} + \mathbf{J}_e.$$

Discretizing the above equation in time, the following equation is obtained.

$$\begin{aligned} E_z^n(i, j, k + \frac{1}{2}) &= E_z^{n-1}(i, j, k + \frac{1}{2}) + \frac{\Delta t}{\epsilon} \nabla \times \mathbf{H}^{n-1/2} - \frac{\Delta t}{\epsilon} J_e \\ E_z^n(i, j, k + \frac{1}{2}) &= E_z^{n-1}(i, j, k + \frac{1}{2}) + \frac{\Delta t}{\epsilon} \nabla \times \mathbf{H}^{n-1/2} - \frac{\Delta t}{\epsilon \Delta x \Delta y} I_e^{n-1/2} \end{aligned} \quad (3.41)$$

For the voltage and current source in x and y directions can be derived and employed by the similar manner.

Simple lumped elements, a resistor, a capacitor and an inductor ( $R$ ,  $C$ , and  $L$ ), can be interpreted and derived in the similar manner. The  $R$ ,  $L$ , and  $C$  formulations in the z direction are derived and given. For the  $R$ ,  $L$ , and  $C$  in x and y directions can be derived and employed in the similar manner.

The formulation of a resistor paralleled with a capacitor ( $RC$ ) in the z direction is derived by starting from consideration of a current  $I_L$  flowing into the  $RC$ .

$$I_L = \frac{V}{R} + C \frac{dV}{dt} \quad (3.42)$$

Discretizing (3.42) in time, the following equation is obtained:

$$\begin{aligned} I_L^{n-1/2} &= \frac{\Delta z}{2R} (E_z^n + E_z^{n-1}) + \frac{C\Delta z}{\Delta t} (E_z^n - E_z^{n-1}) \\ &= \left( \frac{\Delta z}{2R} + \frac{C\Delta z}{\Delta t} \right) E_z^n + \left( \frac{\Delta z}{2R} - \frac{C\Delta z}{\Delta t} \right) E_z^{n-1} \end{aligned} \quad (3.43)$$

Rearranging (3.43), the following equation is obtained:

$$E_z^n(i, j, k + \frac{1}{2}) = \left( \frac{1 + \frac{C\Delta z}{\epsilon \Delta x \Delta y} - \frac{\Delta z \Delta t}{2R\epsilon \Delta x \Delta y}}{1 + \frac{C\Delta z}{\epsilon \Delta x \Delta y} + \frac{\Delta z \Delta t}{2R\epsilon \Delta x \Delta y}} \right) E_z^{n-1}(i, j, k + \frac{1}{2}) + \left( \frac{\Delta t / \epsilon}{1 + \frac{C\Delta z}{\epsilon \Delta x \Delta y} + \frac{\Delta z \Delta t}{2R\epsilon \Delta x \Delta y}} \right) \nabla \times \mathbf{H}^{n-1/2} \quad (3.44)$$

The formulation of a pure resistor is obtained by substituting  $C$  by zero in (3.44).

$$E_z^n(i, j, k + \frac{1}{2}) = \frac{\left(1 - \frac{\Delta z \Delta t}{2R\epsilon\Delta x\Delta y}\right)}{\left(1 + \frac{\Delta z \Delta t}{2R\epsilon\Delta x\Delta y}\right)} E_z^{n-1}(i, j, k + \frac{1}{2}) + \frac{\Delta t / \epsilon}{\left(1 + \frac{\Delta z \Delta t}{2R\epsilon\Delta x\Delta y}\right)} \nabla \times \mathbf{H}^{n-1/2} \quad (3.45)$$

The formulation of a pure capacitor is obtained by substituting  $R$  by zero in (3.44).

$$E_z^n(i, j, k + \frac{1}{2}) = E_z^{n-1}(i, j, k + \frac{1}{2}) + \frac{\Delta t / \epsilon}{\left(1 + \frac{C\Delta z}{\epsilon\Delta x\Delta y}\right)} \nabla \times \mathbf{H}^{n-1/2} \quad (3.46)$$

The formulation of an inductor  $L$  in the  $z$  direction is derived by starting from consideration of a current  $I_L$  flowing into the  $L$ .

$$I_L = \frac{1}{L} \int_0^t V_L(\tau) d\tau \quad (3.47)$$

Discretizing (3.47) in time, the following equation is obtained:

$$I_L^{n-1/2} = \frac{1}{L} \int_0^{(n-1/2)\Delta t} V_L(\tau) d\tau = \frac{\Delta z}{L} \int_0^{(n-1/2)\Delta t} E_z(\tau) d\tau \quad (3.48)$$

Rearranging (3.48), the following equation is obtained:

$$E_z^n(i, j, k + \frac{1}{2}) = E_z^{n-1}(i, j, k + \frac{1}{2}) + \frac{\Delta t}{\epsilon} (\nabla \times \mathbf{H}^{n-1/2})_z - \frac{\Delta z(\Delta t)}{\epsilon L \Delta x \Delta y} \sum_{m=1}^{n-1} E_z^m \quad (3.49)$$

Many problems in EMI/EMC simulations involve open region problems that are impossible to discretize a whole domain in the FDTD method due to limitation of computer memory. This problem can be solved using mathematical formulations, absorbing boundary conditions, such as Mur's absorbing boundary formulation, Liao's absorbing boundary formulation, a perfect matching layer absorbing boundary formulation.

To ensure that the electromagnetic wave propagation between the nodes does not exceed the speed of light a time step condition, Courant condition [82], has to be fulfilled. The Courant condition for three dimensional models is given by:

$$\Delta t \leq \frac{1}{c \sqrt{\frac{1}{\Delta x^2} + \frac{1}{\Delta y^2} + \frac{1}{\Delta z^2}}}, \quad (3.50)$$

where  $\Delta x$ ,  $\Delta y$ , and  $\Delta z$  are the cell sizes and  $c$  the propagation speed between the nodes.

The procedure of the FDTD calculation is the following:

- 1) Using (3.31) to (3.33) to calculate the electric field components for the complete structure,
- 2) Advance time by  $\Delta t/2$ ,
- 3) Using (3.34) to (3.36) to calculate the magnetic field components for the complete structure based on the electric field components,
- 4) Advance time by  $\Delta t/2$  and continue to 1).

The FDTD method yields the results in field variables,  $\mathbf{E}$  and  $\mathbf{H}$ , at all locations in the discretized domain and at every time point. To obtain currents and voltages post-processing is required.

### 3.3.2 Transmission line matrix 'TLM'

The transmission-line matrix (TLM) method is a 3 dimensional time domain method for the computation of electromagnetic fields. The method [85,86] is based on the analogy between the electromagnetic field and transmission lines. The TLM method is similar to the FDTD method. However, instead of interleaving E-field and H-field grids, a single grid is defined, the nodes of which are interconnected through virtual transmission lines (see Figure 3.2).

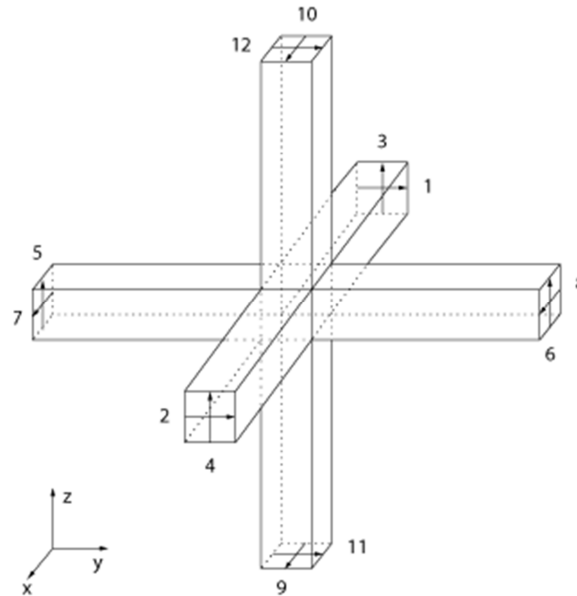


**Figure 3.2: FDTD cell with indicated electromagnetic field components**

Absorbing boundary conditions can be established in TLM method in a straightforward way by terminating each transmission line to its characteristic impedance. Different methods for implementing absorbing boundary conditions have been proposed in the literature (see e.g. [87-91]).

The TLM method is characterized by the same advantages as those of the FDTD method [92], most importantly the ability of handling nonlinear materials. The TLM method, however, features a better performance compared to that of the FDTD when dealing with complex boundary geometries. On the other hand, TLM methods require more computer memory per node than does FDTD [93].

### 3.3.3 Finite-element method in time domain (FEMTD)

The Finite Element Method (FEM) is a numerical method for finding approximate solutions of partial differential equations (PDEs). This method has a long tradition and its beginnings can be traced back to the publications of A. Hrennikoff [94] and R. Courant [95] in 1941 and 1942 respectively. The pioneering applications of the finite element method were related to the problems of structural analysis for aircraft design.

It took a relatively long time (almost 25 years) for FEM to be adopted by the electromagnetic field community. The first FEM application in electrical engineering was reported by Winslow in 1965 [96] and the first nonlinear variation formulation of electromagnetic field problems in electrical machines was published by Silvester and Chari in 1970 [97].

The initial FEM applications in electromagnetics were based on triangular and rectangular (2D) or tetrahedral and hexahedral (3D) nodal scalar elements, as shown in Figure 3.2. The capability to use an unstructured mesh allows FEM users to describe complex real-life geometries with great flexibility, which is one of the main advantages of this method.

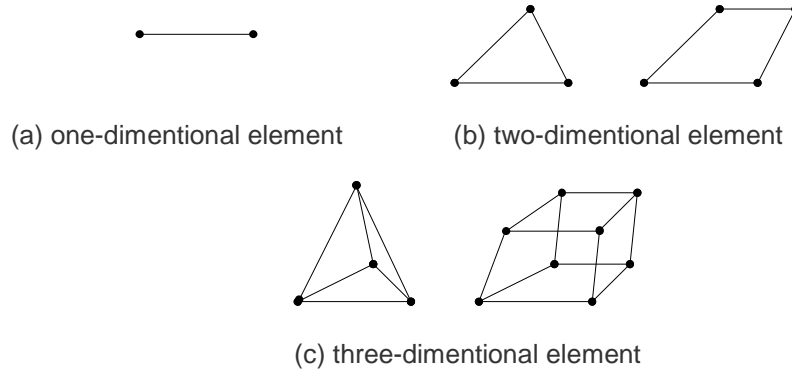


**Figure 3.2: Typical finite elements used in the discretization**

As the FEM applications entered the field of electrodynamics (eddy-currents, wave propagation, etc.), several numerical problems attributed to the nodal scalar elements were recognized: (a) generation of spurious solutions due to the lack of enforcement of the divergence condition, (b) difficulties in imposing boundary conditions over the interfaces between different materials, and (c) difficulty in treating conducting and dielectric edges and corners due to the associated field singularities [98].

The revolutionary approach for solving the mentioned numerical problems associated with the nodal scalar elements was developed relatively recently. Namely, in 1980 J.C. Nedelec developed and published the basic scheme of the vector edge elements [99]. He actually rediscovered and extended the work of H. Whitney on vector shape functions [100] published in 1957. The first concrete application of vector elements to electrodynamics (eddy-current problems) was done by A. Bossavit and J. C. Verite in 1982 [101]. The vector finite elements are widely used today in both research and industrial product development since they are a core component of the most successful commercial software solutions for electrodynamic simulations.

Concerning the full-wave electromagnetic simulations in time-domain, there are several different field formulations that can be used for numerical simulations. However, the main principle of the FEM discretization of the vector field equations by using vector elements is not dependent on the chosen field formulation. Thus, without the loss of generality, we can present the 3D full-wave FEM electromagnetic analysis in time-domain starting from the following field formulation based on the vector magnetic potential [98,102]:

$$\mu_0 \frac{\partial}{\partial t} \left( \epsilon_0 \epsilon_r \frac{\partial \vec{A}}{\partial t} \right) + \mu_0 \sigma \frac{\partial \vec{A}}{\partial t} + \nabla \times \left( \frac{1}{\mu_r} \nabla \times \vec{A} \right) = 0 \text{ in } \Omega \subset R^3 \quad (3.51)$$

$$\vec{n} \times \vec{A} = 0 \text{ over } \partial_{PEC} \Omega \subset R^2 \quad (3.52)$$

$$-\vec{n} \times \left( \frac{1}{\mu_r} \nabla \times \vec{A} \right) - \frac{\mu_0}{Z_s} \frac{\partial}{\partial t} \vec{n} \times (\vec{n} \times \vec{A}) = \frac{2\mu_0}{Z_s} \vec{n} \times (\vec{n} \times \vec{E}_0) \text{ over } \partial_{PORT} \Omega \subset R^2 \quad (3.53)$$

Where  $\vec{A}$  is the vector magnetic potential,  $\mu = \mu_r \mu_0$  is the magnetic permeability of the domain,  $\mu_0$  is the magnetic permability of vacuum,  $\epsilon = \epsilon_r \epsilon_0$  is the dielectric permittivity of the domain,  $\epsilon_0$  is the dielectric permittivity of vacuum,  $\sigma$  is the electric conductivity of the domain,  $\Omega$  is the 3D computational domain,  $\partial_{PEC} \Omega$  is the perfect electric conductor boundary of the domain (metal conductor at high frequencies),  $\partial_{PORT} \Omega$  is the connecting port boundary of the domain over which is its connection with the external source is established,  $\vec{E}_0$  is the source

electric field (voltage source) over the connecting boundary, and  $Z_s = \sqrt{\frac{\mu}{\epsilon}}$  is the surface wave impedance (can be also an impendence of the conductors system attached to the computational domain over the interface boundary).

If the computational domain is truncated by a surface from the surrounding open space, then Equation (3.53) can also be used as a boundary condition (BC) but its right hand side is equal to zero and it is then called the Absorbing Boundary Condition (ABC) of first order [98].

The problem described by Equations (3.51-3.53) is the so-called boundary value problem (BVP). Before we start the FEM discretization of this BVP, the equivalent weak-form of the BVP must be obtained [98]. This step will be done by applying the Galerkin version of the weighted residual method [98]:

$$\begin{aligned} & \int_{(\Omega)} \vec{N}_i \cdot \left[ \mu_0 \frac{\partial}{\partial t} \left( \epsilon_0 \epsilon_r \frac{\partial \vec{A}}{\partial t} \right) + \mu_0 \sigma \frac{\partial \vec{A}}{\partial t} + \nabla \times \left( \frac{1}{\mu_r} \nabla \times \vec{A} \right) \right] dV + \\ & + \int_{(\partial_{PORT} \Omega)} \vec{N}_i \cdot \left[ -\vec{n} \times \left( \frac{1}{\mu_r} \nabla \times \vec{A} \right) - \frac{\mu_0}{Z_s} \frac{\partial}{\partial t} \vec{n} \times (\vec{n} \times \vec{A}) \right] dS = \int_{(\partial_{PORT} \Omega)} \vec{N}_i \cdot \left[ \frac{2\mu_0}{Z_s} \vec{n} \times (\vec{n} \times \vec{E}_0) \right] dS = 0 \end{aligned} \quad (3.54)$$

Evidently, Equation (3.54) was obtained by weighting the residual of the PDE and the corresponding BCs with the vector weighting functions  $\vec{N}_i$  and by integrating it over the corresponding volume and boundary surfaces.

If we apply the well-known vector derivative formula  $\nabla \cdot (\vec{a} \times \vec{b}) = \vec{b} \cdot (\nabla \times \vec{a}) - \vec{a} \cdot (\nabla \times \vec{b})$  and the divergence theorem  $\int_{(\Omega)} \nabla \cdot \vec{a} dV = \oint_{\partial \Omega} \vec{a} \cdot d\vec{S}$ , it is relatively simple to transform Equation (3.54) into the following form:

$$\begin{aligned} & \int_{(\Omega)} \frac{1}{\mu_r} \nabla \times \vec{A} \cdot \nabla \times \vec{N}_i dV + \int_{(\Omega)} \vec{N}_i \cdot \left[ \mu_0 \frac{\partial}{\partial t} \left( \epsilon_0 \epsilon_r \frac{\partial \vec{A}}{\partial t} \right) + \mu_0 \sigma \frac{\partial \vec{A}}{\partial t} \right] dV + \\ & - \int_{\partial_{PORT} \Omega} \vec{N}_i \cdot \left[ \frac{\mu_0}{Z_s} \frac{\partial}{\partial t} \vec{n} \times (\vec{n} \times \vec{A}) \right] dS = \int_{\partial_{PORT} \Omega} \vec{N}_i \cdot \left[ \frac{2\mu_0}{Z_s} \vec{n} \times (\vec{n} \times \vec{E}_0) \right] dS \end{aligned} \quad (3.55)$$

The obtained form (3.55) is called the weak-form as it contains only spatial derivatives of the first order. Equation (3.55) is suitable for the subsequent FEM discretization.

To better understand the vector FEM discretization and the properties of the vector edge elements it is necessary to define the scalar nodal element and its shape functions and to summarize its properties. For this reason let us consider a linear nodal tetrahedral element presented in Figure 3.3.

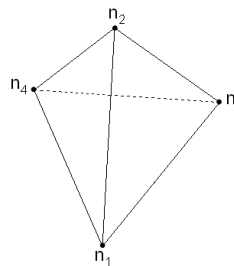


**Figure 3.3: Linear nodal tetrahedral element**



An unknown scalar function  $\Phi(x, y, z, t)$  is approximated in the linear nodal tetrahedron in the following way:

$$\Phi^e(x, y, z, t) = \sum_{i=1}^4 N_i^e(x, y, z) \cdot \Phi_i^e(t) \quad (3.56)$$

Where  $N_i^e(x, y, z)$  is the linear scalar shape function of the node  $i$  (1,2,3, or 4) of the element  $e$ , and  $\Phi_i^e$  are the unknown coefficients that represent the values of the unknown function at the element's nodes. If the element is linear, the nodal shape functions have the following form:

$$N_i^e(x, y, z) = a_i^e + b_i^e x + c_i^e y + d_i^e z, \quad i = 1, 2, 3, 4 \quad (3.57)$$

Where  $a_i^e$ ,  $b_i^e$ ,  $c_i^e$ , and  $d_i^e$  are the unknown approximation coefficients that are easily obtained by enforcing the mathematical constraints such that the shape function must be equal to 1 at the corresponding node and equal to 0 at the remaining three nodes [98]. The scalar shape functions of the linear tetrahedron are shown in Figure 3.4.

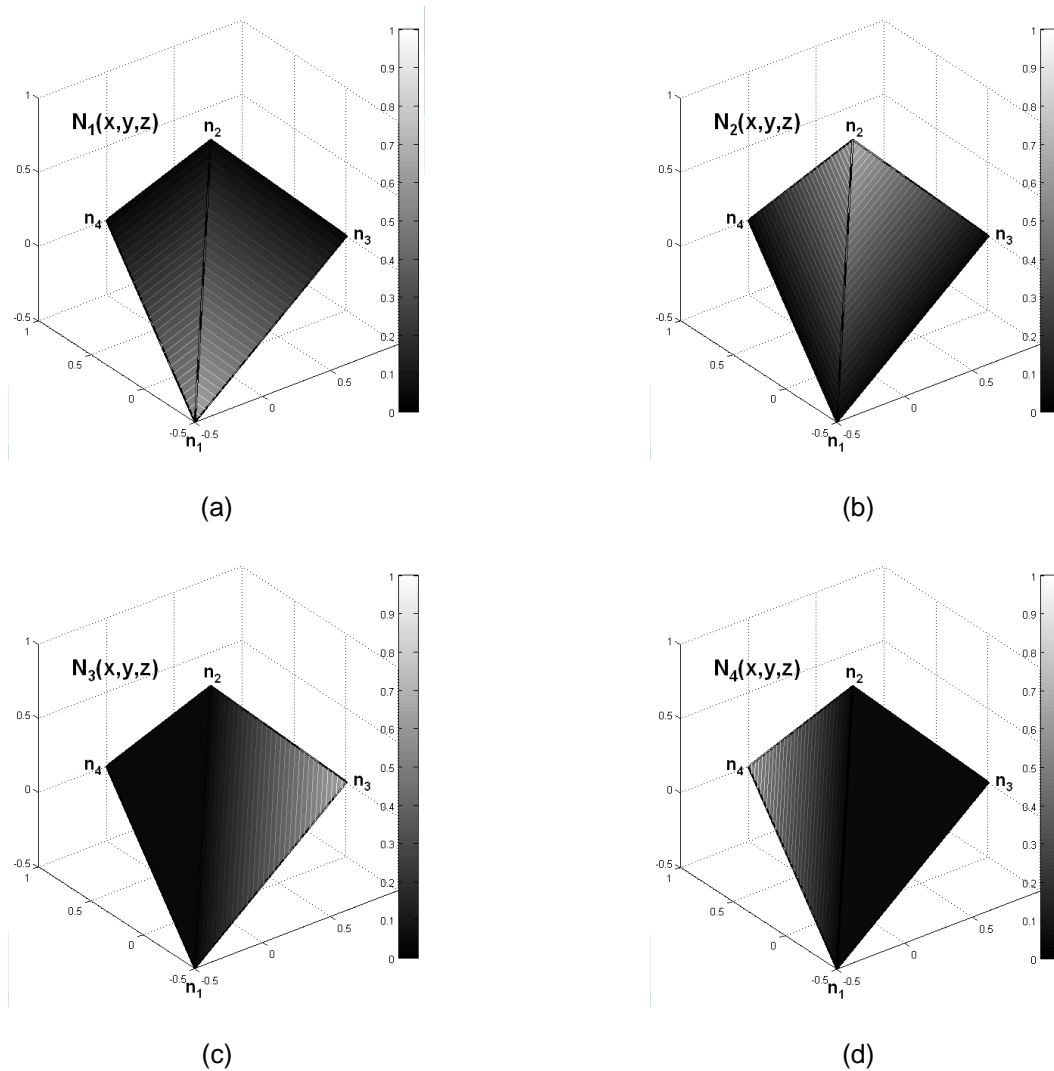


**Figure 3.4: The nodal (scalar) shape functions of the linear tetrahedron**

Based on the nodal (scalar) shape functions defined by (3.56 and 3.57), in 1957 H. Whitney defined the following edge (vector) shape functions of the linear tetrahedron:

$$\vec{N}_k^e(x, y, z) = l_k^e \cdot \vec{W}_{ij}^e(x, y, z) = l_k^e \cdot [N_i^e(x, y, z) \cdot \nabla N_j^e(x, y, z) - N_j^e(x, y, z) \cdot \nabla N_i^e(x, y, z)] \quad (3.58)$$

Where  $i$  and  $j$  are the node indices (1,2,3, or 4),  $k$  is the edge index (1,2,...,6),  $N_i^e$  is the nodal shape function related to the node  $i$ ,  $\vec{W}_{ij}^e$  is the vector shape function related to the edge between the node  $i$  and node  $j$ ,  $l_k^e$  is the length of the edge  $k$ , and  $\vec{N}_k^e$  is the normalized vector shape function related to the edge  $k$ . The vector shape function  $\vec{N}_1^e$  over two faces of the linear tetrahedron is shown in Figure 3.5.

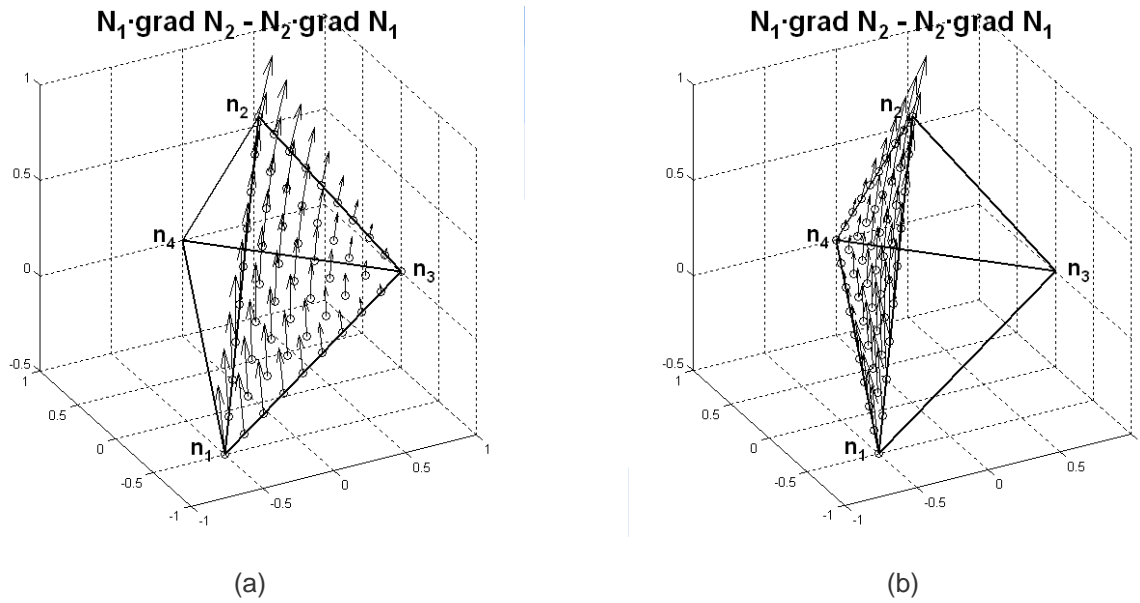


**Figure 3.5 The edge (vector) shape function related to the edge 1 between the nodes 1 and 2 of the linear tetrahedron**

It is not difficult to show that the vector shape functions have the following important properties:

$$\nabla \cdot \vec{W}_{ij}^e = \nabla \cdot (N_i^e \nabla N_j^e) - \nabla \cdot (N_j^e \nabla N_i^e) = 0 \quad (3.59)$$

$$\nabla \times \vec{W}_{ij}^e(x, y) = \nabla \times (N_i^e \nabla N_j^e) - \nabla \times (N_j^e \nabla N_i^e) = 2 \nabla N_i^e \times \nabla N_j^e \quad (3.60)$$

An unknown vector field  $\vec{A}$  is approximated within the vector tetrahedron as follows:

$$\vec{A}^e(x, y, z, t) = \sum_{i=1}^6 \vec{N}_i^e(x, y, z) \cdot A_i^e(t), \quad A_i^e(t) = \vec{e}_i \cdot \vec{A}(x_{ei}^e, y_{ei}^e, z_{ei}^e, t) \quad (3.61)$$

Where  $\vec{e}_i$  is the unit vector that represents the direction of the tetrahedron edge  $i$ .

Since a scalar shape function is a local function, i.e. since it is different from zero only within those elements that contain its reference node, a vector shape function also has this property. Thus the vector shape function will be

different from zero only within the elements that contain its reference edge. Thus the local (elemental) field expansion (3.61) can be easily generalized into a global field expansion:

$$\vec{A}(x, y, z, t) = \sum_{i=1}^N \vec{N}_i(x, y, z) \cdot A_i(t) \quad (3.62)$$

Where N is the number of edges of the mesh.

If the approximation (3.62) is included into the weak form (3.55) the following equation is obtained:

$$\begin{aligned} & \sum_{j=1}^N \int_{(\Omega)} \frac{1}{\mu_0 \mu_r} [\nabla \times \vec{N}_i(\vec{r})] \cdot [\nabla \times \vec{N}_j(\vec{r})] A_j(t) dV + \sum_{j=1}^N \int_{(\Omega)} \epsilon_0 \epsilon_r \vec{N}_i(\vec{r}) \cdot \vec{N}_j(\vec{r}) \frac{\partial^2 A_j}{\partial t^2}(t) dV + \\ & + \sum_{j=1}^N \int_{(\Omega)} \sigma \vec{N}_i(\vec{r}) \cdot \vec{N}_j(\vec{r}) \frac{\partial A_j}{\partial t}(t) dV - \sum_{j=1}^N \int_{\partial_{PORT} \Omega} \frac{1}{Z_S} [\vec{n} \times \vec{N}_i(\vec{r})] \cdot [\vec{n} \times \vec{N}_j(\vec{r})] \frac{\partial A_j}{\partial t}(t) dS = \\ & = \int_{\partial_{PORT} \Omega} \vec{N}_i \cdot \left[ \frac{2}{Z_S} \vec{n} \times (\vec{n} \times \vec{E}_0) \right] dS, \quad i = 1, 2, \dots, N \end{aligned} \quad (3.63)$$

The system of equations (3.63) can be written in the following matrix form:

$$[T] \frac{\partial^2 \{A\}}{\partial t^2}(t) + ([R] - [Q]) \frac{\partial \{A\}}{\partial t}(t) + [S] \{A\}(t) = \{f\}(t) \quad (3.64)$$

$$T_{ij} = \int_{(\Omega)} \epsilon_0 \epsilon_r \vec{N}_i(\vec{r}) \cdot \vec{N}_j(\vec{r}) dV \quad (3.65)$$

$$R_{ij} = \int_{(\Omega)} \sigma \vec{N}_i(\vec{r}) \cdot \vec{N}_j(\vec{r}) dV \quad (3.66)$$

$$Q_{ij} = \int_{\partial_{PORT} \Omega} \frac{1}{Z_S} [\vec{n} \times \vec{N}_i(\vec{r})] \cdot [\vec{n} \times \vec{N}_j(\vec{r})] dS \quad (3.67)$$

$$S_{ij} = \int_{(\Omega)} \frac{1}{\mu_0 \mu_r} [\nabla \times \vec{N}_i(\vec{r})] \cdot [\nabla \times \vec{N}_j(\vec{r})] dV \quad (3.68)$$

$$f_i = \int_{\partial_{PORT} \Omega} \vec{N}_i \cdot \left[ \frac{2}{Z_S} \vec{n} \times (\vec{n} \times \vec{E}_0) \right] dS \quad (3.69)$$

Evidently, the finite element method was used to discretize the BVP (3.51-3.53) in space and the process has yielded the ordinary differential matrix equation (3.64). The obtained matrices (3.65-3.68) are large square sparse matrices, due to the local character of the vector shape functions.

The ordinary differential equation (3.64) can be discretized in time-domain by using several theoretically very well investigated schemes [98]: (a) forward difference scheme, (b) backward difference scheme, (c) central difference scheme, and (d) Newmark method. Considering the stability of the time-domain solution process we will choose here the backward difference scheme because it is absolutely stable, i.e. the stability is independent from the time-step. The backward difference scheme is based on the following approximations of the time derivatives:

$$\frac{\partial \{A\}}{\partial t} \approx \frac{\{A\}^n - \{A\}^{n-1}}{\Delta t}, \quad \frac{\partial^2 \{A\}}{\partial t^2} \approx \frac{\{A\}^n - 2\{A\}^{n-1} + \{A\}^{n-2}}{\Delta t^2} \quad (3.70)$$

By following this scheme the ordinary differential equation (3.64) becomes:

$$\left( \frac{[T]}{\Delta t^2} + \frac{[R] - [Q]}{\Delta t} + [S] \right) \{A\}^{n+1} = \left( \frac{2[T]}{\Delta t^2} + \frac{[R] - [Q]}{\Delta t} \right) \{A\}^n - \frac{[T]}{\Delta t^2} \{A\}^{n-1} - \{f\}^{n+1} \quad (3.71)$$

Evidently, the discretization by using the backward difference scheme (3.70) yields the iterative procedure (3.71) within which the solution of the next time step ( $\{A\}^{n+1}$ ) is obtained from the solution of the preceding two steps ( $\{A\}^n$  and  $\{A\}^{n-1}$ ) and from the excitation ( $\{f\}^{n+1}$ ). Therefore this scheme is called an implicit scheme [98]. The main advantage of the scheme is that it is absolutely stable and the main drawback is that it requires a solution of the large sparse system of equation in each time step.

The presented FEM approach in time-domain is generally numerically stable, robust in terms of the mesh quality and size, and very suitable for industrial applications with complicated 3D geometries [103].

### 3.4 Integral equation based approach

A good advantage of the integral equation based (IE) methods over the differential equation based methods is to solve the open space problem without employing boundary condition to truncate the calculated domain. Discretization is carried out on only the boundary of considered material not on the whole space domain like DE based methods.

This section describes the basic theory of two representative methods based on the IEs, i.e. the MoM method and the PEEC method in brief detail. The detail of generalized PEEC method can be found in Chapter 3.

#### 3.4.1 Method of moment (MoM)

The method of moment (MoM) derived from electric field integral equation (EFIE) [99] is an IE based approach. The MoM in the frequency and time domains is widely used in analyzing responses of conducting structure to external electrodynamic fields. The entire conducting structure with and without loss is modeled by a combination of conducting segments.

For lightning surge analyses, the cylindrical thin wire is often modeled for a transmission line, a tower, and a building structure. In this section only the MoM of the thin wire structure in the free space is presented. The assumption of thin wire is that its radii are much smaller than and the wavelength of interest. In the MoM, the thin wire is segmented into a small wire of which radius is much smaller than its length. For simplicity the perfectly conducting thin wire in the air is considered as illustrated in Figure 3.3. Assuming current  $I$  and charge  $q$  are confined to the wire axis (thin wire approximation), the EFIE in the frequency domain from (3.19) is simplified to:

$$\mathbf{E}^i(\mathbf{r}) = j\omega\mu_0 \int_C I(\mathbf{r}') g(\mathbf{r}, \mathbf{r}') \mathbf{s}' ds' - \frac{\nabla}{j\omega\epsilon_0} \int_C g(\mathbf{r}, \mathbf{r}') \nabla \cdot (I(\mathbf{r}') \mathbf{s}') ds' \quad (3.58)$$

where  $\mathbf{s}$  is a unit tangential vector along  $C(\mathbf{r})$  and  $\mathbf{s}'$  is a unit tangential vector on the wire surface.

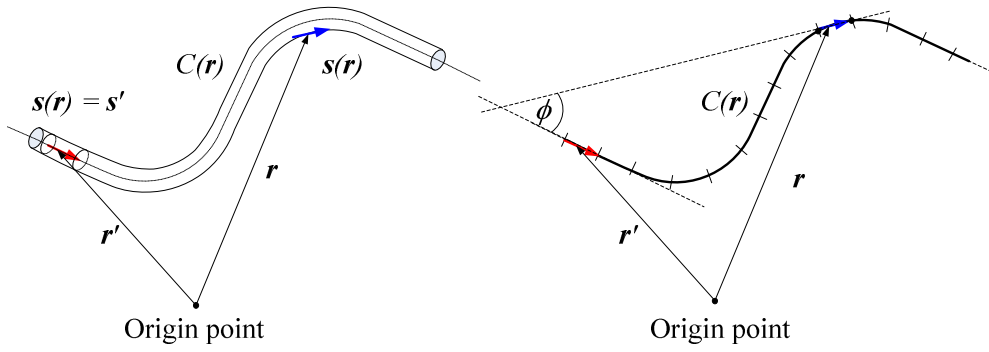


**Figure 3.3: Problem geometry**

Considering electric field intensity on the surface of a wire and dot producing a vector,  $\mathbf{s}$  with (3.58). The following equations is obtained.

$$\mathbf{s} \cdot \mathbf{E}^i(\mathbf{r}) = j\omega\mu_0 \int_C \mathbf{s} \cdot \mathbf{s}' I(\mathbf{r}') g(\mathbf{r}, \mathbf{r}') ds' - \mathbf{s} \cdot \frac{\nabla}{j\omega\epsilon_0} \int_C g(\mathbf{r}, \mathbf{r}') \nabla \cdot (I(\mathbf{r}') \mathbf{s}') ds' \quad (3.59)$$

or

$$\mathbf{s} \cdot \mathbf{E}^i(\mathbf{r}) = j\omega\mu_0 \int_C \mathbf{s} \cdot \mathbf{s}' I(\mathbf{r}') g(\mathbf{r}, \mathbf{r}') ds' + \frac{I}{j\omega\epsilon_0} \int_C \frac{\partial(I(\mathbf{r}') g(\mathbf{r}, \mathbf{r}'))}{\partial s \partial s'} ds' \quad (3.60)$$

Rearranging (3.60), the general form as the following is obtained:

$$\mathbf{s} \cdot \mathbf{E}^i(\mathbf{r}) = \frac{j\eta}{k} \int_C \left( k^2 \mathbf{s} \cdot \mathbf{s}' - \frac{\partial}{\partial s \partial s'} \right) I(\mathbf{r}') g(\mathbf{r}, \mathbf{r}') ds' \quad (3.61)$$

where  $k = \omega\sqrt{\mu_0\epsilon_0}$  and  $\eta = \sqrt{\frac{\mu_0}{\epsilon_0}}$ .

The derivation of the EFIE in the time domain is carried out in the similar manner of the frequency domain formulation by considering (3.22). The following result is obtained:

$$\mathbf{s} \cdot \mathbf{E}^i(\mathbf{r}, t) = \frac{\mu_0}{4\pi} \int_C \mathbf{s} \cdot \mathbf{s}' \frac{1}{R} \cdot \frac{\partial I(\mathbf{r}', t')}{\partial t'} ds' - \mathbf{s} \cdot \frac{\nabla}{4\pi\epsilon_0} \int_C \frac{q(\mathbf{r}', t')}{R} ds' \quad (3.62)$$

where  $q(\mathbf{r}', t') = -\int_{-\infty}^{t'} \frac{\partial I(\mathbf{r}', \tau)}{\partial s'} d\tau$ .

The last term of (3.62) can be derived and the following equation is obtained.

$$\begin{aligned}
 \nabla \left( \frac{q(\mathbf{r}', t')}{R} \right) &= \frac{\partial}{\partial R} \left( \frac{q(\mathbf{r}', t')}{R} \right) \frac{\mathbf{R}}{R} = q \frac{\partial(1/R)}{\partial R} + \frac{1}{R} \frac{\partial q}{\partial R} \\
 &= -\frac{1}{R^2} q + \frac{1}{R} \frac{\partial q}{\partial s'} \\
 &= -\frac{1}{R^2} q - \frac{1}{R} \frac{\partial q}{c \partial t'}
 \end{aligned} \tag{3.63}$$

Using the continuity in the one dimensional form which is given in (3.64), the last term of (3.62) can be written in (3.65).

$$\frac{\partial q}{\partial t'} = -\frac{\partial I}{\partial s'} \tag{3.64}$$

$$\nabla \left( \frac{q(\mathbf{r}', t')}{R} \right) = -\frac{1}{R^2} q + \frac{1}{Rc} \frac{\partial I}{\partial s'} \tag{3.65}$$

Substituting (3.65) into (3.62) and rearranging it, the EFIE in the time domain is obtained.

$$\mathbf{s} \cdot \mathbf{E}^i(\mathbf{r}, t) = \frac{\mu_0}{4\pi} \int_C \left\{ \mathbf{s} \cdot \mathbf{s}' \frac{1}{R} \cdot \frac{\partial I(\mathbf{r}', t')}{\partial t'} + c \frac{\mathbf{s} \cdot \mathbf{R}}{R^2} \frac{\partial I(\mathbf{r}', t')}{\partial s'} - c^2 \frac{\mathbf{s} \cdot \mathbf{R}}{R^3} \frac{q(\mathbf{r}', t')}{R} \right\} ds' \tag{3.66}$$

To solve (3.61) or (3.66), a function of a distributed current is to expand the unknown quantity using known functions weighted by unknown coefficients. The results are converted into a linear system of equations by enforcing the boundary conditions on the surface of each segmented wire. The resulting linear system is then solved numerically for the unknown coefficients. The linear system can be solved by a method of weighted residuals known as the method of moments (MoM). The generalized problem can be written in the following form.

$$L(f) = E \tag{3.67}$$

where  $L$  is a linear operator,  $E$  the excitation function and  $f$  the unknown current function,  $f$  can be expressed as a linear combination of basis functions weighted by unknown coefficients. The unknown function  $f(x)$  can be expanded in the following form:

$$f(x) = \sum_{n=1}^N a_n f_n(x), \tag{3.68}$$

where  $a_n$  is an unknown coefficient, and  $f_n(x)$  is a known basis function which is illustrated in Fig 3.4.

Substituting (3.68) into (3.67), the following equation is obtained:

$$\sum_{n=1}^N a_n L(f_n(x)) \approx E. \tag{3.69}$$

To solve (3.69), the inner product of weight function  $f_m$  is applied to (3.69). The following equation is obtained.

$$\sum_{n=1}^N a_n \langle f_m, L(f_n) \rangle \approx \langle f_m, E \rangle \tag{3.70}$$

The equation (3.70) can be written in a matrix form:

$$\mathbf{Z}\mathbf{a} = \mathbf{b}, \quad (3.71)$$

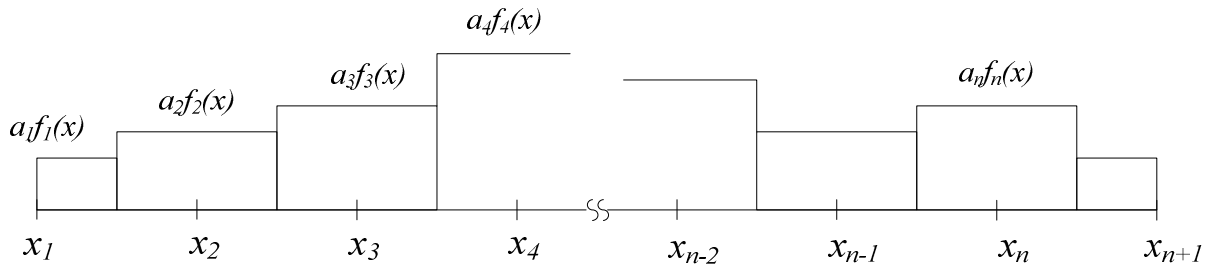
with

$$Z_{mn} = \langle f_m, L(f_n) \rangle \quad (3.72)$$

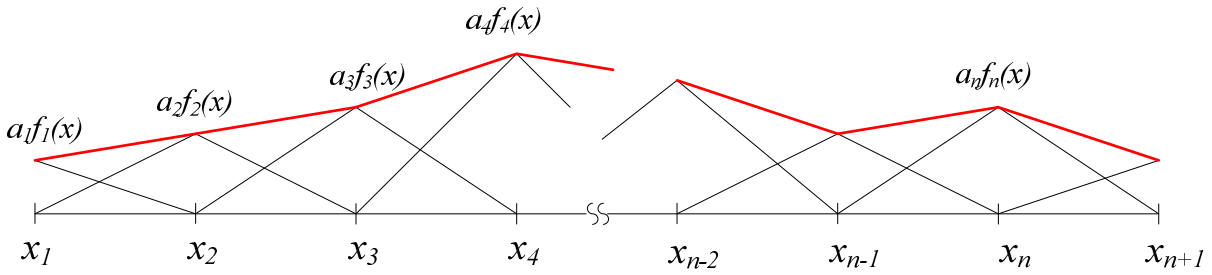
and

$$b_{mn} = \langle f_m, E \rangle \quad (3.73)$$

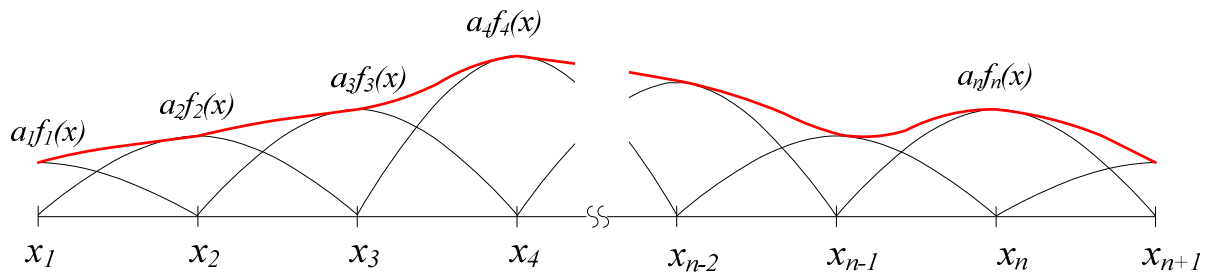
where  $z_{mn}$  is an element of the matrix  $\mathbf{Z}$  at row  $m$  and column  $n$ , and  $b_m$  is an element of the vector  $\mathbf{b}$  at row  $m$ .



(a) Piecewise pulse function.



(b) Piecewise triangular function.



(c) Piecewise sinusoidal function

**Figure 3.4: MoM typical basis functions**

The unknown coefficients of distributed currents are obtained by solving (3.71). To obtain the results in terms of field variables post-processing is needed for the conversion. The well-known computer program numerical electromagnetic code, often referred to as NEC [100], [101], utilizes the MoM for the calculation of the electromagnetic response for antennas and other metal structures in the frequency domain and thin wire time domain analysis (TWTD) code which is available in public domain [102].

### 3.4.2 Partial element equivalent circuit (PEEC) method

The partial element equivalent circuit (PEEC) [103] has been introduced by A. Ruehli in 1974. The PEEC method is also an IE based technique. It is based on the mixed potential integral equation (MFIE) from which an equivalent circuit is extracted. Despite the PEEC method provides full-wave solution, it was not primarily developed for calculation of electromagnetic fields. The PEEC method was strongly developed in the 1990s when retardation, excited fields, and treatment of dielectric material are investigated and included [104], [105].

Unlike differential equation based methods, the PEEC method gives fewer unknowns than differential equation based methods since it does not require discretization of the whole domain space. Though the resulting matrices are dense, recent fast solvers have greatly improved the solution time for PEEC simulations [106]. The main difference of PEEC from MoM is the possibility to extract equivalent circuits from the integral equations. The PEEC method yields potentials on potential cells and distributed currents on current cells without post-processing unlike the MoM yields only distributed currents. However, the number of unknowns in the PEEC method is about double when it compared with that of the MoM. The derivation of the MPIE and the detail of the generalized PEEC method can be found in Reference [107]-[110]

The first step for obtaining solution of the PEEC method starts from discretizing geometry structure into small cells that are composed of current cells and charge or potential cells. The current cells and potential cells are interleaved each other. The rectangular pulse is employed for both charge and current basis functions. Then Galerkin method is applied to enforce the integral equation that is written in the time domain.

$$\begin{aligned} \mathbf{E}^i(\mathbf{r}, t) = & \frac{\mathbf{J}(\mathbf{r}, t)}{\sigma} + \frac{\mu_0}{4\pi} \int_{V'} \frac{1}{R} \cdot \frac{\partial \mathbf{J}(\mathbf{r}', t')}{\partial t} dV' \\ & + \frac{\epsilon_0(\epsilon_r - 1)}{4\pi} \int_{V'} \frac{1}{R} \cdot \frac{\partial^2 \mathbf{E}(\mathbf{r}', t')}{\partial t^2} dV' + \nabla \phi \end{aligned} \quad (3.74)$$

with

$$\nabla \phi = \frac{\nabla}{4\pi\epsilon_0} \int_{V'} \frac{1}{R} \cdot q(\mathbf{r}', t_d) dV' \quad (3.75)$$

The third term in the right hand side of (3.74) vanishes for ideal conductors ( $\epsilon_r = 1$ ), thus permitting the separation of the ideal conductor and ideal dielectric properties.

The term on the left hand side of (3.74) can be represented as a part of a voltage source,  $V_{ij}$  which is affected from an external field and/or an excited source. The first term on the right hand side is represented as a resistor  $R_{ij}$ , the second term on the right hand side is represented as an inductor  $L_{ij}$  and a part of  $V_{ij}$  affected by magnetic coupling from other elements, the third term on the right hand side is represented as a capacitor  $C_{mij}$  affecting from dielectric material, and the last term on the right hand side in (3.74) is represented a voltage drop along the current cell and can be interpreted as a capacitor  $C_{ij}$  and dependent current sources  $I_i$  and  $I_j$  affected by electric coupling from self and other elements through the continuity equation. The equivalent circuit from the interpretation is illustrated in Figure 3.5.

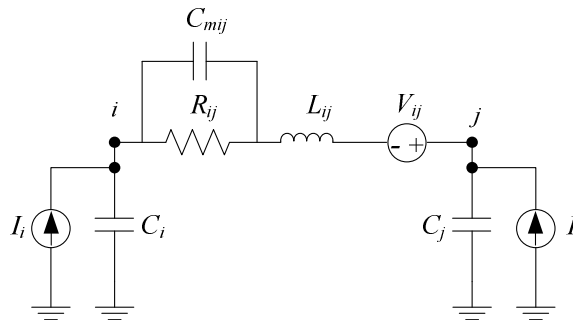


**Figure 3.5: Equivalent circuit model of a PEEC cell**



Applying Kirchhoff's voltage law to all current cells and applying the continuity equation to all potential cells, the formulation of the modified nodal analysis (MNA) is composed. The resulting of the MNA formulation in a matrix form can be solved by an appropriate network simulator in both time and frequency domains.

Like the MoM, the electromagnetic field can be calculated by post-processing of current and potentials. The post processing for electromagnetic fields calculation is describe in section 3.6.

Like other IE techniques, spurious resonances may occur [110],[111], most likely resulting from poor geometric meshing in both time and frequency domains of the PEEC method. One of reasons of instabilities and the mitigations of instabilities are described in [110].

## 4 SPECIFIC CHARACTERISTICS OF VARIOUS METHODS

In general, a calculated result by a numerical electromagnetic analysis method is heavily dependent on the cell size and the time step in the calculation. Also, absorbing boundary condition affects the result significantly. Computer resource (CPU time and memory) required by the method is very large. It is not easy to interpret the result from physical viewpoint.

### 4.1 Absorbing boundary conditions of Finite Difference Time Domain (FDTD)

In EMI/EMC simulations using the FDTD method very large computer resources, such as CPU time and memory, are required, especially involving open region problems. This problem can be overcome by truncating problem space using absorbing boundary conditions (ABC), such as Mur's ABC, Liao's ABC, a perfect matching layer.

There are two types of ABC, one is a differential-based ABC and the other is a material-based ABC. Mur's, Higdon's, and Liao's ABC are classified in a differential-based ABC on which outgoing travelling waves may not ideally be reflected because a radiation condition (RC), such as the Sommerfeld RC, is assumed. On the other hand, a perfect matched layer (PLM) is classified a material-based ABC and it literally absorbs outgoing waves at most outer boundary of the problem space.

Table 4.1 shows main features of typical ABCs.

Type of ABC	Designer	Advantage / Drawbacks	Remarks
<b>Differential-based ABC</b>	Mur [112]	- accuracy: fair - implementation in software: easy	- most popular
	Higdon [113]	- accuracy: good - implementation in software: easy	-popular
	Liao [114]	- accuracy: good - implementation in software: easy	- very popular
<b>Material-based ABC</b>	Berenger [115]	- accuracy: excellent - implementation in software: somewhat time-consuming job more than differential-based ABC	- perfect matched layer (PLM) - popular
	Sacks [116]	- accuracy: excellent	- PLM employing uniaxial anisotropic material
	Gedney [117]	- applicable to scattering fields	- easy to understand physical meaning

Table no. 4.1: Main feature of ABC

The differential-based ABC is often designated as “Outer Radiation Boundary Condition (ORBC)” or “Radiation Boundary Condition (RBC)”. The basis of this type of ABC involves assuming that a locally plane wave is propagating out of problem space, and estimating the fields for the outgoing travelling plane wave on the boundary by using fields just within the boundary.

Liao’s ABC is very popular and its accuracy is good, furthermore, its implementation in software is easy. Considering a travelling wave propagating in the direction of minus x-axis as shown in Figure 4.1, for example, the field  $E_z$  on the most outer boundary is forcibly replaced by the surrounding and past  $E_z$  as Eq.(4.1) [118] that is the second order Liao’s ABC.

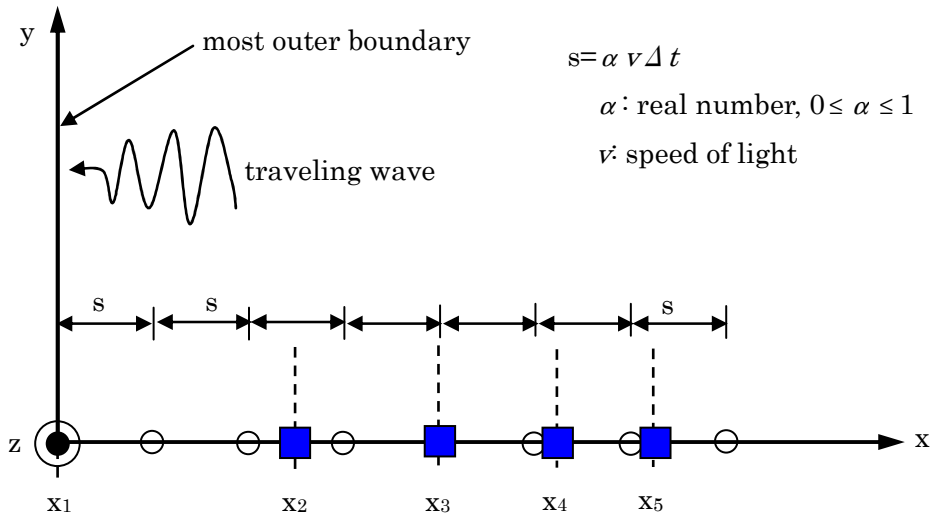


**Figure 4.1: Most outer boundary is present at  $x=x_1$ . Traveling wave propagates in the direction of minus x-axis. The  $x_2$ ,  $x_3$ ,  $x_4$ , and  $x_5$  denote the positions on the non-uniform x-axis at which fields are given by ordinary FDTD scheme**

$$\begin{aligned}
 E_z(x_1, t + \Delta t) = & 2T_{11}(x_1, s) E_z(x_1, t) \\
 & + 2T_{12}(x_1, s) E_z(x_2, t) \\
 & + 2T_{13}(x_1, s) E_z(x_3, t) \\
 & - T_{11}(x_1, s) T_{11}(x_1, s) E_z(x_1, t - \Delta t) \\
 & - \{T_{11}(x_1, s) T_{12}(x_1, s) + T_{12}(x_1, s) T_{22}(x_2, s)\} E_z(x_2, t - \Delta t) \\
 & - \{T_{11}(x_1, s) T_{13}(x_1, s) + T_{12}(x_1, s) T_{23}(x_2, s) \\
 & \quad + T_{13}(x_1, s) T_{33}(x_3, s)\} E_z(x_3, t - \Delta t) \\
 & - \{T_{12}(x_1, s) T_{24}(x_2, s) + T_{13}(x_1, s) T_{34}(x_3, s)\} E_z(x_4, t - \Delta t) \\
 & - T_{13}(x_1, s) T_{35}(x_3, s) E_z(x_5, t - \Delta t)
 \end{aligned} \tag{4.1.1}$$

$$T_{11}(x_1, s) = \frac{(s + x_1 - x_2)(s + x_1 - x_3)}{(x_1 - x_2)(x_1 - x_3)},$$

$$T_{12}(x_1, s) = \frac{s(s + x_1 - x_3)}{(x_1 - x_2)(x_2 - x_3)}, \tag{4.1.2}$$

$$T_{13}(x_1, s) = \frac{s(s + x_1 - x_2)}{(x_1 - x_3)(x_2 - x_3)},$$

$$T_{22}(x_2, s) = \frac{(s + x_2 - x_3)(s + x_2 - x_4)}{(x_2 - x_3)(x_2 - x_4)},$$

$$T_{23}(x_2, s) = -\frac{s(s + x_2 - x_4)}{(x_2 - x_3)(x_3 - x_4)}, \quad (4.1.3)$$

$$T_{24}(x_2, s) = \frac{s(s + x_2 - x_3)}{(x_2 - x_4)(x_3 - x_4)},$$

$$T_{33}(x_3, s) = \frac{(s + x_3 - x_4)(s + x_3 - x_5)}{(x_3 - x_4)(x_3 - x_5)},$$

$$T_{34}(x_3, s) = -\frac{s(s + x_3 - x_5)}{(x_3 - x_4)(x_4 - x_5)}, \quad (4.1.4)$$

$$T_{35}(x_3, s) = \frac{s(s + x_3 - x_4)}{(x_3 - x_5)(x_4 - x_5)}.$$

The  $s$  in the above equations is determined by  $\alpha v \Delta t$ , where  $\alpha$  is real number ( $0 \leq \alpha \leq 1$ ) and  $v$  is the speed of light. One of main features of Liao's formulation is that only  $E_z$ 's on the  $x$ -axis are required.

Considering uniform spatial interval  $\Delta x$  in the direction of  $x$ -axis, and substituting  $x_2 = x_1 + \Delta x$ ,  $x_3 = x_1 + 2\Delta x$ ,  $x_4 = x_1 + 3\Delta x$ , and  $x_5 = x_1 + 4\Delta x$  to Eq. (4.1) yields

$$\begin{aligned} E_z(x_1, t + \Delta t) = & 2T_{11} E_z(x_1, t) + 2T_{12} E_z(x_2, t) + 2T_{13} E_z(x_3, t) \\ & - (T_{11})^2 E_z(x_1, t - \Delta t) - 2T_{11}T_{12} E_z(x_2, t - \Delta t) \\ & - \{(T_{12})^2 + 2T_{11}T_{13}\} E_z(x_3, t - \Delta t) \\ & - 2T_{12}T_{13} E_z(x_4, t - \Delta t) - (T_{13})^2 E_z(x_5, t - \Delta t). \end{aligned} \quad (4.2)$$

Eq. (4.2) is the familiar second order Liao's ABC in case the spatial interval is uniform.

## 4.2 Method of Moments (MoM)

To use MoM, the Green functions generated by current elements immersed in a half-space conducting medium should be used. According to the direction of the current, there are two kinds of basic currents: vertical current and horizontal current. Currents in other directions can be decomposed into these two directions. In the coordinate system as shown in Figure 4.2, the vector potential caused by vertical current has only vertical component in either region I or region II.

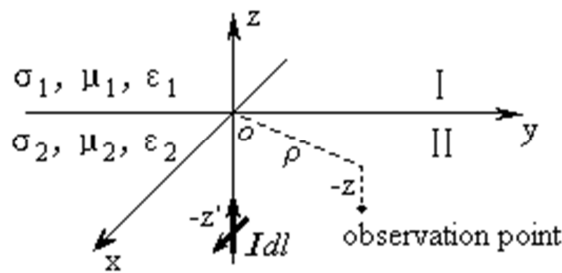


Figure 4.2: Coordinate system for deducing the Green functions.

$$\mathbf{A}_1 = \mathbf{k} \frac{\mu_1 Idl}{2\pi} \int_0^\infty \lambda Ge^{-u_2 z' - u_1 z} J_0(\lambda \rho) d\lambda \quad (4.2.1)$$

$$\mathbf{A}_2 = \mathbf{k} \frac{\mu_2 Idl}{4\pi} \left[ \left( \frac{e^{-jk_2 r}}{r} - \frac{e^{-jk_2 r'}}{r'} \right) + 2 \int_0^\infty \lambda G e^{-u_2(z+z')} J_0(\lambda \rho) d\lambda \right] \quad (4.2.2)$$

where  $\mathbf{A}_1$  and  $\mathbf{A}_2$  are the vector potentials in region I and region II,  $J_0(\lambda \rho)$  is the zero order Bessel function,

$$u_1 = \sqrt{\lambda^2 - k_1^2}, u_2 = \sqrt{\lambda^2 - k_2^2}, r' = \sqrt{\rho^2 + (z+z')^2}, r = \sqrt{\rho^2 + (z-z')^2}, k_1^2 = \omega \mu_1 (\omega \epsilon_1 - j \sigma_1),$$

$$k_2^2 = \omega \mu_2 (\omega \epsilon_2 - j \sigma_2), G = \frac{\mu_2 k_1^2}{\mu_1 k_2^2 u_1 + \mu_2 k_1^2 u_2}.$$

Yet the vector potential caused by horizontal current has not only horizontal component but also vertical component. For example, if the current is in the x direction, the vector potential will be composed of:

The horizontal component:

$$A_{1x} = \frac{\mu_1 Idl}{2\pi} \int_0^\infty \frac{\lambda \mu_2}{\mu_1 u_2 - \mu_2 u_1} e^{-u_2 z' - u_1 z} J_0(\lambda \rho) d\lambda \quad (4.2.3)$$

$$A_{2x} = \frac{\mu_2 Idl}{4\pi} \left[ \left( \frac{e^{-jk_2 r}}{r} - \frac{e^{-jk_2 r'}}{r'} \right) + 2 \int_0^\infty \frac{\lambda \mu_1}{\mu_1 u_2 - \mu_2 u_1} e^{-u_2(z+z')} J_0(\lambda \rho) d\lambda \right] \quad (4.2.4)$$

The vertical component:

$$A_{1z} = \frac{\mu_1 Idl}{2\pi} \int_0^\infty H e^{-u_2 z' - u_1 z} J_1(\lambda \rho) d\lambda \quad (4.2.5)$$

$$A_{2z} = \frac{\mu_2 Idl}{2\pi} \int_0^\infty H e^{-u_2(z+z')} J_1(\lambda \rho) d\lambda \quad (4.2.6)$$

where,  $H = \frac{\mu_1 \mu_2 (k_1^2 - k_2^2) \lambda^2}{(\mu_1 u_2 - \mu_2 u_1)(\mu_1 k_2^2 u_1 + \mu_2 k_1^2 u_2)}$ ,  $J_1(\lambda \rho)$  is the first order Bessel function of the first kind.

Equations (4.2.1) to (4.2.6) are all called generalized Sommerfeld integrals (GSI) [119].

Several approaches have been developed to get approximate solutions of GSI. The popular one is the generalized pencil-of-function (GPOF) method.

In homogeneous medium, following identical equation holds:

$$\frac{e^{-jkr}}{r} = \int_0^\infty \frac{\lambda}{u} e^{-u|z-z'|} J_0(\lambda \rho) d\lambda \quad (4.2.7)$$

where,  $k^2 = \omega \mu (\omega \epsilon - j \sigma)$ ,  $u = \sqrt{\lambda^2 - k^2}$ .

If the current is in the x direction, let's find the partial differential result of (4.2.7) and the following expression can be obtained with the help of equation  $\frac{\partial J_0(\lambda \rho)}{\partial x} = -\lambda J_1(\lambda \rho)$ :

$$-\left(\frac{1}{r} + jk\right) \frac{x e^{-jkr}}{r^2} = \int_0^\infty -\frac{\lambda^2}{u} e^{-u|z-z'|} J_1(\lambda \rho) d\lambda \quad (4.2.8)$$

By comparing GSI with (4.2.7) and (4.2.8), it can be seen that if the kernel of the GSI can be approximated by a sum of complex exponentials, GSI can be approximated by a sum of expressions just like the left side in (4.2.7) or (4.2.8). The Prony method is often used to approximate the kernel [120]. Now, GPOF method is a more popular method that has advantages over the Prony method in both computation and noise sensitivity [121-123].

Usually generalized pencil-of-function (GPOF) method [122] is used to extract features of functions in target identification. Now, it is introduced to calculate the GSI. It can approximate declining functions by a sum of complex exponentials series as following:

$$f(u) = \sum_{i=1}^M b_i e^{a_i u} \quad (4.2.9)$$

where  $a_i$  and  $b_i$  are complex values.

First, GPOF method solves a generalized eigenvalue problem to get  $a_i$  by singular value decomposition (SVD).

Then,  $b_i$  can be obtained by solving a linear least squares problem. With the sum of complex exponentials, GSI can be approximated into a sum of simple expressions. For example, by using GPOF method with (4.2.7), (4.2.1) can be approximated into the following expression:

$$\begin{aligned} \mathbf{A}_1 &= \frac{\mu_1 I dl}{2\pi} \int_0^\infty \lambda G e^{-u_2 z' - u_1 z} J_0(\lambda \rho) d\lambda \mathbf{k} \\ &= \frac{\mu_1 I dl}{4\pi} \sum_{i=1}^M b_i \frac{e^{-jk_i r_i}}{r_i} \mathbf{k} \end{aligned} \quad (4.2.10)$$

where  $r_i = \sqrt{\rho^2 + (z - a_i)^2}$ .

By using the same method, (4.2.2) to (4.2.6) can also be approximated.

After obtaining the vector potential  $\mathbf{A}$ , the electromagnetic field can be calculated from the following formulas:

$$\mathbf{E} = -j\omega\mathbf{A} - \nabla\phi = -j\omega[\mathbf{A} + \frac{1}{k^2}\nabla(\nabla \cdot \mathbf{A})] \quad (4.2.11)$$

$$\mathbf{B} = \nabla \times \mathbf{A} \quad (4.2.12)$$

where  $\phi$  is the scalar potential which can be obtained from  $\mathbf{A}$  according to the Lorentz condition. It can be seen that the electromagnetic field can also be calculated easily from the approximated vector potential  $\mathbf{A}$ .

### 4.3 Partial Element Equivalent Circuit (PEEC)

Procedures for obtaining solution of the PEEC method start from discretizing geometry structure into small cells or elements which are composed of current cells and charge or potential cells. The current cells and potential cells are interleaved each other. The rectangular pulse is employed both charge and current basis functions. Then, Galerkin's method is applied to enforce the mixed potential integral equation which is interpreted as Kirchhoff's voltage law applied to a current cell, and the continuity equation or the charge conservation equation is applied via Kirchhoff's current law to a potential cell. Whole system equations in the frequency domain can be written in a matrix form corresponding to a modified nodal analysis (MNA) formulation as shown in eq. (4.3.1).

$$\begin{bmatrix} j\omega\mathbf{P}^{-1} + \mathbf{Y}_a & \mathbf{A}^T \\ -\mathbf{A} & \mathbf{R} + j\omega\mathbf{L} \end{bmatrix} \begin{bmatrix} \Phi \\ \mathbf{I} \end{bmatrix} = \begin{bmatrix} \mathbf{I}_s \\ \mathbf{U}_s \end{bmatrix} \quad (4.3.1)$$

where  $\mathbf{A}$  is an incident matrix which expresses the cell connectivity,  $\mathbf{R}$  is a matrix of series resistances of current cells,  $\mathbf{L}$  is a matrix of partial inductances of current cells including the retardation effect,  $\mathbf{P}$  is a matrix of partial potential coefficients of potential cells including the retardation effect,  $\Phi$  is a vector of potentials on potential cells,  $\mathbf{I}$  is a vector of currents along current cells,  $\mathbf{U}_s$  is a vector of voltage sources,  $\mathbf{I}_s$  is a vector of external current sources, and  $\mathbf{Y}_a$  is an additional admittance matrix of linear and non-linear elements.

The equivalent circuit is extracted from three-dimensional geometries of a considered structure. An appropriate solver is employed to obtain solution either in the time domain or in the frequency domain. Figure 4.3 shows the procedures of the PEEC simulation. The detail of derivation and formulation of a PEEC for a thin wire structure is found in [124-127].

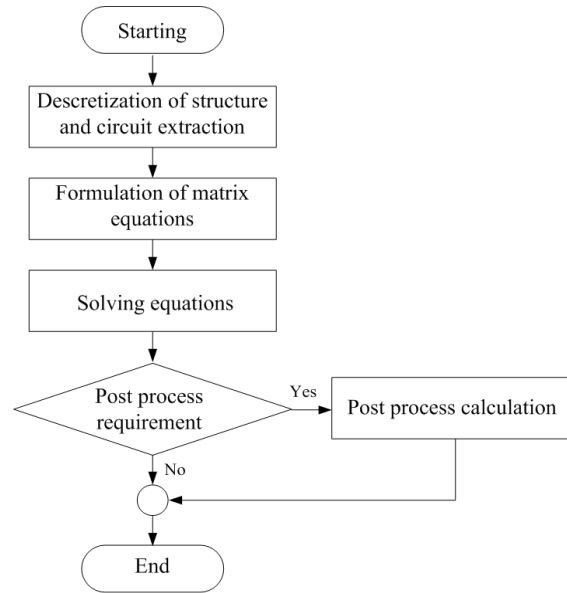


**Figure 4.3: Procedures in the simulation of PEEC models.**

In [124-127], Yutthagowith et al. have developed a full-wave PEEC method based on the thin wire structure in the frequency domain which has been successfully applied to lightning studies. The calculated results by the full-wave PEEC method have shown good agreement in comparison with the results calculated by the MoM and the FDTD methods, as well as with measured results. Moreover, in some specific cases, the computational efficiency of the method was found to be higher than those of the MoM and the FDTD method, because post processing for calculating voltages and currents in a given system is not required. Moreover, the PEEC method can readily incorporate electrical components based on a circuit theory, such as resistive, inductive, and capacitive elements, transmission lines, cables, transformers, switches, and so on.

In this section, an effective way to increase the efficiency of the PEEC method in terms of computation time, which consists of the appropriate combination of the PEEC method and the transmission line theory, is presented.

#### 4.3.1 Formulation of the quasi-static PEEC method in the time domain

The formulation of the quasi-static PEEC method in the time domain can be derived by using (4.3.1) and is given in eq. (4.3.2).

$$\begin{bmatrix} \mathbf{P}^{-1} \frac{d}{dt} + \mathbf{Y}_a & \mathbf{A}^T \\ -\mathbf{A} & \mathbf{R} + \mathbf{L} \frac{d}{dt} \end{bmatrix} \begin{bmatrix} \Phi \\ \mathbf{I} \end{bmatrix} = \begin{bmatrix} \mathbf{I}_s \\ \mathbf{U}_s \end{bmatrix} \quad (4.3.2)$$

where  $\mathbf{L}$  is a matrix of partial inductances of current cells neglecting the retardation effect, and  $\mathbf{P}$  is a matrix of partial potential coefficients of potential cells neglecting the retardation effect.

The matrices,  $\mathbf{P}$  and  $\mathbf{L}$ , express electromagnetic coupling among the cells, and are dense. The solution of eq. (4.3.2) based on quasi-static assumption can be obtained by employing an appropriate integration scheme. For simplicity, Backward Euler scheme is applied to eq. (4.3.2) by discretizing in time. The following equation is obtained.

$$\begin{bmatrix} \frac{1}{\Delta t} \mathbf{P}^{-1} + \mathbf{Y}_a & \mathbf{A}^T \\ -\mathbf{A} & \mathbf{R} + \frac{1}{\Delta t} \mathbf{L} \end{bmatrix} \begin{bmatrix} \Phi^n \\ \mathbf{I}^n \end{bmatrix} = \begin{bmatrix} \mathbf{I}_s^{n-1} + \mathbf{P}^{-1} \frac{1}{\Delta t} \Phi^{n-1} \\ \mathbf{U}_s^{n-1} - \mathbf{L} \frac{1}{\Delta t} \mathbf{I}^{n-1} \end{bmatrix} \quad (4.3.3)$$

In [127], it has been clear that the electromagnetic retardation can be neglected in most cases of tower surge analyses so that computation time is greatly reduced in a numerical simulation.

#### 4.3.2 Transmission Line Model (TLM)

Formulation of a multi-transmission line in the frequency domain as multi-port network as illustrated in Figure 4.4. The voltages and currents at sending and receiving ends of the transmission line are expressed in eqs. (4.3.4) to (4.3.6);

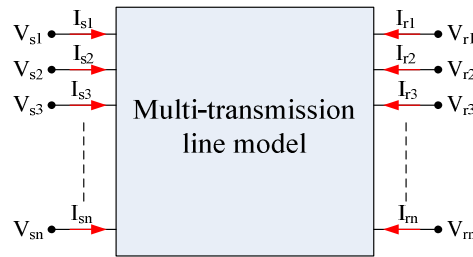


Figure 4.4: Multi-transmission line as multi-port network

$$\begin{bmatrix} \mathbf{V}_s \\ \mathbf{V}_r \end{bmatrix} = \begin{bmatrix} \coth(\Gamma) \mathbf{Z}_c & \operatorname{cosech}(\Gamma) \\ \operatorname{cosech}(\Gamma) & \coth(\Gamma) \mathbf{Z}_c \end{bmatrix} \cdot \begin{bmatrix} \mathbf{I}_s \\ \mathbf{I}_r \end{bmatrix}, \quad (4.3.4)$$

$$\Gamma^2 = \mathbf{Z}\mathbf{Y} \quad (4.3.5)$$

$$\mathbf{Z}_c = \Gamma^{-1} \mathbf{Z} \quad (4.3.6)$$

where  $\mathbf{V}_s$ ,  $\mathbf{V}_r$ ,  $\mathbf{I}_s$ , and  $\mathbf{I}_r$  are vectors of voltages and currents at sending ends and receiving ends, respectively.  $\Gamma$ ,  $\mathbf{Z}$ ,  $\mathbf{Y}$ , and  $\mathbf{Z}_c$  are a propagation matrix, a series impedance matrix per unit length, a shunt admittance matrix per unit length, and a characteristic impedance, respectively.

Eq. (4.3.4) can be written in a compact form as the following.

$$\Phi_T = \mathbf{Z}_a \mathbf{I}_T$$

or 
$$\mathbf{I}_T = \mathbf{Y}_a \Phi_T \quad (4.3.7)$$

where  $\Phi_T$  and  $\mathbf{I}_T$  are vectors of voltages and currents at sending ends and receiving ends, respectively.  $\mathbf{Z}_a$  and  $\mathbf{Y}_a$  are an impedance matrix and an admittance matrix, respectively.

From (4.3.4) to (4.3.7), the formulation in the time domain can be written in the matrix form with propagation time ( $t_d$ ) as the following;

$$\begin{aligned} \mathbf{V}_s(t) - \mathbf{Z}_c \mathbf{I}_s(t) &= \mathbf{V}_r(t-t_d) + \mathbf{Z}_c \mathbf{I}_r(t-t_d), \\ \mathbf{V}_r(t) - \mathbf{Z}_c \mathbf{I}_r(t) &= \mathbf{V}_s(t-t_d) + \mathbf{Z}_c \mathbf{I}_s(t-t_d), \end{aligned} \quad (4.3.8)$$

or it can be written in another form as the following;

$$\begin{aligned} \mathbf{I}_s(t) - \mathbf{Y}_c \mathbf{V}_s(t) &= -\mathbf{Y}_c \mathbf{V}_r(t-t_d) - \mathbf{I}_r(t-t_d), \\ \mathbf{I}_r(t) - \mathbf{Y}_c \mathbf{V}_r(t) &= -\mathbf{Y}_c \mathbf{V}_s(t-t_d) - \mathbf{I}_s(t-t_d), \end{aligned} \quad (4.3.9)$$

where  $\mathbf{Y}_c$  is an inversion matrix of  $\mathbf{Z}_c$ . To consider the frequency dependence of  $\mathbf{Z}$  and  $\mathbf{Y}$ , the time convolution is required.

In the frequency domain, the transmission line model can be combined with the PEEC method by adding the admittance matrix ( $\mathbf{Y}_a$ ) in (4.3.7) to the additional admittance matrix in (4.3.2). The transmission line model can also be combined with the PEEC method by adding  $\mathbf{Y}_c$  as an additional admittance matrix on the matrix on the left hand side of (4.3.3) and adding additional delayed current sources in (4.3.9) on the right hand side of (4.3.3).

#### 4.4 On the representation of metallic conductors

Thin wire approximation problems related to the infinite conductivity of structures.

In [128] and [129], Wang et al. developed a modified-mesh-current (MMC) method, this method can be viewed as a combination of the PEEC method and the integral equation method (or MoM method). The MMC method mainly has three attractive features:

1) it is accurate from DC to 1 MHz and it does not have the low-frequency breakdown problem. In comparison, the conventional electric-field integral-equation (EFIE)-MoM method only uses tangential current along the thin-wire as unknowns; it is always plagued by the low-frequency breakdown problem when part of the thin-wire structure is exposed in the air.

The reason of this phenomenon is that the EFIE method only uses tangential (axial) current as unknown. The charge density  $\rho$  is approximated from the divergence of the current:  $\rho = -\nabla \cdot \mathbf{J}/s$ . When the frequency is very low, the current's contribution to the electric field ( $s\mathbf{A}$ , which is proportional to the frequency and is the spatial integration of the axial current.) becomes very insignificant in comparison to the charge's contribution ( $\nabla \phi$ , which is inversely proportional to the frequency and is the spatial integration of the divergence of axial current.). Consequently, the solution of the final linear equations is prone to produce an axial-current distribution whose divergence is accurate. The axial-current distribution itself might not be accurate. The MMC method can be viewed a PEEC representation of the mixed-potential integral-equation (MPIE) [130]. Similar to the MPIE formulation, the proposed method uses both charges and current as the state-variables in order to disentangle each's contribution to the electric field. Although the number of unknowns is nearly doubled, the low-frequency instability is removed.

2) The method takes into account all the four coupling mechanisms among conductors, namely, inductive coupling, resistive coupling, conductive coupling, and capacitive coupling. It has a time-domain state-space form and can be easily implemented in a circuit-simulator with external components connected.

Generally speaking, for conductors embedded in lossy medium, there exist four coupling mechanisms, namely, capacitive coupling, conductive coupling, inductive coupling, and resistive coupling, as shown in Figure 4.5. The former two coupling mechanisms are related to the potential rise of one conductor caused by the current (including displacement and conductive currents) flowing radially out of another conductor. The latter two coupling mechanisms are related to the voltage drop on one conductor caused by the current flowing axially in another conductor.



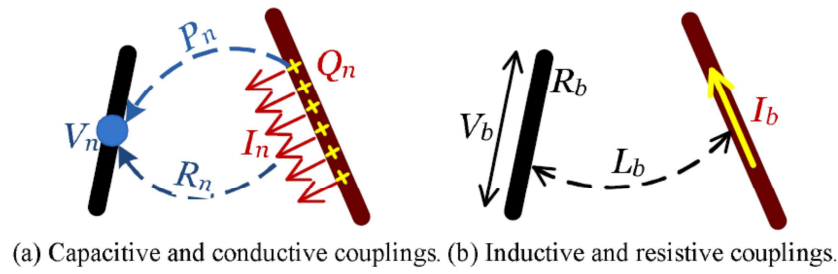


**Figure 4.5: Illustration of four coupling mechanisms in lossy medium.  $I_b$  and  $I_n$  are the axial and radial currents, respectively.  $Q_n$  is the charge accumulated on the conductor [129]**

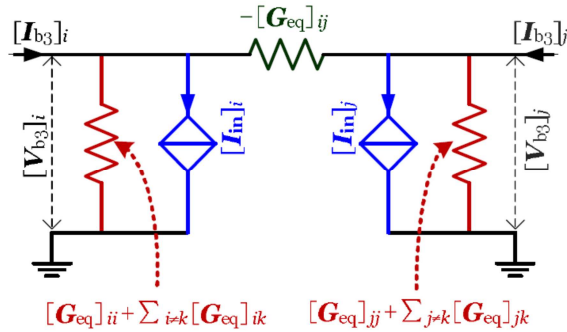


**Figure 4.6: Illustration of the active multiport network derived from the state-space system [129]**

The MMC method reduces the electric circuit in Figure 4.5 into a state-space form. Through trapezoidal rules, the state-space equation can be reduced into an active multiport network, as illustrated in Figure 4.6. The network is described by a conductance matrix  $\mathbf{G}_{eq}$  and time-dependent current sources  $I_{in}$ , which is updated using history current. The active network can be easily implemented in EMTP.

3) MMC method has a good computational efficiency. Building the active network from the thin-wire structure only requires one-time computation of the inverse of the system matrix. After obtaining the active network, only several matrix-vector multiplications are needed at every time step in the simulation. In comparison, MoM method always requires repetitive calculation of the inverse of the system matrix in many frequencies.

Another attractive feature of the new method, which is not explored yet, is that its state-space form facilitates the modeling of the nonlinear effects, such as the soil ionization and the corona discharge. For example, the soil ionization can be modeled by changing the radius of the electrode, and correspondingly, the coupling matrices at every time step. Though the consideration of these nonlinear effects seems to be straightforward, the loss of stability and passivity of the model caused by the variation of coupling matrices should be taken cared carefully.

However, because the method is based on quasi-static electromagnetic assumption (That is the retardation effect between the source and the field is neglected.), it is only suitable for thin-wire structures with relatively small spatial scales. As for lightning-caused transient, the spatial scale of the structure should be no more than a hundred meters.

#### 4.5 On the representation of soil-ionization phenomena

As already evidenced by many researches, the characteristic of grounding systems subject to high impulse current is dramatically different from that at low frequency. Because inductive behaviour can become more and more important with respect to resistive behaviour and, in addition, these large currents can generate complicated soil ionization surrounding the grounding conductors, which makes the transient characteristic typically non-linear [132-141].

When high impulse currents excite a grounding system, the transient electromagnetic fields will be generated in the soil around the grounding conductors.

$$E = J\rho \quad (4.6.1)$$

where  $E$  is the electric field strength in the soil,  $\rho$  is the soil resistivity and  $J$  is the current density in the soil.

The electric field strength in the soil will rise with the increase of the amplitude of impulse current. When the electric field strength surrounding the grounding conductor exceeds the critical value of the electrical field strength ( $E_c$ ), soil breakdown around the conductor will occur [136]. It will make the potential fall around the grounding conductor smaller. And it will convert the affected portion of the soil from a medium to a metallic conductor.

The fall of potential in the area of soil ionization is often neglected. That is to say, the resistivity of the area of soil ionization is approximately considered to be zero. The radius of the area of soil ionization surrounding the grounding electrode can be considered to be the equivalent radius of the electrode during the transient process.

The inductive effect is notable for the high frequency of impulse current. It will obstruct the current to flow towards the other end of the conductors. This will result in extremely unequal leakage current along the grounding conductors and the steel reinforcement bars of the foundation if any [137]. And the ionization degree and equivalent radii of the soil around every point of the conductors are nonuniform. The tested shape of the ionized zone around a grounding conductor is illustrated in Figure 4.7. The current density in the soil, where is much closer to the feed point, is much larger. So the ionized zone of the soil around the conductor is not columniform but pyramidal.

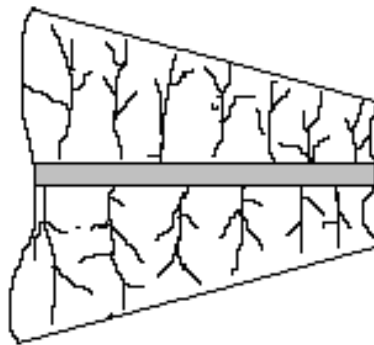


**Figure 4.7: Shape of the ionized zone around a grounding-electrode [138]**

With respect to the complexity of mathematical model, the conductor can be represented by a set of cylindrical zones as shown in Figure 4.8 [139]. Obviously, this assumption is reasonable.  $r_i$  in Figure 4.8 is the equivalent radius for the  $i$ -th segment, which is time-variable when an impulse current is injected into the grounding conductor; and  $a$  is the radius of the metal conductor.

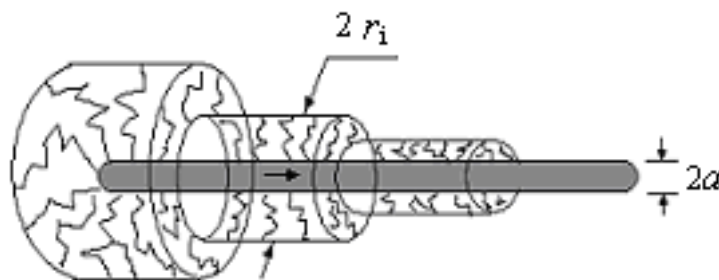


**Figure 4.8: Model of equivalent radii for each segment [139]**

The model in Figure 4.8 can be simulated by a lossy transmission line model as shown in Figure 4.9, the shunt capacitance  $C$  and shunt conductance  $G$  are related to the equivalent diameters of every conductor segment, so they are time-varying. The electric field strength on the boundary of ionized zone is the critical value of soil breakdown. The equivalent radius for each segment can be obtained by [139]

$$J_i = E_c / \rho = \Delta i_i / (2\pi a_i l_i) \quad (4.6.2)$$

where,  $J_i$  is the current density leaked by the  $i$ th segment;  $\Delta i_i$  is the current leaked into earth from the  $i$ th segment. The value used for the critical field gradient in this paper is selected as 300 kV/m. The formulas to calculate the inductance, resistance, capacitance and conductance per unit length in Figure 4.9 were derived by He, et al [139].

Dividing the grounding grid or grounding device into segments, the respective equivalent diagram between the  $i$ th and  $j$ th segments is shown in Figure 4.10 [140], the mutual inductance, mutual resistance and mutual capacitance between any two segments are considered. Assuming that the current  $i_i$  along the axis of the  $i$ th segment is uniform, then the self-inductance  $L_{ii}$  of the  $i$ th segment, and mutual inductance  $L_{ij}$  between the  $i$ th and  $j$ th segments can be calculated by

$$L_{ii} = \frac{\mu_0}{4\pi} \iint_{l_i l_i} \frac{1}{D_{ii'}} dl_i \cdot dl_{i'}, \quad L_{ij} = \frac{\mu_0}{4\pi} \iint_{l_i l_j} \frac{1}{D_{ij}} dl_i \cdot dl_j \quad (4.6.3)$$

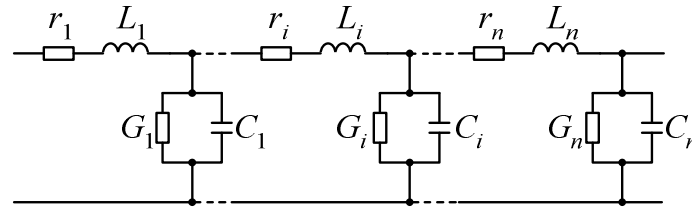


Figure 4.9: The loss transmission line model of a grounding electrode [139]

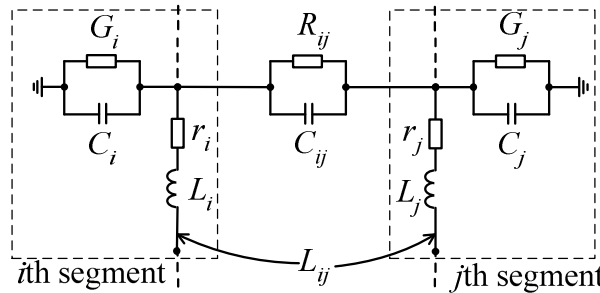


Figure 4.10: The mutual impedance diagram between two segments of a grounding grid [140]

where,  $\mu_0$  is the permeability of the soil;  $l_i$  is the path of the  $i$ -th conductor axis,  $l_i$  is a path at the surface of the  $i$ -th conductor,  $l_j$  is the path of the  $j$ -th conductor,  $D_{ij}$  is the distance between two segments  $dl_i$  and  $dl_j$  in the integral routine,  $D_{ii'}$  is the distance between  $dl_i$  and  $dl_{i'}$  in the integral routine.

The mutual impedance  $Z_{ij}$  consisting of mutual resistance  $R_{ij}$  and mutual capacitance  $C_{ij}$  between the  $i$ th and  $j$ th segments can be calculated by [141].

$$Z_{ij} = \frac{1}{4\pi l_j (\sigma + j\omega\epsilon)} \left[ \iint_{l_i, l_j} \frac{1}{D_{ij}} dl_i dl_j + \frac{\sigma + j\omega(\epsilon - \epsilon_0)}{\sigma + j\omega(\epsilon + \epsilon_0)} \iint_{l_i', l_j} \frac{1}{D_{ij'}} dl_i' dl_j \right] \quad (4.6.4)$$

where,  $\epsilon_0$  and  $\epsilon$  are permittivities of the air and the soil;  $\sigma$  is the conductivity of soil;  $D_{ij}$  is the distance between two segments  $dl_i'$  and  $dl_j$  in the integral routine,  $l_i'$  is the image length of the  $i$ -th conductor.

## 5 APPLICATION EXAMPLES

In this chapter, representative applications of numerical electromagnetic computation methods to analyse surges are reviewed. Section 5.1 shows the calculation of surge characteristics of overhead transmission-line towers by using the following methods: (i) method of moments (MoM) [142] in the time domain, (ii) finite-difference time-domain (FDTD) method [143] and PEEC. In Section 5.2, surge characteristics of a vertical grounding electrode and a horizontally-placed square-shape grounding electrode, computed using the FDTD method, are presented. In Section 5.3, the FDTD-computed surge characteristics of an air-insulated substation are shown. Section 5.4 shows lightning surge voltages induced on overhead distribution lines computed using: (i) the MoMs in frequency and time domains, (ii) FDTD method and (ii) PEEC. Section 5.4 also presents comparison between lightning-induced surges computed using transmission line theory vs 3D full-wave Finite Element Method. In Section 5.5, propagation characteristics of a power line carrier or communication (PLC) signal along a power coaxial cable, computed using the FDTD method, are presented. In Section 5.6, surge characteristics of a wind-turbine-generator tower struck by lightning and its inside transient magnetic field, computed using the FDTD method, are shown. Section 5.7 presents the simulation algorithm and numerical results of 3D full-Maxwell FEMTD simulations of very fast transients (VFTs) in gas insulated switchgears (GIS).

### 5.1 Surge characteristics of transmission towers

Mozumi et al. [144] have computed, using the MoM in the time domain [145], voltages across insulators of a 500-kV double-circuit transmission-line tower with two overhead ground wires located above perfectly conducting ground, in the case that the tower top is struck by lightning and thereby back-flashover occurs across the insulator of one phase. In order to analyze back-flashover using the MoM in the time domain, they incorporate a flashover model developed by Motoyama [146] in it. For the computations, the lightning return-stroke channel is represented by a vertical perfectly conducting wire in air. The lightning channel and the tower are excited by a lumped voltage source in series with 5 k $\Omega$  lumped resistance inserted between them. Figure 5.1 shows the structure of the tower to be analyzed. Figure 5.2 shows waveforms of insulator voltages computed using the MoM in the time domain and using the Electro-Magnetic Transients Program (EMTP) [147], when an upper-phase back-flashover occurs for a current of magnitude 150 kA and risetime 1  $\mu$ s being injected. Note that, in the EMTP computation, a multi-story transmission-line tower model [148] is employed, and its top part characteristic impedance is set to 245  $\Omega$  and its bottom part characteristic impedance is set to 180  $\Omega$ . MoM-computed waveforms are reasonably well reproduced by the corresponding EMTP-computed waveforms.

Noda [149] has computed, using the FDTD method, voltages across insulators of a 500-kV double-circuit transmission-line tower, located above ground having conductivity of 10 mS/m, in the case that the tower top is struck by lightning. In his computation, the lightning return-stroke channel is represented by a vertical perfectly conducting wire having additional distributed series inductance of 10  $\mu$ H/m, and the speed of current wave propagating along the wire is 0.33c. The lightning channel and the tower are excited by a lumped current source inserted between them. Figure 5.3 shows the structure of the tower to be analyzed using the FDTD method. Figure 5.4 shows waveforms of insulator voltages computed using the FDTD method and using the EMTP when a ramp current of magnitude 1 A and risetime 1  $\mu$ s is injected. Note that, in his EMTP computation, a new circuit model for a tower [149] is employed, and its characteristic impedance is set to 192  $\Omega$ . FDTD-computed waveforms are reasonably well reproduced by the corresponding EMTP-computed waveforms. Also note that Noda [149] has shown that his FDTD-computed waveforms of tower-top voltage and tower and ground-wire currents for a similar tower agree reasonably well with the corresponding measured waveforms.

Yutthagowith *et al.* have used the partial element equivalent circuit (PEEC) method [150] to calculate voltages across insulators of a 500-kV transmission-line tower. The computed results agree well with the corresponding

measured waveforms [148]. Figure 5.5 shows the structure of the tower to be analyzed and injected current waveforms. Figure 5.6 shows waveforms of insulator voltages computed using the PEEC method. It is noted that Visacro and Soares [151] has employed the hybrid electromagnetic/circuit model (HEM) to calculate the same case of which results also agree well with the measured waveforms.

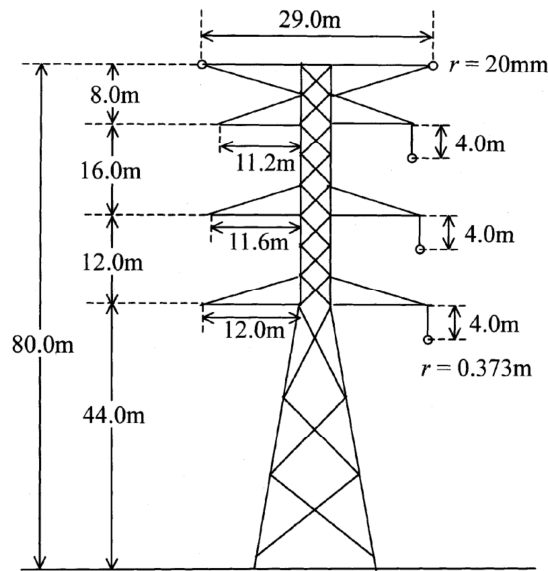


**Figure 5.1: Structure of a 500-kV transmission-line tower to be analyzed using the MoM in the time domain [144]**

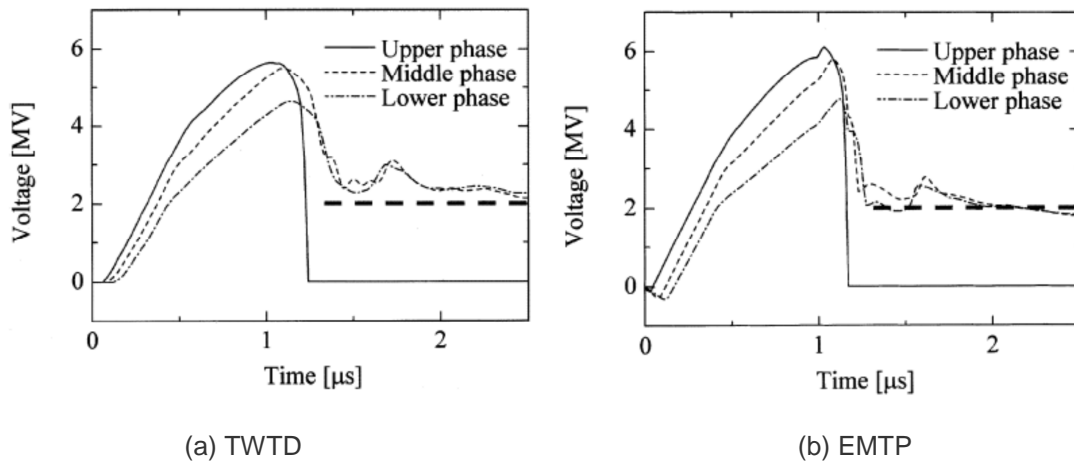


**Figure 5.2: Waveforms of insulator voltages computed using the MoM in the time domain and using EMTF, in the case of an upper-phase back-flashover for a current of magnitude 150 kA and risetime 1  $\mu$ s being injected [144]**

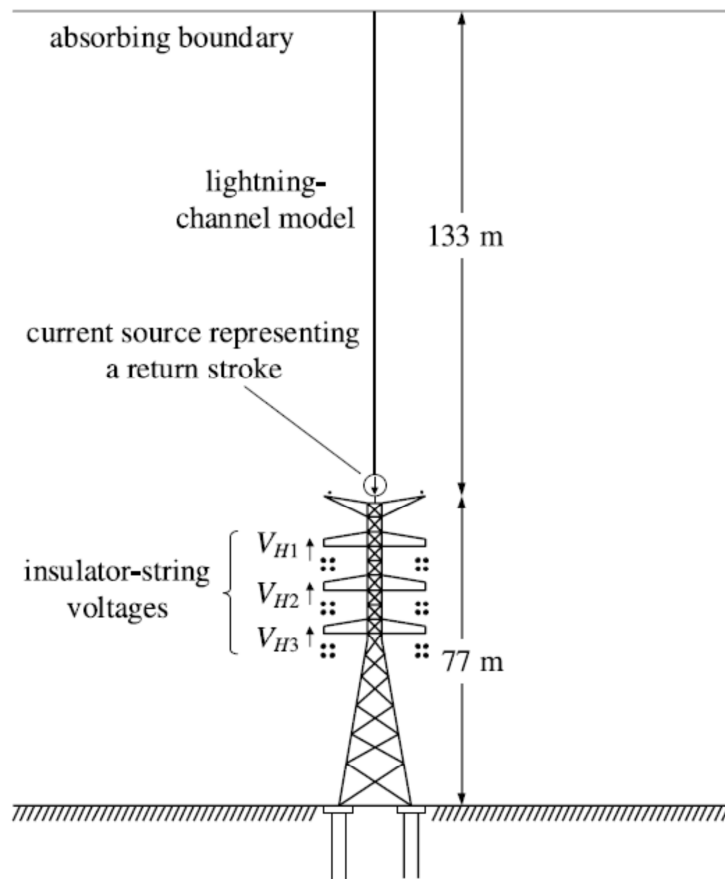


**Figure 5.3: Structure of a 500-kV transmission-line tower to be analysed using the FDTD method [149]**

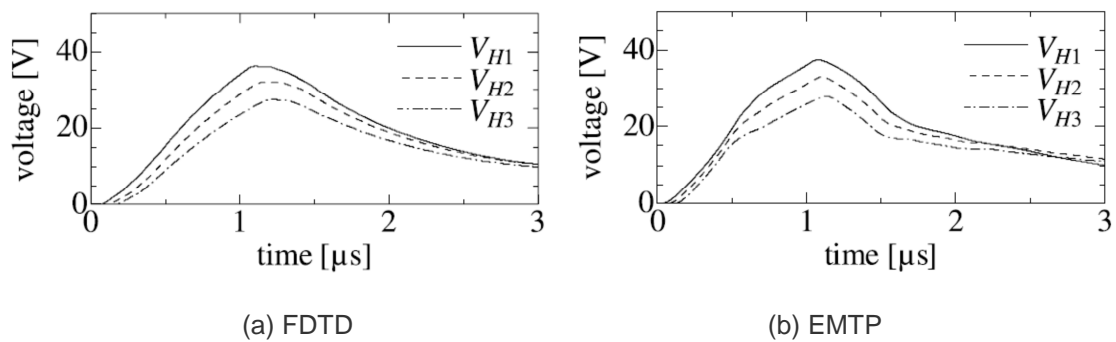


**Figure 5.4: Waveforms of insulator voltages computed using the FDTD and using EMTP, in the case of a ramp current of magnitude 1 A and risetime 1  $\mu$ s being injected [149]**

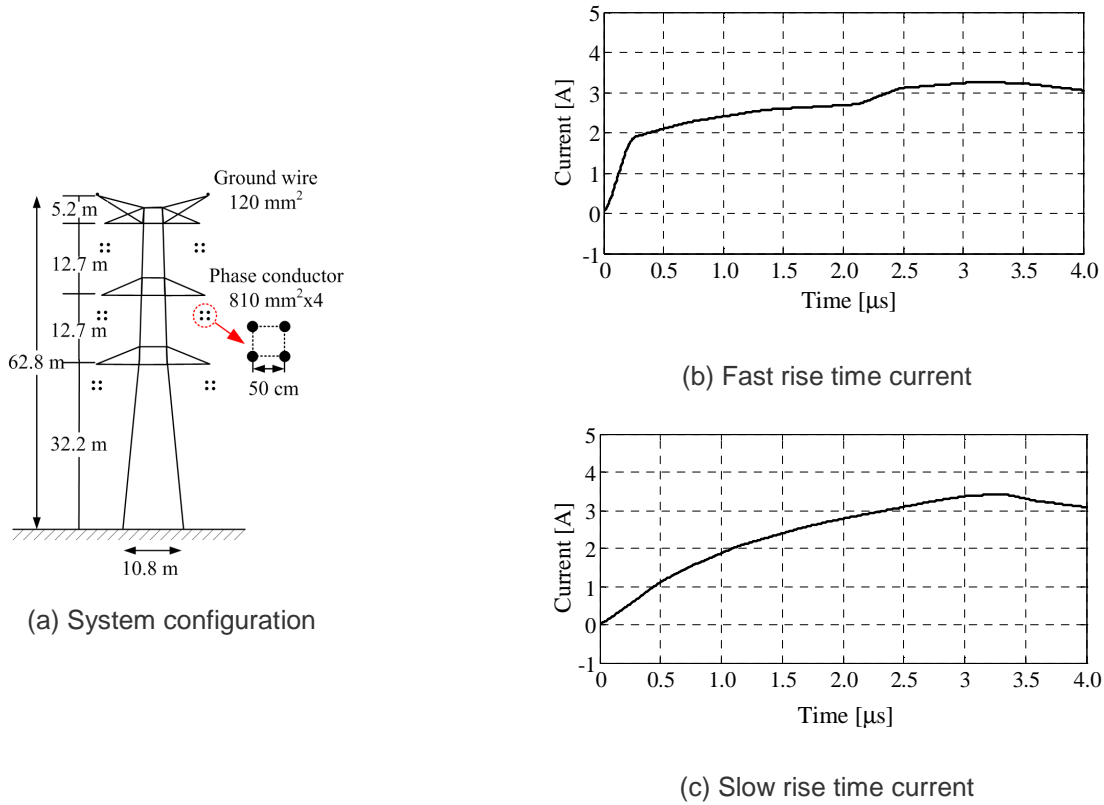


Figure 5.5: System configuration and applied current waveforms

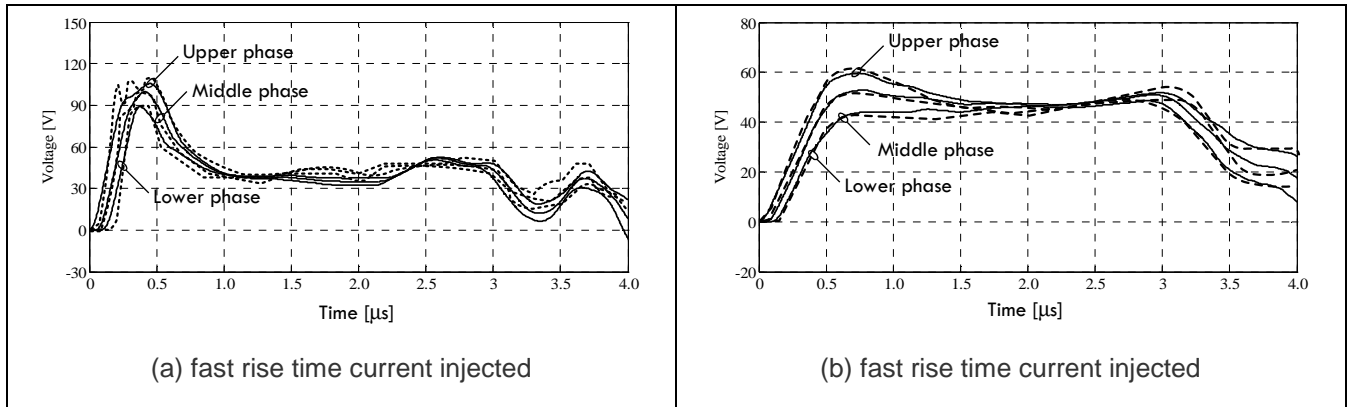


Figure 5.6: Voltage waveforms on insulators

## 5.2 Surge characteristics of grounding electrodes

### 5.2.1 Vertical grounding rods

Tanabe [152] has measured the transient response of a vertical grounding electrode of  $0.5 \text{ m} \times 0.5 \text{ m} \times 3 \text{ m}$ , shown in Figure 5.7, in order to test the validity of his FDTD computation. In the FDTD computation, the conductivity, relative permittivity and relative permeability of the ground are set to  $\sigma = 1.9$  to  $2.7 \text{ mS/m}$  (based on their low-frequency measurement),  $\epsilon_r = 50$  and  $\mu_r = 1$ , respectively. Figure 5.8 shows the FDTD-computed voltage and



current waveforms for the vertical electrode and the corresponding measured waveforms [152]. The FDTD-computed waveforms are in good agreement with the corresponding measured ones.

Tanabe et al. [153] have measured the transient response of a horizontally-placed square-shape grounding electrode of 7.5 m  $\times$  7.5 m, buried 0.5 m depth, in order to test the validity of his FDTD computation. In the FDTD computation, the conductivity, relative permittivity and relative permeability of the ground are set to  $\sigma = 3.8$  mS/m (based on their low-frequency measurement),  $\epsilon_r = 50$  and  $\mu_r = 1$ , respectively. Figure 5.9 shows the FDTD-computed voltage and current waveforms for the square-shape electrode and the corresponding measured waveforms [153]. The overall waveforms of voltage and current computed using the FDTD method agree reasonably well with the measured ones.

Note that Miyazaki and Ishii [154] have reasonably well reproduced the measured waveforms shown in Figure 5.8 using the MoM in the frequency domain. Also note that, using the FDTD method, Baba et al. [155] have reproduced responses of a 6-m long vertical grounding electrode and a 12-m long horizontal grounding electrode, computed by Grcev [156] using the MoM in the frequency domain. In [155], Baba et al. propose a method for representing a thin wire in a lossy ground.

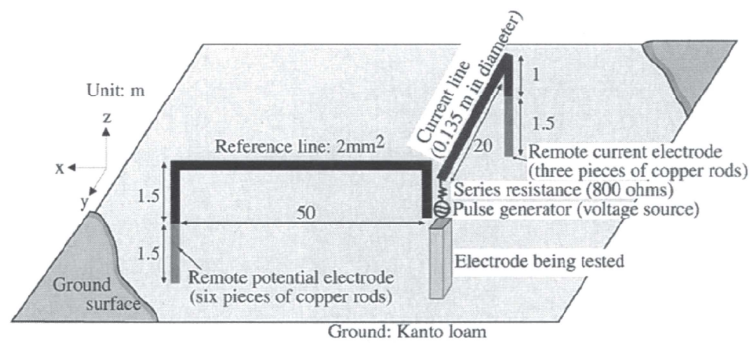


**Figure 5.7: Configuration of a 3-m long vertical grounding electrode and its auxiliary wires for measurement of its surge response [151]**

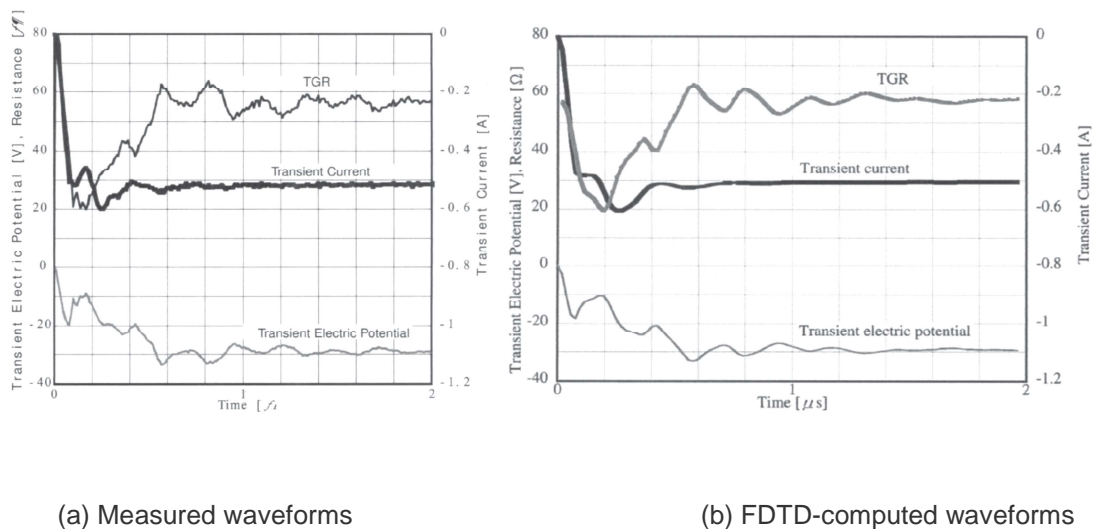


**Figure 5.8: Measured waveforms of voltage and current for the 3-m long vertical grounding electrode, and the corresponding FDTD-computed waveforms [151]**



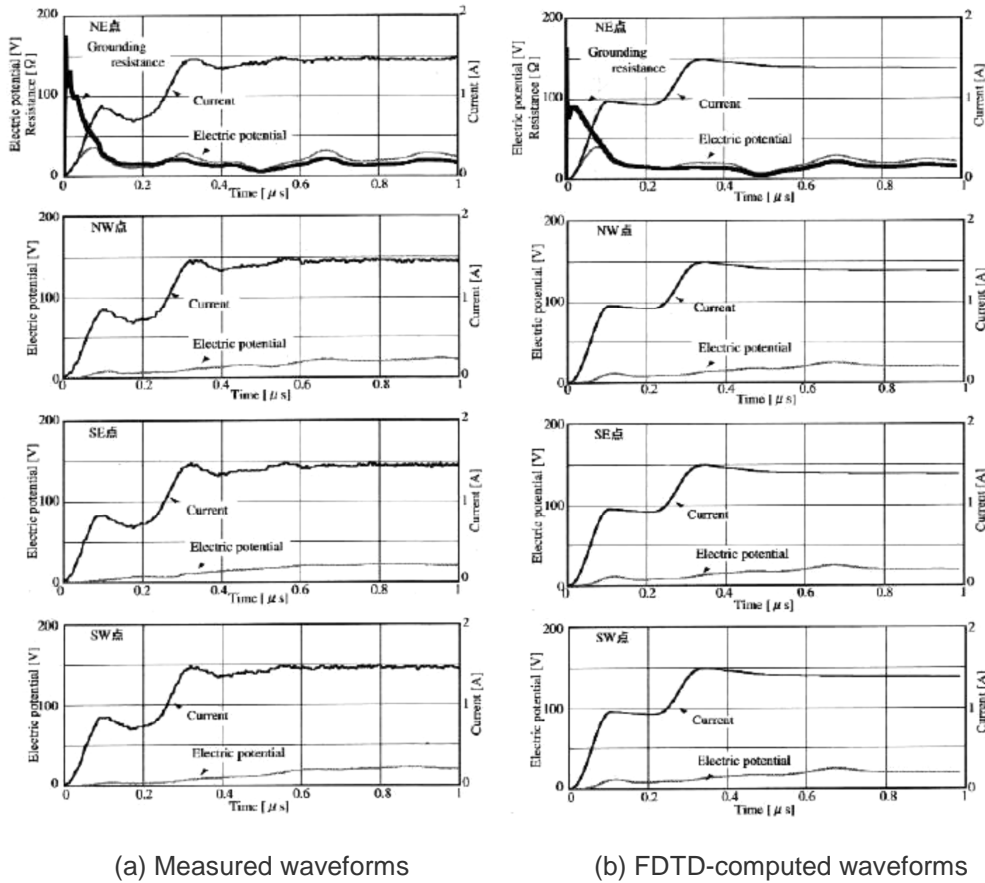


**Figure 5.9: Measured waveforms of voltage at each corner of a horizontally-placed square-shape grounding electrode of  $7.5 \text{ m} \times 7.5 \text{ m}$  and injected current, and the corresponding FDTD-computed waveforms [152]**

Ala et al. [157] have considered the soil ionization around a grounding electrode in their FDTD computations. The soil ionization is represented by reducing the local resistivity dependently on the instantaneous value of electric field there. Waveforms of voltage and current, computed using the FDTD method with this resistivity-controlled ionization model, for grounding electrodes agree well with the corresponding waveforms measured by Darveniza and Liew [158] for high current injection.

### 5.2.2 Horizontal grounding electrodes

There have been many papers on the performance of grounding systems [159-165]. As an example, a double exponential lightning current with  $2.6/50 \text{ μs}$  wave shape and 20 kA amplitude is injected into a ground electrode at one end. The grounding electrode with 20 meters length is buried at 1-meter depth under the earth. The soil is assumed to be homogeneous with a  $100 \text{ Ω} \cdot \text{m}$  resistivity, a relative permittivity of 1, and relative permeability of 1. The computation model is illustrated in Figure 5.10 [164]. When the lightning current mentioned above is injected in the grounding electrode, severe transient electric field will occur in air. When soil ionization is taken into consideration, the transient electromagnetic fields generated by lightning current will be different with those without considering soil ionization. From comparing the magnitudes of electromagnetic field at points 1, 2, and 3, we can get an idea of the influence of soil ionization on transient electromagnetic fields.

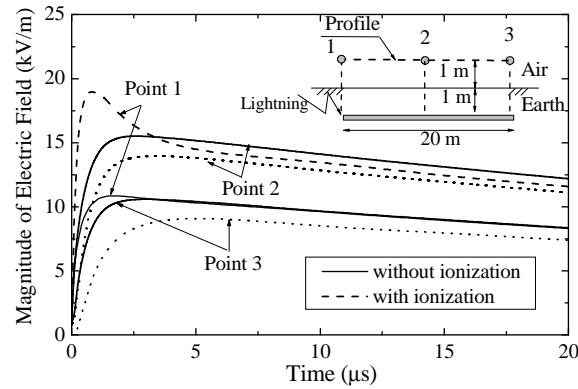


Figure 5.10: Magnitude of electric field at different points [164]

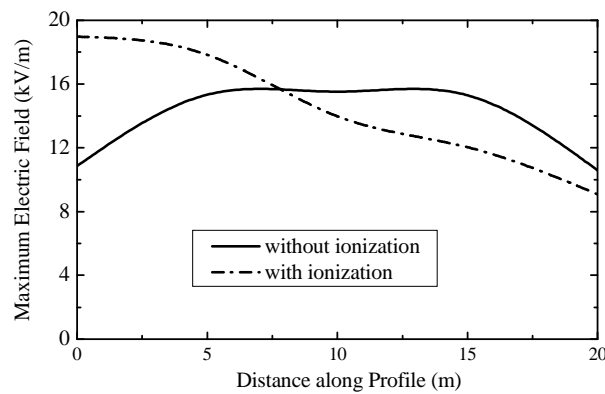


Figure 5.11: Maximum electric field along the profile [164]

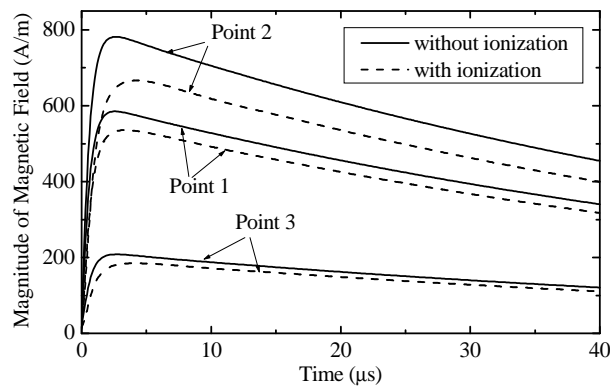
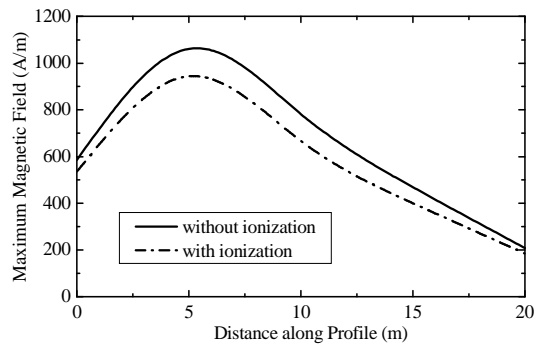


Figure 5.12: Magnitude of magnetic field at different points [164]



**Figure 5.13: Maximum magnetic field along the profile [164]**

Figure 5.11 shows the magnitudes of electric field with and without soil ionization for point 1, 2, and 3 on the profile illustrated in Figure 5.12 [164]. Figure 5.13 shows the magnitudes of magnetic field with and without soil ionization for point 1, 2, and 3 [164].

From the curves in Figure 5.10 [164], when soil ionization is taken into consideration, the electric field in point 1 becomes severer obviously. While the electric fields in point 2 and 3 become smaller. The time to peak value of the electric fields is about 1-2  $\mu\text{s}$  ahead of that of the injected lightning current. When soil ionization is taken into consideration, the magnetic fields in 3 points all become smaller, as shown in Figure 5.12.

The curves in Figure 5.11 show the maximum electric fields along the profile illustrated in Figure 5.10. From the curves in Figure 5.10, when soil ionization is taken into consideration, the maximum electric fields in air near the position of feed point become severer. On the other hand, the maximum electric fields in air far away from the feed point become smaller.

The curves in Figure 5.13 illustrate the maximum magnetic fields along the profile [164]. When the soil ionization is taken into consideration, the maximum magnetic fields along the profile become smaller. But the influence of soil ionization on magnetic fields is slight with respect to the electric fields.

### 5.2.3 Complex grounding configurations

As an application, structure shown in Figure 5.14 is analyzed in order to show the influence among the lines both in air and soil. A 30 kA 2.6/40  $\mu\text{s}$  lightning current strikes point A directly [165]. The radii of the columnar conductors are 0.01 m. The resistivity of the conductors are  $1 \times 10^{-7} \Omega \cdot \text{m}$ , and their relative magnetic permeability is 1000. The soil resistivity is 100  $\Omega \cdot \text{m}$  and its relative permittivity is 10. Figure 5.15 shows the currents flowing through point B, point C and point D[165].

It can be seen that when a 30 kA 2.6/40  $\mu\text{s}$  lightning current strikes point A directly, the currents flowing through point B, point C and point D are almost the same. The peak values of the currents are 0.2298 kA, 0.2309 kA and 0.2318 kA respectively.

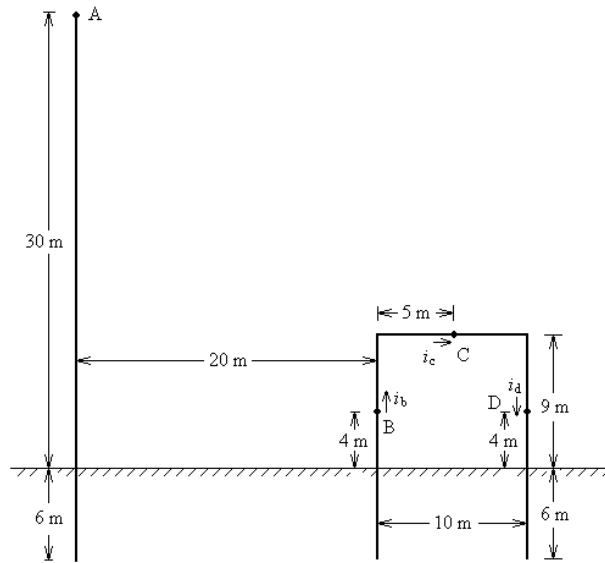


Figure 5.14: The analyzed structure [165]

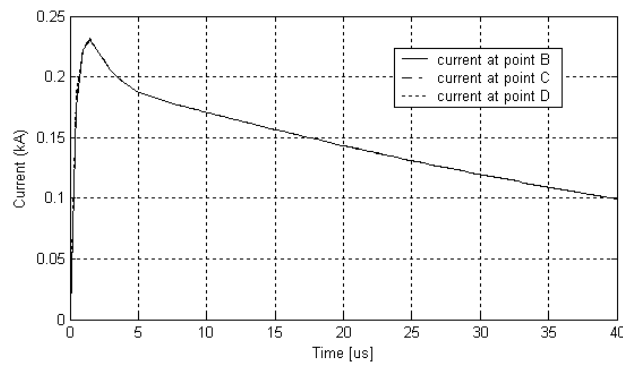


Figure 5.15: The transient current flowing through point B, point C and point D [165]

The multi-grounding systems shown in Figure 5.16 is also analyzed [165]. All the grounding systems are buried 1 m depth. The radii of the columnar conductors are 0.01 m. The resistivity of the conductors are  $1 \times 10^{-7} \Omega \cdot \text{m}$ , and their relative magnetic permeability is 1000. The soil resistivity is  $100 \Omega \cdot \text{m}$  and its relative permittivity is 10. The 30 kA 2.6/40  $\mu\text{s}$  lightning current strikes point A directly. Figure 5.17 shows the potential rise at point A, point B and point C [165].

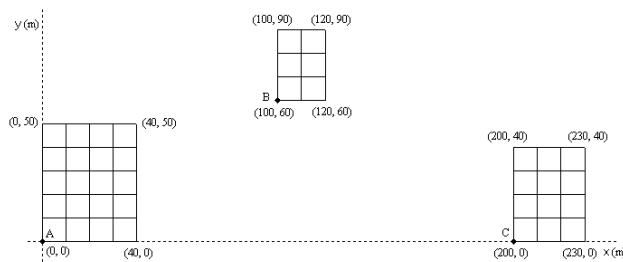
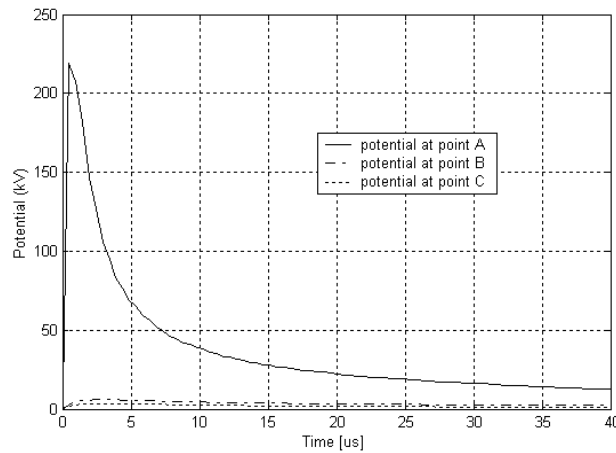
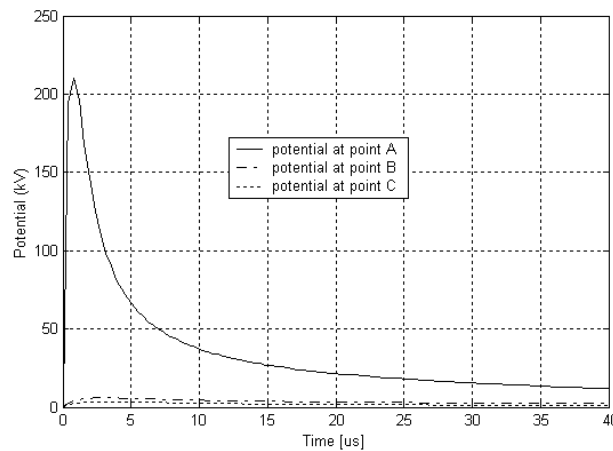


Figure 5.16: The analyzed grounding systems [165]



**Figure 5.17: The transient ground potential rise at point A, point B and point C[165]**

It can be seen that when a 30 kA 2.6/40  $\mu$ s lightning current strikes point A directly, the transient ground potential rise at point A, point B and point C are quite different. The peak values of the potential at point A is 219.00 kV, while at point B is 5.98 kV and at point C is 3.54 kV. Thus, the ground potential rise decreases quickly from the current injected point, while tends to smoothness when the distance from the current injected point is long. If point (120, 60) and point (200, 40) are connected, the potential rises at point A, point B and point C are shown in Figure 5.18 [165]. It can be seen that at this situation the peak values of the potential at point A is 210.30 kV, while at point B is 5.94 kV and at point C is 3.51 kV.



**Figure 5.18: The transient ground potential rise at point A, point B and point C when point (120, 60) and point (200, 40) are connected [165]**

If point (40, 50) and point (100, 90) are connected by bare conductor, point (120, 60) and point (200, 40) are connected by bare conductor, and point (40, 0) and point (200, 0) are connected by bare conductor, the potential rises at point A, point B and point C are shown in Figure 5.19 [165]. It can be seen that at this situation the peak values of the potential at point A is 204.43 kV, while at point B is 5.92 kV and at point C is 3.50 kV.

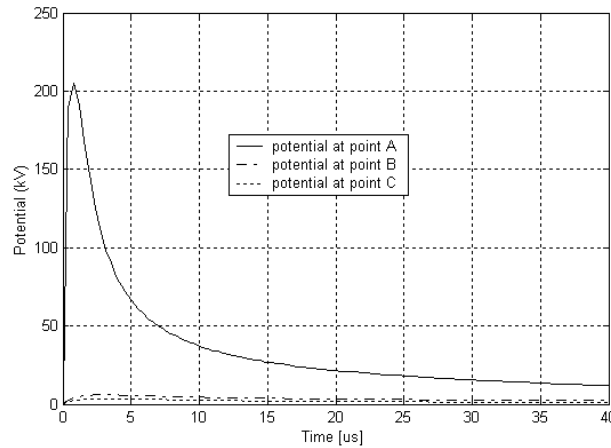


**Figure 5.19: The transient ground potential rise at point A, point B and point C when point (40, 50) and point (100,60) are connected by bare conductor, point (120, 60) and point (200, 40) are connected by bare conductor and point (40, 0), and point (200, 0) are connected by bare conductor [165]**

Thus, at transient, connecting the grounding systems has little effect on the ground potential rise. This may be because the impedance of the grounding electrode is very large and the most effective part of a grounding system at transient is the part near the current injected point.

### 5.3 Lightning surge calculation in substations

#### 5.3.1 Air-Insulated Substations

Watanabe et al. [166] have carried out a 1/10 reduced-scale experiment to measure surge voltages on an air-insulated substation, to which an impulse voltage is applied, and performed an FDTD computation that simulates the experiment. Figure 5.20 shows the small-scale substation model constructed for their experiment. Figure 5.21 shows its plan view: an impulse voltage is applied to the terminal of Line B-2, and surge voltages are measured at the voltage application point and at the number-2 transformer. Figure 5.22 shows measured and FDTD-computed voltage waveforms. FDTD-computed waveforms agree well with the corresponding measured waveforms. Note that Oliveira and Sobrinho [167] have performed a similar computation for an air-insulated substation struck by lightning using the FDTD method.

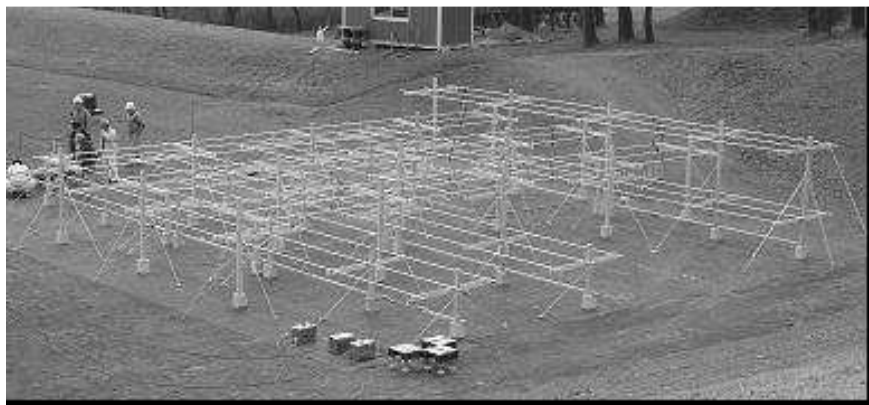


**Figure 5.20: 1/10 reduced-scale model of an air-insulated substation [166]**

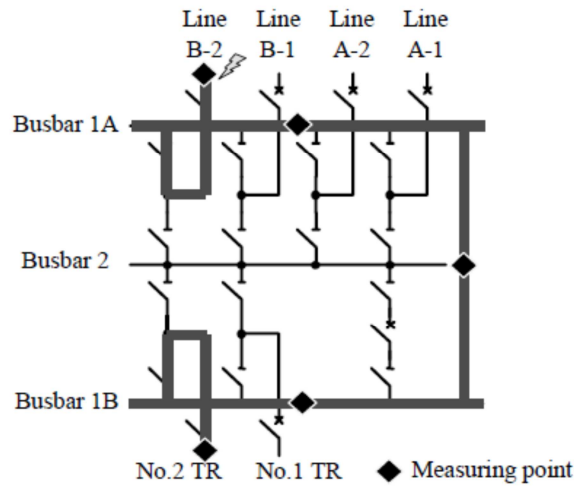


**Figure 5.21: Plan view of the small-scale model: an impulse voltage is applied to the terminal of Line B-2, and surge voltages are measured at the voltage application point and at the number-2 transformer [166]**

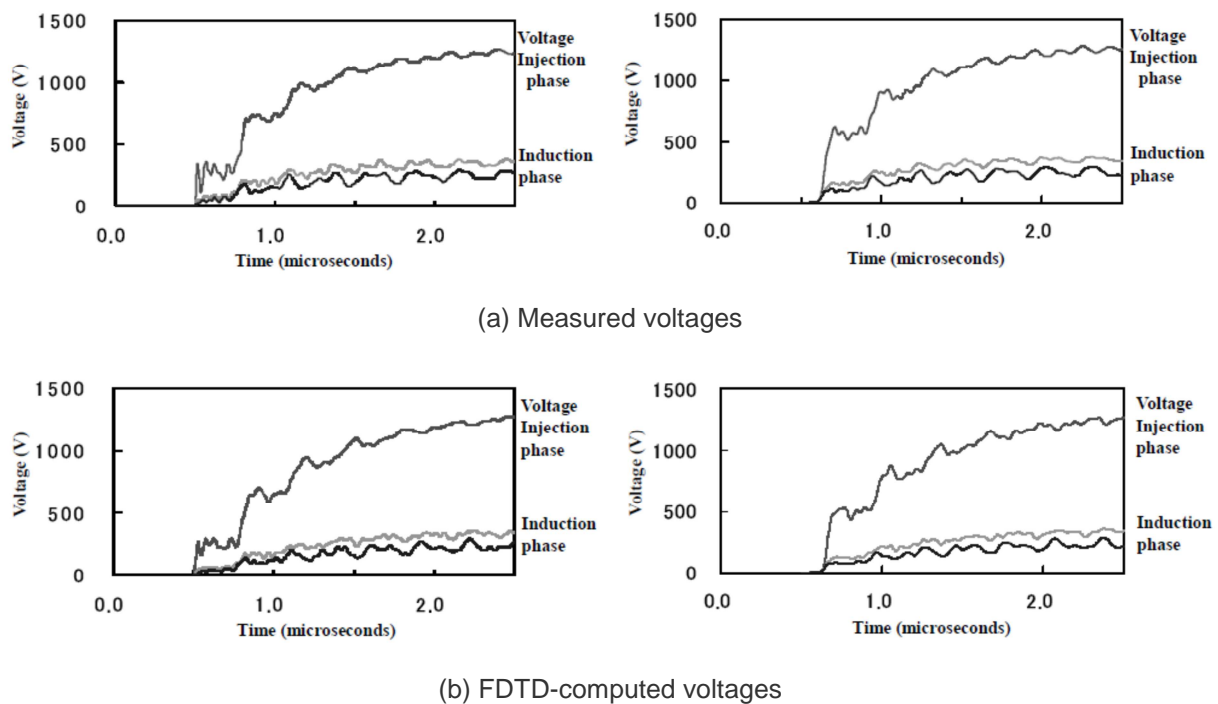


**Figure 5.22: Measured and FDTD-computed waveforms: the left-hand side shows voltages at the voltage application point, and the right-hand side shows voltages at the number-2 transformer [166]**

### 5.3.2 Influence of grounding on lightning surge calculation in substations

The influence of the transient model of the grounding grid on the lightning overvoltage of substation was analyzed by Zeng, et al. [168]. Figure 5.23 shows a typical configuration referring to a 110-kV gas-insulated substation (GIS) with one transmission line connected. The GIS bus of 33 m in length and the cable of 3 m are simulated by the single-conductor transmission line model. The arrester is simulated by the proposed model in [169]. The

transformer is simulated by a transmission-line model in [170], and other power apparatus, such as PT, cable end and bushing are simulated by capacitances of 100 pF and 300 pF respectively. It is worth observing that the effect of the transformer model has been investigated in many references (e.g. [14], [17]).

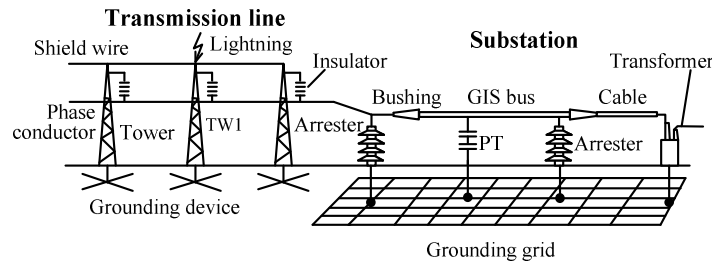


**Figure 5.23: A typical configuration of a 110 kV gas-insulated substation [166]**

The analyzed voltages of transformer and GIS bus by the proposed method and the traditional methods are compared in Figure 5.24 [168], they have large difference. The voltage applied on and the current through the surge arrester near the transformer are shown in Figure 5.25 [168], the voltage includes the voltage drop on the grounding grid model. The magnitudes of the transient voltages and currents are compared in Table 5.1 [168]. The transient voltages by the proposed method are much smaller than these by the traditional method, but the currents through the arrester by the proposed method are much higher than these by the traditional method due to high voltage drop of the grounding grid when the grounding grid is modeled as a lumped resistance. The transient grounding impedance of the grounding grid at the connecting point of the line-side arrester is shown in Figure 5.25 [168], which is in the region from 0.61 to 1.78  $\Omega$ . In the rising region of the applied lightning current, due to high  $di/dt$ , the inductive effect of the grounding conductor is very high, this leads the transient impedance to be very high, and then the effect of the soil ionization becomes strong, this leads to a decrease of the impedance. But in the wave-tail region, the inductive and ionization effects all become weak, then the impedance trends toward the power frequency impedance. So, the transient characteristics of grounding systems have strong influence on the lightning transient process of substation.

The actual wave process is considered in the proposed model, it is much closer to the actual condition. So, the analysed results of transient voltage obtained by traditional method exhibits higher values than the actual ones. However, a similar work presented in [171] shows a different conclusion and, in this respect, further investigations are needed.

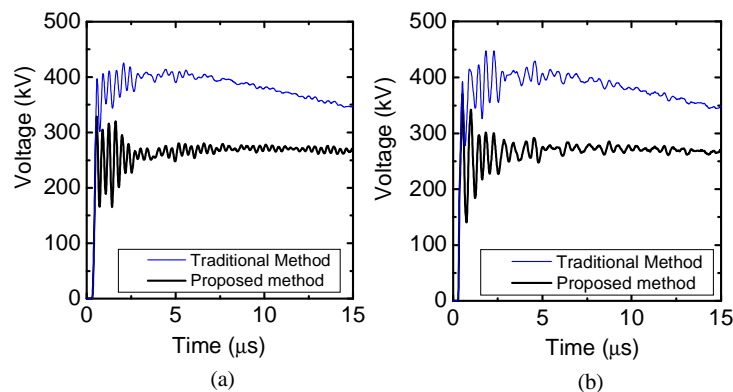


**Figure 5.24: The lightning transient voltages applied on (a) the GIS bus and (b) the transformer analyzed by the proposed and the traditional methods [168]**



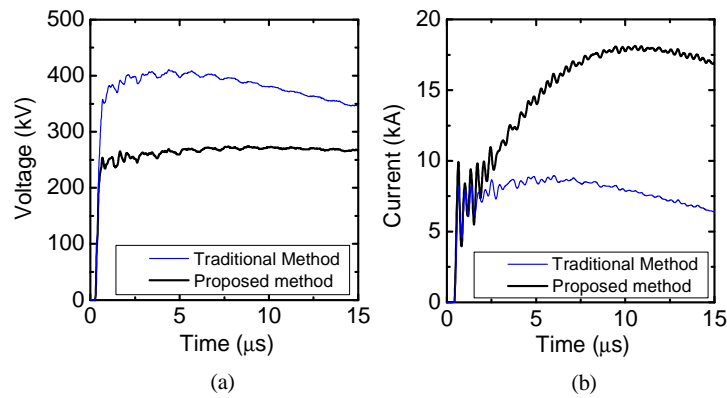


**Figure 5.25: (a) The transient voltages applied on and (b) transient current through the surge arrester near the transformer [168]**

Items		Traditional Method	Proposed Method	Difference
Voltage (kV)	Transformer	425.2	326.9	30.1%
	GIS Bus	447.5	370.4	20.8%
	Entry point of substation	527.2	470.3	12.1%
	Line-side arrester	415.3	281.6	47.5%
	Transformer-side arrester	410.8	268.9	52.8%
Current (kA)	Line-side arrester	10.3	19.6	-47.4%
	Transformer-side arrester	9.0	18.1	-50.3%

**Table no. 5.1: Comparison of Magnitudes of Voltages and Currents on Different Power Equipment by Traditional and Proposed Methods[168]**

## 5.4 Surge voltages on overhead lines

### 5.4.1 Lightning-induced surges on distribution lines computed by means of the MoM

Using the MoM in the frequency domain, Pokharel et al. [172] have reproduced lightning-induced voltages on an overhead horizontal wire of radius 0.25 m, length 25 m and height 0.5 m, measured by Ishii et al. [173]. Figure 5.26 shows the configuration of Ishii et al.'s small-scale experiment. In the experiment, a vertical return-stroke channel is represented by a coiled wire, along which a current wave propagates upward at the speed of about 125 m/μs. The close (to the simulated channel) end of the overhead horizontal wire is either terminated in a 430-Ω resistor or left open, and the remote end is terminated in a 430-Ω resistor. The lightning-induced voltages at both ends of the wire are measured using voltage probes having 20-pF input capacitance. Figure 5.27 shows MoM-computed and measured waveforms of induced voltages. Note that, in the MoM computations, the lightning channel was represented by a vertical wire having 1-Ω/m series distributed resistance and 3-μH/m series distributed inductance, and the ground conductivity and its relative permittivity are set to  $\sigma = 0.06$  S/m and  $\epsilon_r = 10$ , respectively. In Figure 5.28, MoM-computed voltage waveforms for the case of perfectly conducting ground are also shown for reference. Due to the finitely conducting ground, the polarity of the remote-end voltage is opposite to that of the close end.

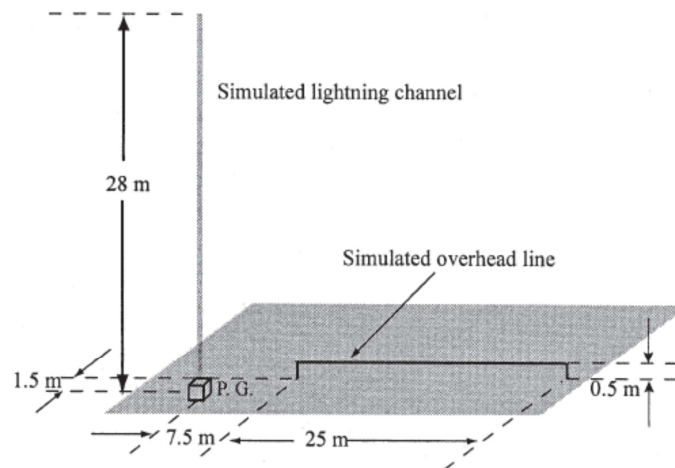
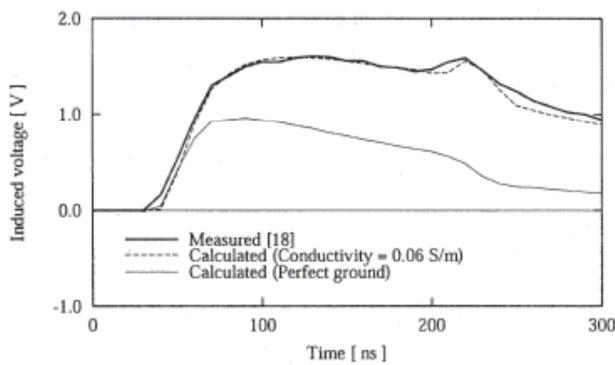
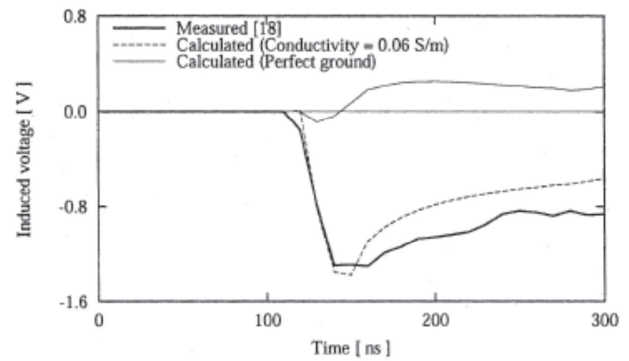


**Figure 5.26: Configuration of a small-scale experiment for measuring lightning-induced voltages [162]**



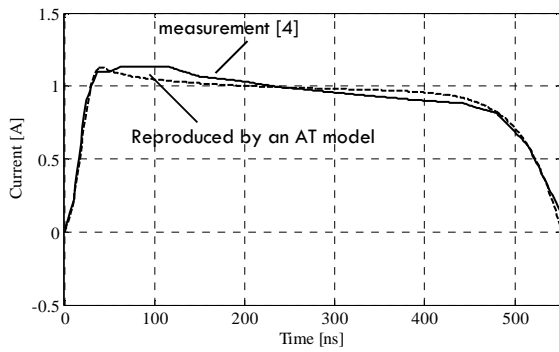
(a) Voltages at the close end



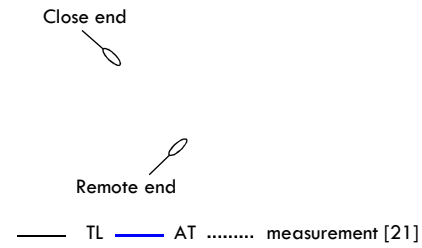
(b) Voltages at the remote end

**Figure 5.27: MoM-computed and measured waveforms of lightning induced voltages at both ends of the overhead wire, each end is terminated in a 430- $\Omega$  resistor**

Ishii *et al.* [173] have well reproduced lightning-induced voltages measured in their experiment with Agrawal *et al.*'s field-to-wire electromagnetic coupling model [174], Baba and Rakov [175] have reproduced the same measured waveforms using the FDTD method, and Silveira *et al.* [176] have reproduced them using the HEM method. In all of these computations, the ground conductivity and its relative permittivity are set to  $\sigma = 0.06$  S/m and  $\epsilon_r = 10$ . Yutthagowith *et al.* [177] have reproduced them using the partial element equivalent circuit (PEEC) method [178]. A lightning current is modelled by a transmission line and an antenna (AT). A speed of the lightning current in the AT model is controlled by additional internal inductance 8  $\mu$ H/m. Figure 5.28 (a) shows a comparison of the reproduced lightning current and a measured current [173]. Figure 5.28 (b) shows a comparison of a calculated induced voltage by the PEEC method [177] and the measured voltage [173]. A good agreement is observed. It should be noted that the current employed in [31] has a lower speed than the measured current [173].



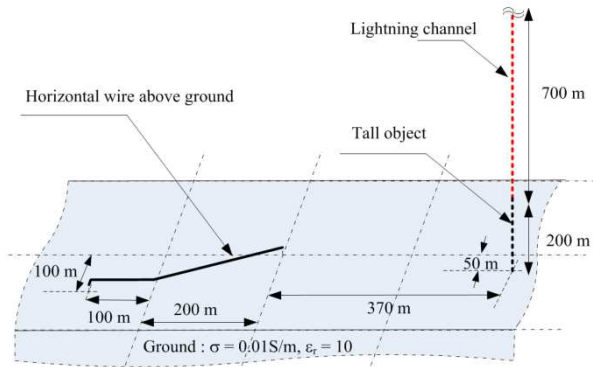
(a) Lightning current



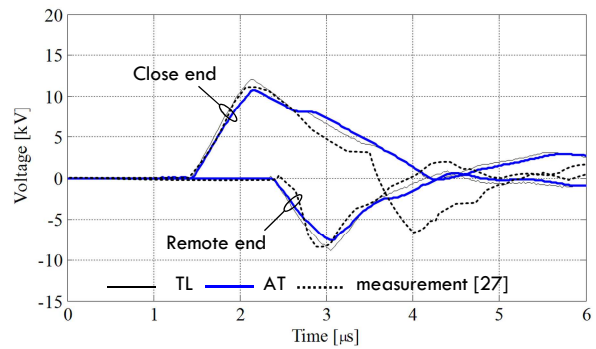
(b) Lightning induced voltages

**Figure 5.28: PEEC-computed and measured waveforms of a lightning current and lightning induced voltages at both ends of the overhead wire, each end is terminated in a  $430\text{-}\Omega$  resistor**

Michishita *et al.* [179] have measured lightning induced voltage due to a lightning struck to a tall object. The tall object with height 200 m was set at 375 m from the close end of a line. The lines were approximately 300 m in length and 11 m above ground. A resistor of  $400\text{ }\Omega$  is connected at the both ends of the line. Yutthagowith *et al.* have reproduced a lightning induced voltage in this case using the partial element equivalent circuit (PEEC) method [178]. The configuration and parameters in the PEEC calculation are illustrated in Figure 5.29 (a). Figure 5.29 (b) shows the PEEC-computed voltages [177] and measured voltages and a good agreement is observed. It is noted that Michishita *et al.* [179] have reproduced lightning-induced voltages with Agrawal *et al.*'s field-to-wire electromagnetic coupling model [174]



(a) Configuration of an experiment [38]



(b) Lightning induced voltage [36]

**Figure 5.29: Configuration of the observation system and calculated lightning induced voltages**

Using the MoM in the time domain, Pokharel *et al.* [180] have computed lightning-induced voltages on a 500-m long overhead wire, which is located above perfectly conducting ground. The overhead wire is terminated in  $540\text{-}\Omega$  resistance at each end, and is connected to ground in the middle of the wire via surge arrester. The surge arrester is represented by a non-linear resistor whose characteristics were shown in Figure 5.30. Figure 5.31 shows computed waveforms of lightning-induced voltage in the middle of the wire with or without the surge arrester and the arrester current. Note that the simulated lightning channel was located 100 m away from the middle of the overhead wire, the magnitude of lightning current was set to 10 kA, and its risetime is set to  $1\text{ }\mu\text{s}$ . Using the same method, Moini *et al.* [181] have performed computation of lightning induced voltages on vertically-arranged and horizontally-arranged multi-phase conductors above perfectly conducting ground.

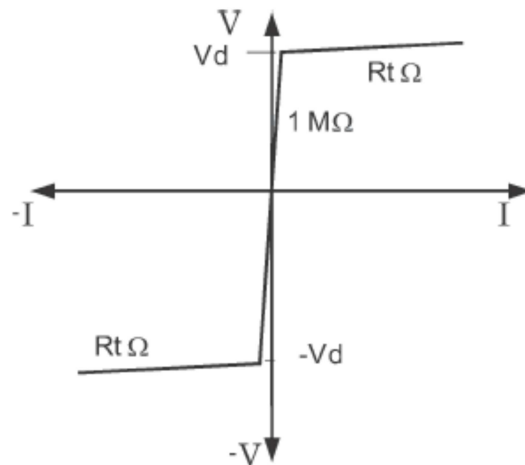


**Figure 5.30: Approximate voltage vs. current characteristics of non-linear resistance representing a surge arrester, employed by Pokharel et al. [179] in their computations using the MoM in the time domain.  $V_d$  is set to 30 kV**

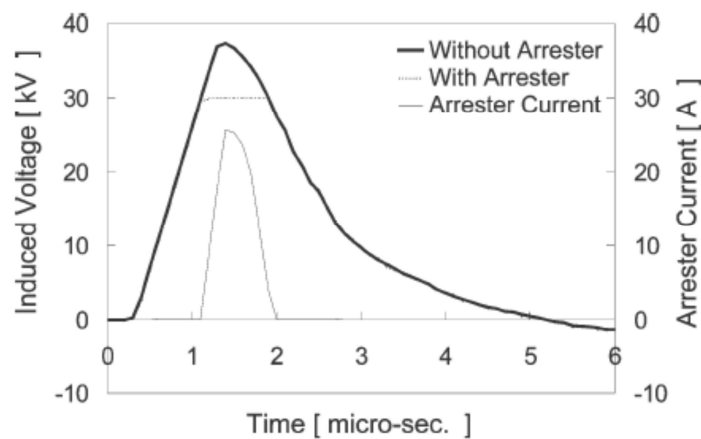


**Figure 5.31: Waveforms of lightning-induced voltage in the middle of a 500-m long overhead wire with or without a surge arrester and the arrester current, computed using the MoM in the time domain [179]**

#### 5.4.2 LEMP and induced surges calculation by means of the FEMTD in overhead lines above a lossy ground

As discussed in [182], further useful application of numerical resolution of full-wave Maxwell's is related to development of benchmark results useful to assess the uncertainties introduced by approximate models usually applied for the calculation of lightning induced voltages on overhead lines. The evaluation of induced voltages requires models for the calculation of both the electromagnetic field generated by the return stroke (Lightning Electromagnetic Pulse – LEMP) starting from the time-spatial distribution of the lightning current along the channel (e.g. [183, 184]), and its coupling with the line conductors.

Different methodologies and approaches have been presented in the literature for the LEMP calculation. They can be grouped as follows: (i) approaches that use the dipole technique (e.g. [185-189]), approaches based on the implementation of specific algorithms (e.g. [190, 191]) able to solve the so-called Sommerfeld integrals [195] for the

expressions of electromagnetic fields radiated by dipoles [193, 195], and (iii) approaches that use numerical electromagnetic analysis (NEA) methods. Recent examples of the use of NEA methods are the method of moment (e.g., [195-197]), the FDTD technique (e.g., [198–201]) and the Finite Element Method (FEM) [202].

It is worth observing that the same NEA methods can be applied for the calculation of the induced voltages along the overhead line. However, the most common approaches implement a LEMP-to-line coupling model based on the transmission line approximation (e.g. [203-205]).

Within the above-mentioned context, this section of the brochure aims at comparing the results obtained by using the approximated models implemented in the Lightning Induced Overvoltage (LIOV) code [206] and the results obtained by using a full-wave time-domain FEM model [207]. The comparison is carried out with reference to a typical benchmark configuration composed by a single conductor overhead line of finite length (with opened terminations) above an ideal or lossy ground.

As described in [208], both the so-called monopole and dipole techniques can be adopted for the LEMP calculation. Note that very recently, antenna over a perfectly conducting plane, are obtained by solving Maxwell's equations in terms of retarded scalar and vector potentials [209, 210].

For distances not exceeding a few kilometres, the perfectly conducting ground assumption does not significantly affect the calculation of the vertical electric field component and of the horizontal magnetic field component [188, 205, 210]. Instead, the calculation of the horizontal component of the electric field is appreciably affected by the finite conductivity of the ground.

Although the intensity of the horizontal field component is much smaller than that of the vertical one, it plays an important role in the LEMP-to-transmission line coupling [206] and, hence, it has to be determined accurately. Several approaches have been proposed in the literature for its evaluation (see a recent review presented in [211]).

In this section we have made reference to the results provided by the LIOV code that implements the field equations obtained by applying the dipole technique and the approximated Cooray-Rubinstein formula [187-189, 212] to take in account the finite ground conductivity in the evaluation of the horizontal component of the electric field.

Concerning the lightning induced voltage calculation, it can be performed either in the time or in the frequency domain. The LIOV code performs the solution in the time domain as it allows the handling, in a straightforward manner, of nonlinear phenomena such as corona, changes in the network configuration (due, for instance, to an insulation flashover originated by the lightning surge), and the presence of surge arresters. As mentioned, the LIOV code is based on the Agrawal et al. LEMP-to-line coupling model suitably adapted for the case of a line above a lossy ground [213, 214].

Concerning NEA approaches, they are based on the direct numerical resolution of full wave Maxwell's equation relaxing all the assumptions usually made for circuit-theory based approaches. Typical examples are based on the use of the following numerical resolution schemes: method of moments (MoM) in the frequency and time domains (e.g. [195-197, 215-220]), the finite-difference time-domain (FDTD) method (e.g. [198-201, 221, 222]), and the FEM (e.g. [202]).

This section makes reference to the FEM method. In particular, the adopted simulation environment is the Comsol Multiphysics [207] that numerically integrates a weak-form representation of the time-domain wave equation of the magnetic vector potential [202].

Charge acceleration technique was also used to compute LEMP [209]. By making reference to the dipole technique and to the geometry shown in Figure 5.32, the expressions for the electromagnetic field radiated by a vertical dipole of length  $dz'$  at a height  $z'$  along the lightning channel, assumed as a vertical



As it can be seen, the waveshapes obtained by using the FEM model are in close agreement with those provided by the LIOV code.

For the case of a finitely conducting ground, Figure 5.34 shows the comparison between the results obtained by using: the FEM model, the LIOV code and those obtained by the solution of the Sommerfeld integrals. In particular, waveshapes of Figure 5.34 refer to the horizontal component of the electric field at the same observation points of Figure 5.33. The assumed ground conductivity is equal to 0.001 S/m and the lightning current parameters were the same as those adopted for the case of an ideal ground.

Figure 5.34 shows that, for the case of a lossy ground, the results obtained by the FEM model are in good agreement with those obtained by the numerical resolution of the Sommerfeld integrals that could be considered as a benchmark. Additionally, the results provided by the LIOV code, in which the Cooray-Rubinstein formula is implemented, exhibit a slight discrepancy with respect to the others in the early-time region where they are characterized by a higher time derivative and a higher negative-polarity peak value. As discussed recently by Cooray [225], this might be due to the fact that propagation effects are neglected in the magnetic field that is being used as an input in the Cooray-Rubinstein formula. The late-time responses of all the three waveshapes are virtually identical.

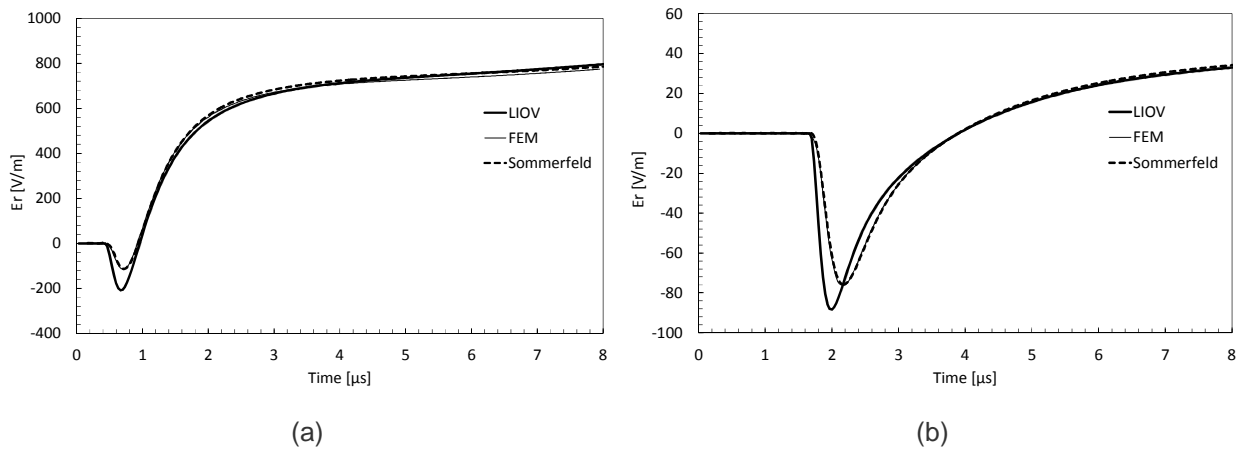


**Figure 5.34: Comparison among radial components of the electric field calculated using the LIOV code, by the numerical solution of the Sommerfeld integrals and by the FEM model. Ground conductivity: 0.001 S/m, lightning current: 12 kA peak, 40 kA/μs maximum time derivative. Observation points: a) 130 m, b) 500 m**

In what follows we made reference to the calculation of lightning-induced voltages on overhead lines. In particular, the geometry adopted to compare LEMP-induced overvoltages in overhead lines is illustrated in Figure 5.35. It is composed by a single-conductor, 1-km long line placed at 10 m above the ground and open circuited at both ends.

The FEM model adopted for the calculation of the induced voltages along the overhead conductor needs to be three-dimensional due to the presence of the line-scattered field that eliminates the cylindrical symmetry. The line is represented as a perfectly conducting thin wire. The induced voltages along the line are calculated by integrating the electric field along straight vertical paths between the line and the ground at the considered observation points located at line center and terminals.



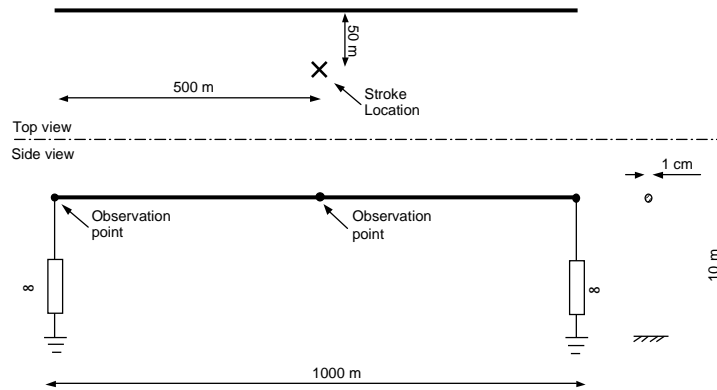


**Figure 5.35: Adopted line configuration and stroke location for the lightning-induced voltages calculation**

Figure 5.36 and Figure 5.37 show the comparison between lightning-induced voltages calculated by means of the FEM model and the LIOV code: Figure 5.36 presents the comparison for the ideal ground case, whilst Figure 5.37 presents the comparison for a ground conductivity equal to 0.001 S/m. All the calculations have been carried out using the same lightning current parameters adopted in the in the previous section.

For the ideal ground case (Figure 5.36), all the waveshapes are in quite good agreement. However, the ones obtained by means of the FEM model show a larger time lag between subsequent traveling wave reflections taking place at the line terminations, with respect to the corresponding waveforms calculated by the LIOV code. The difference can be attributed to the transmission line approximation of the Agrawal et al. coupling model adopted in the LIOV code in which the per-unit-length parameters are calculated for an infinitely long line. In this respect, it is worth noting that the FEM model inherently takes into account the finite length of the line.

For the case of a lossy ground (Figure 5.37), the voltage waveforms calculated by using the FEM model show a pronounced attenuation and distortion in the late time response with respect to those provided by the LIOV code. The difference is mainly attributed to the different approaches adopted by the LIOV code and by the FEM model in order to take into account the effects of the finite conductivity of the ground in both the LEMP calculation and in the simulation of the propagation of traveling waves along the line.

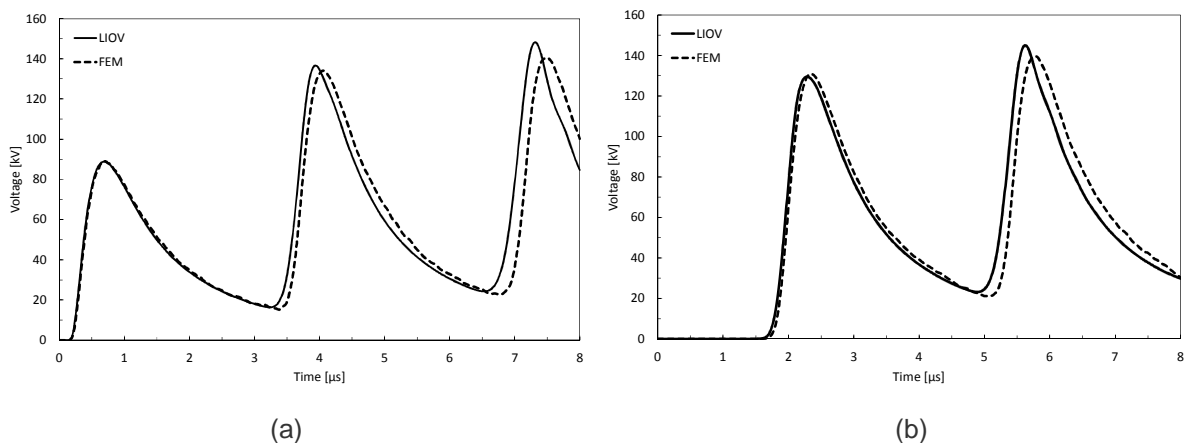


**Figure 5.36: Comparison between lightning induced voltages calculated by means of the FEM model and using the LIOV code with reference to the configuration of Figure 5.35 and an ideal ground: a) lightning-induced voltages at the middle of the line, b) lightning-induced voltages at one of the two line terminations**



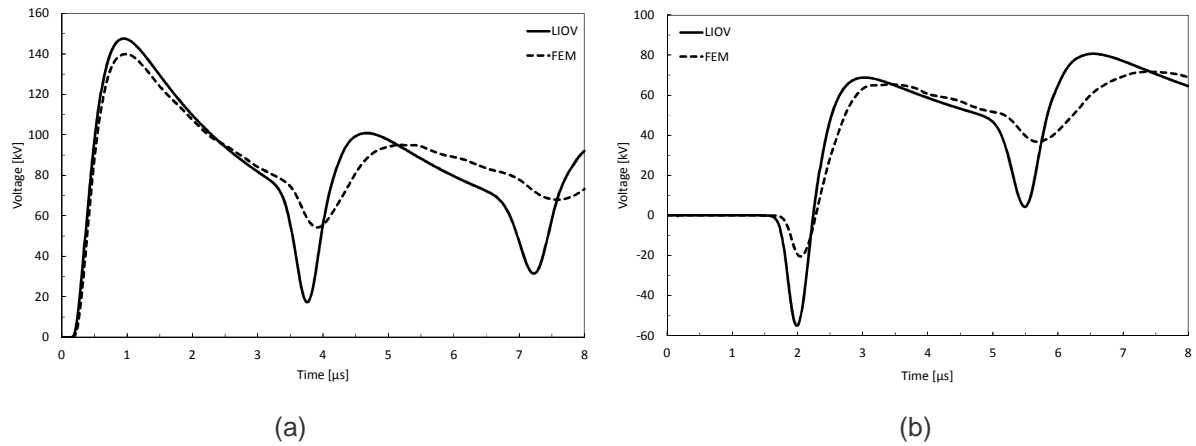


**Figure 5.37: Comparison between lightning induced voltages calculated by means of a FEM model and using the LIOV code with reference to the configuration of Figure 5.35 and a 0.001 S/m conducting ground: a) lightning-induced voltages at the middle of the line, b) lightning-induced voltages at one of the two line terminations**

#### 5.4.3 Influence of grounding on surge propagation in overhead transmission lines

Based on time-domain method, the algorithm of impulse characteristic analysis of grounding can be easily integrated and linked to the general electromagnetic program EMTP. Then the influence of the grounding on surge propagation of transmission line was analyzed by He, et al [226]. The analyzed example was 110-kV transmission lines. A 15.9 m-long horizontal grounding rod which is buried at a depth of 0.8m is  $10 \Omega$ . And an 11.5 m-long vertical grounding rod at a depth of 1m also has the same power frequency grounding resistance of  $10 \Omega$ . Both of them are imported as grounding devices of transmission towers to compute the lightning overvoltage on 110-kV transmission lines. The results are compared with those obtained through the traditional method in which the grounding resistance is simplified as a constant resistance of  $10 \Omega$ . The potential on the top of tower and the voltage on the insulator are illustrated in Figure 5.38 and Figure 5.39 [226]. And the grounding potential rises (GPRs) are shown in Figure 5.40 [226].

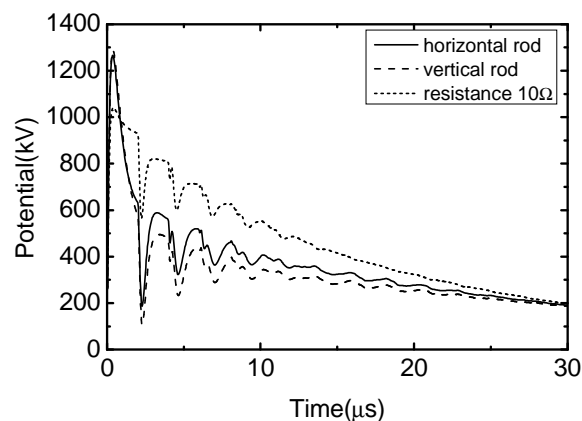


**Figure 5.38: Potential on top of tower [226]**

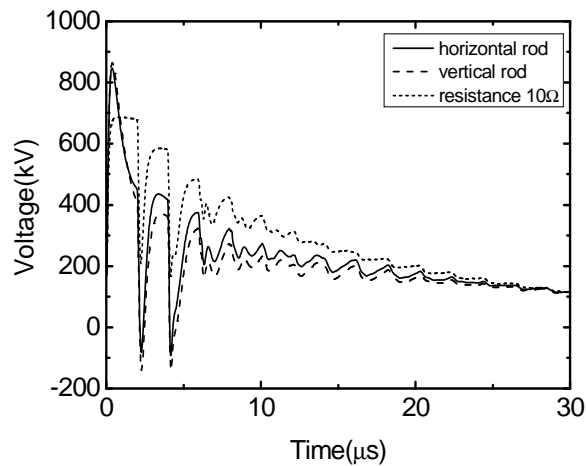


**Figure 5.39: Voltage on insulator [226]**

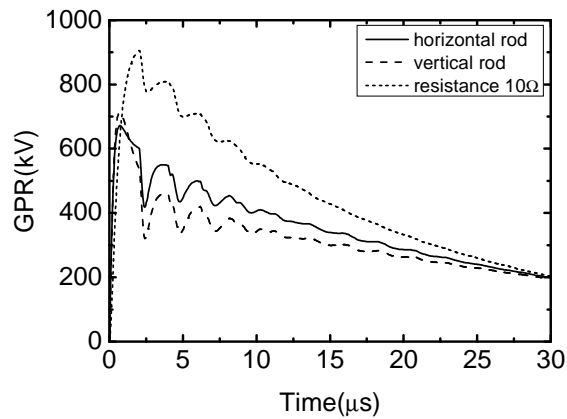


**Figure 5.40: Ground potential rise [226]**

We can see from Figure 5.38 that the transient characteristics of these three models are quite different, although they have the same power frequency grounding resistance. Taking account of the time-varying parameter of impulse resistance, the peak value of the potential is much higher than that obtained though the method using constant resistances. And the potential decreases quickly to a certain level within a short time. But if a constant resistance is used as the grounding resistance to compute the overvoltage, the potential reduces slowly and keeps at a high level from a long time. A similar trend can also be seen in Figure 5.39. It can be seen from Figure 5.40 that the ground potential computed through traditional method is much higher than those taking account of the impulse characteristics. From all these three figures, we can see that the waveforms obtained with the proposed grounding model [168] are quite different from those with constant resistance. The differences can affect a lot on the lightning-withstand characteristic of transmission lines. However, it should be noted that different, and more realistic grounding electrode configurations, might provide a different answer and lead to a different conclusion. In this respect, further investigations are definitely needed.

### 5.5 Propagation characteristics of PLC signals along power coaxial cables

Okazima et al. [227] have investigated, using the FDTD method in the two-dimensional (2D) cylindrical coordinate system, the propagation characteristics of a **power line communication (PLC)** signal of frequency 30 MHz along a single-core power cable having two 3-mm thick semiconducting layers. For the conductivity of the semiconducting layers, a wide range from  $10^{-5}$  to  $10^5$  S/m is considered. Figure 5.41 shows a 130-m long single-core power cable to be analysed. The radius of the core conductor is set to 5 mm, and the inner radius of the sheath conductor is set to 25 mm. Both the core and the sheath conductor are perfectly conducting. Between the core and the 14-mm thick insulating layer of relative permittivity of 3, and between the insulating layer and the sheath conductor, 3-mm thick semiconducting layers are installed. The relative permittivity of the semiconducting layers is set to  $\epsilon_r=3$ . At one of the ends of the cable, a 10-V single wave voltage pulse, which is the positive half cycle of a sine wave of frequency  $f=30$  MHz, is applied between the core and the sheath conductor. Figure 5.42 shows the dependence of the propagation speed of a 30-MHz voltage pulse on  $\sigma$ . Note that the propagation speed is calculated from the propagation distances from the voltage excitation point to 20, 40, 60, 80, and 100 m and the corresponding propagation times, evaluated tracking the voltage pulse peak. Figure 5.43 shows the dependence of the magnitude of the voltage between the core and the sheath conductor at distance 100 m from the excitation point on  $\sigma$  when a 30-MHz and 10-V pulse is injected.

It appears from Figure 5.43 that the magnitude of a voltage pulse decreases with increasing propagation distance in all cases considered. However, the dependence of attenuation on  $\sigma$  is not monotonous: attenuation is significant around  $\sigma=10^{-3}$  and  $10^3$  S/m, while it is not when  $\sigma$  is lower than about  $10^{-5}$  S/m or  $\sigma$  is around 1 S/m. When  $\sigma=10^{-3}$  S/m and  $10^3$  S/m, dispersion is also marked. Therefore, it is quite difficult to conduct PLCs in a system having a power cable with semiconducting-layer conductivity of about  $\sigma=10^{-3}$  or  $10^3$  S/m. The reason for the significant attenuation and dispersion around  $\sigma=10^{-3}$  S/m is that charging and discharging processes of the layer become observable since the time constant  $\tau = CR$  ( $=27$  ns) of the semiconducting layer becomes close to the half cycle (17 ns) of a 30 MHz signal. In this condition, the conductance of the semiconducting layer is close to its susceptance. The reason for the attenuation and dispersion around  $\sigma=10^3$  S/m is that axial conduction current flows in the lossy semiconducting layers because a penetration depth (2 mm) for  $f=30$  MHz and  $\sigma=10^3$  S/m is close to the thickness of the semiconducting layer (3 mm).

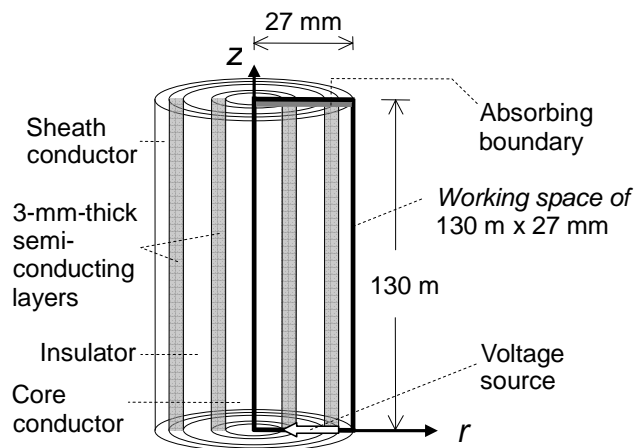


**Figure 5.41: 130-m long single-core power cable with semiconducting layers, to be analysed using the 2D-FDTD method [227]**

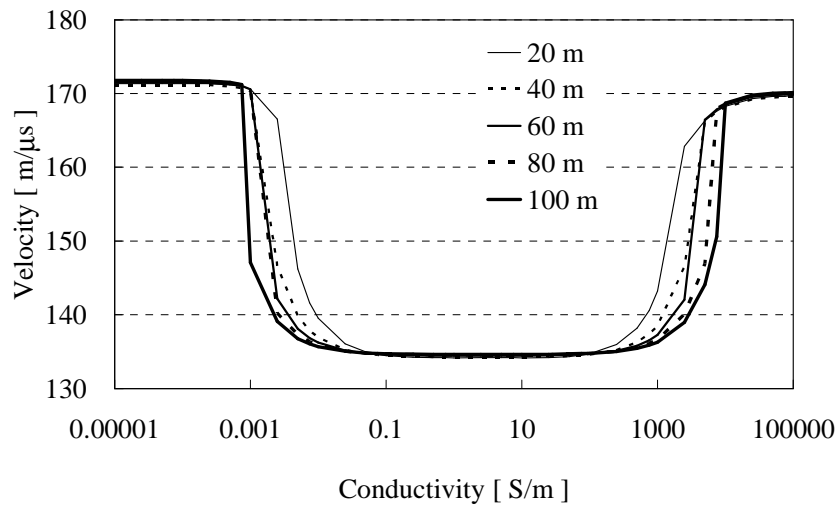


**Figure 5.42: 2D-FDTD-computed dependence of the propagation speed of a 30-MHz voltage pulse on the semiconducting-layer conductivity  $\sigma$  [227]**

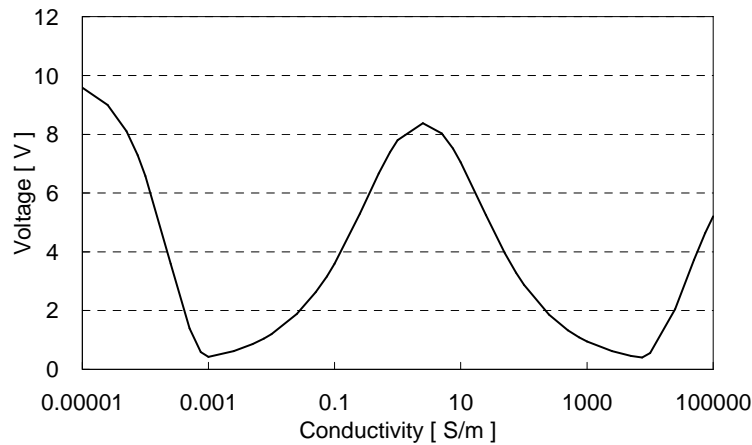


**Figure 5.43: 2D-FDTD-computed dependence of the magnitude of the voltage between the core and the sheath conductor at distance 100 m from the excitation point on the semiconducting-layer conductivity  $\sigma$  when a 30-MHz and 10-V pulse is injected [227]**

## 5.6 Lightning surge characteristics of a wind-turbine tower

Yamamoto *et al.* [228] have investigated the lightning protection of wind turbine generator systems by using a reduced-size wind turbine model and the FDTD analyses. The reduced-size model used in the experiments and analyses is a 3/100-scale model of an actual wind turbine generator system that has blades with a length of 25 m and a tower that is 50 m high. The reduced-size model was set up as shown in Figure 5.44 and the experiments and analyses have been carried out. Figure 5.44 shows the case that the assumed point of the lightning strokes is the tip of one of the blades. In ref. [228], the case that assumed point of the lightning strokes is the rear portion of the nacelle has also been investigated in the ref. [228].  $V_{11}$  to  $V_{14}$  in Figure 5.45 represent the voltage differences between the incoming conductor from a distant point and equipment in the tower foot. The voltage difference is caused by the voltage increase at the tower foot. The voltage difference becomes an overvoltage between the power line and the power converter or transformer on the ground level installed inside the tower or that between a communication line and a telecommunication device. The measured and calculated results are shown in Figure 5.46 under the conditions of the grounding resistance: 9.4  $\Omega$  and the wave front of the injected current: 4 ns. The

FDTD calculated result agrees well with the measurement, it has been confirmed that the FDTD method is also useful to analyze the voltage potential rises.

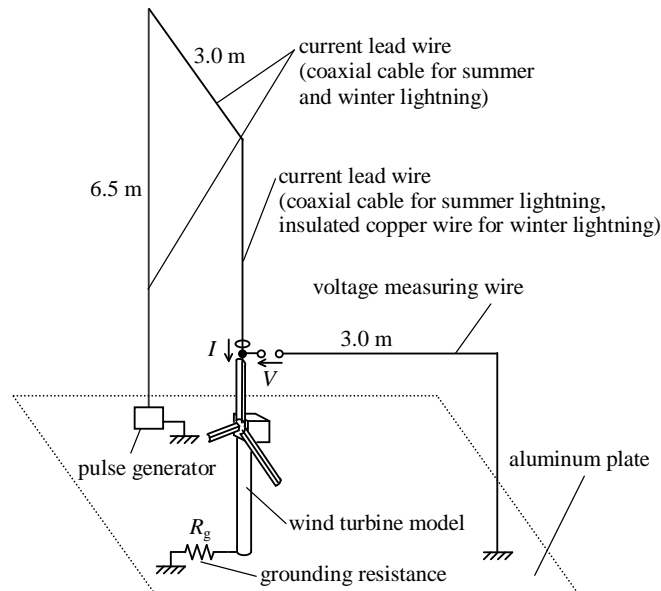


**Figure 5.44: Configuration of experimental setup in case of summer and winter lightning strokes on one of the blades [228]**

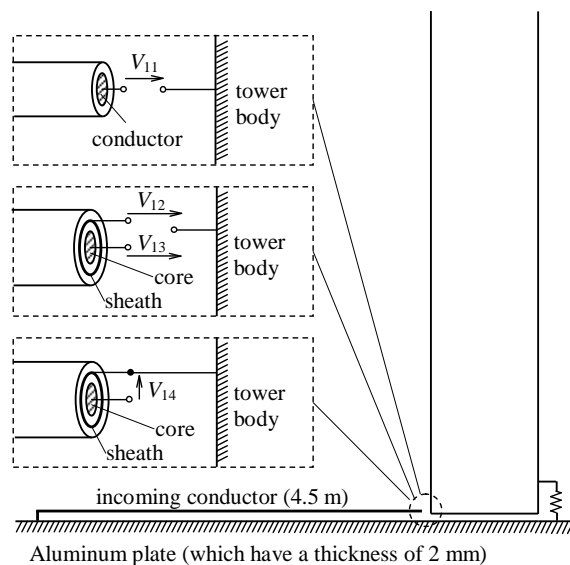


**Figure 5.45: Configuration of incoming conductors into the wind turbine foot to measure and analyse overvoltage between the incoming conductors and equipment in the tower foot [228]**

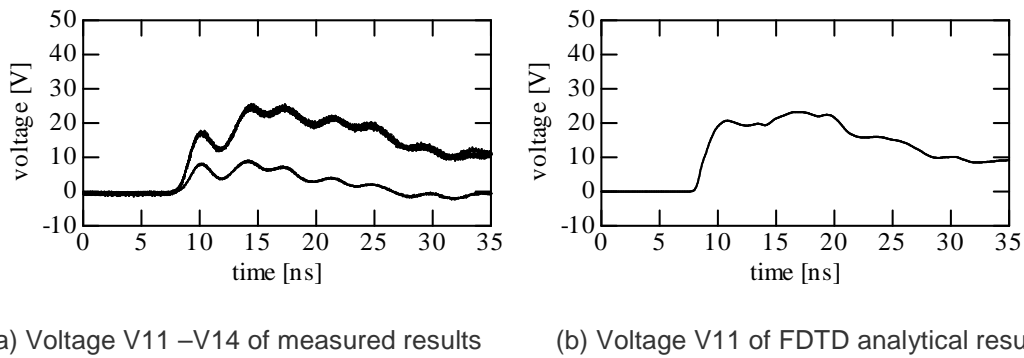


**Figure 5.46: Potential differences between the incoming conductor and equipment in the tower foot. The grounding resistance is  $9.4 \Omega$  and the wave front of the injected current is 4 ns [228]**

Yamamoto et al. [224] have also investigated the transient grounding characteristics of a wind turbine generator system. The wind turbine generator system used for the field test and the FDTD analyses is located at a unique disposal site. The grounding system consists of the foundation, the foundation feet and grounding mesh as shown in Figure 5.47. It is well known that most of the transient grounding characteristics of wind turbines are inductive because the steady-state grounding resistance is quite low such as less than  $10 \Omega$  in most instances. The characteristics are confirmed as shown in Figure 5.48.

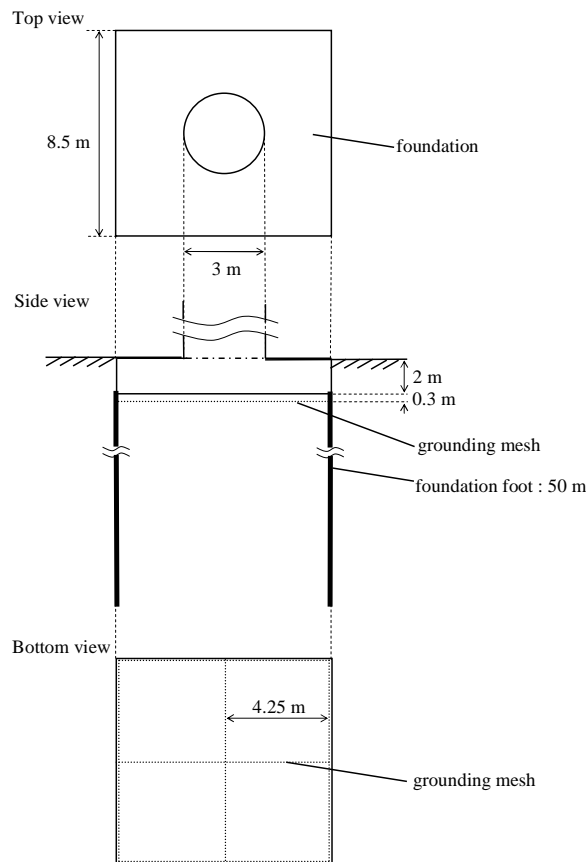
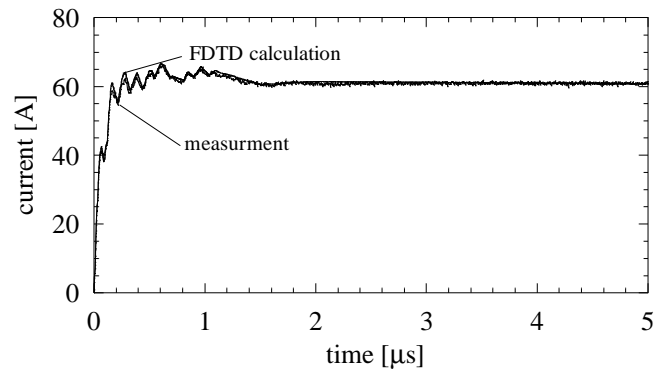
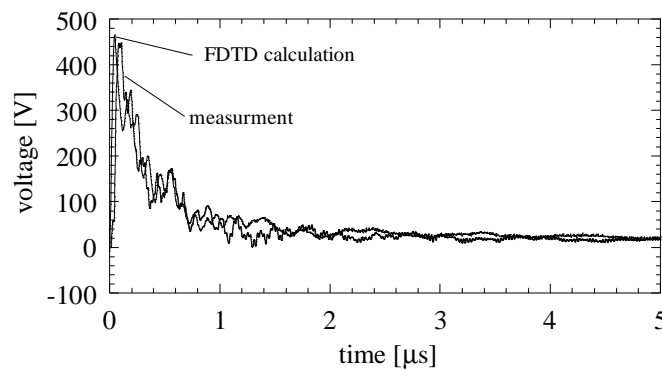


**Figure 5.47: Foundation of the actual wind turbine generator system [229]**



(a) Injected currents into the foundation



(b) Potential rises of the foundation

**Figure 5.48: FDTD calculated results of the grounding system compared with the measured results [229]**

Ametani *et al.* [230] have considered the transitions of the magnetic fields in a nacelle due to lightning strokes to a wind turbine by using the FDTD method. The analytical models are based on a wind turbine generator system of 2 MW. The nacelle is modelled as a rectangular parallelepiped object having dimensions of 4 m  $\times$  10 m  $\times$  4 m as shown in Figure 5.49. The magnetic field distributions of the x direction on yz plane at x = 1.5 m and that of the zx plane at y = 0.5 m are shown in Figures 5.50 and 5.51. The plane view of the magnetic fields of Figures 5.50 and 5.51 are at the time of 1.2  $\mu$ s and 0.35  $\mu$ s respectively. From those magnetic fields and the current flows on the grids constructing the nacelle and the down conductors in the blades, it is evident that the current flowing through the down conductor of the blades exerts a greater influence on the magnetic fields in the nacelle than the current flowing in the grids of the nacelle.

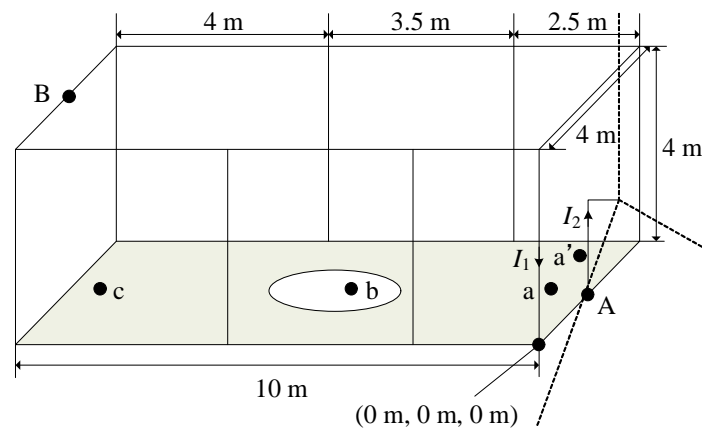
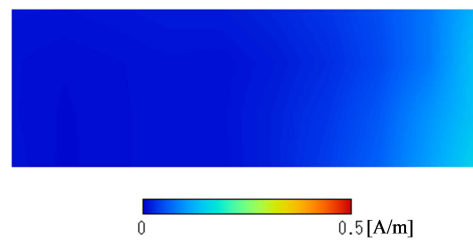
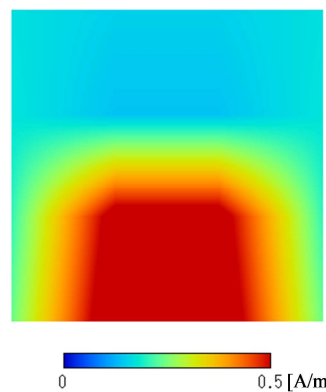


Figure 5.49: Nacelle model with output points of magnetic fields and currents [230]



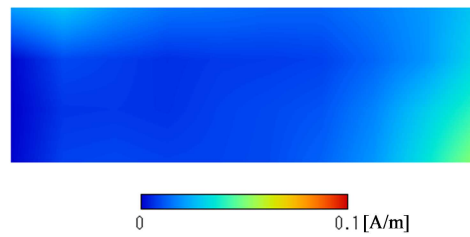
(a) Magnetic fields to x direction on yz plane at  $x = 1.5$  m



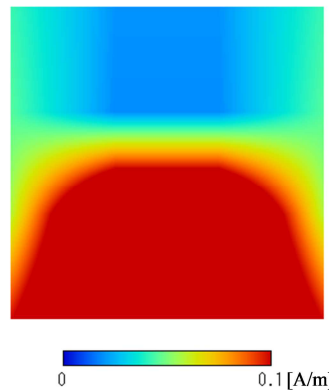
(b) Magnetic fields to y direction on zx plane at  $x = 0.5$  m

Figure 5.50: Plane view of magnetic fields at  $1.2 \mu\text{s}$  (lightning strokes at the tip of the blade) [230]





(a) Magnetic fields to x direction on yz plane at  $x = 1.5$  m



(b) Magnetic fields to y direction on zx plane at  $x = 0.5$  m

**Figure 5.51: Plane view of magnetic fields at  $0.35 \mu\text{s}$  (lightning strokes to the rear portion of the nacelle) [230]**

### 5.7 Full-Maxwell 3D simulations of very fast transients (VFTs) in GIS

GIS are very important high voltage (HV) components of electric power distribution and transmission systems. They consist of HV switching devices (circuit breakers, disconnectors, and earthing switches), different connecting pieces and interface components (bushings) to overhead lines, transformers etc. They are usually installed in the nodes of HV networks to perform switching operations needed for power system control and maintenance.

VFT in GIS are initiated by an electrical breakdown between the contacts of the disconnector during its switching operations after the HV circuit breaker has interrupted the service current [231]. VFT are electromagnetic (EM) waves travelling in the pressurized  $\text{SF}_6$  volume along the bus-ducts attached to the disconnector. After an electromagnetic wave encounter any geometrical discontinuity (such as an insulator, open end, bushing, etc) along their path it is partially or totally reflected. Therefore, initiated as an EM impulse and continuing to exist as a superposition of a large number of different multiply reflected EM waves, VFTs have complicated non-harmonic time dependence and cover a wide frequency range from 100 kHz to 100 MHz [232].

The voltage at any particular position of the GIS section affected by VFT is a superposition of the service voltage and traveling VFT waves. Therefore, the peaks of VFT waves temporarily yield significantly higher values of voltage and electric field in GIS compared to their nominal values. As the rated voltage increases, the difference between the rated impulse withstand voltage and the VFTO (very fast transient overvoltage) decreases. For ultra high voltages (UHV) applications, VFTO can become the limiting dielectric stress which defines the dimensions in certain cases.

Due to their significant influence on the GIS dielectric behaviour, the VFTOs must be either accurately measured (very expensive and time consuming) or reliably predicated by simulations (cheaper and allowing for parametric studies and optimization). Up to now predominant approach for simulating VFTOs is based on the representation of

the GIS components by their equivalent circuits with distributed parameters (transmission lines) and time-domain solution of circuit equations for the obtained equivalent network [232, 233]. The main drawback of this method is the lack of geometrical details and local field values that are critical for the dielectric design.

The purpose of this section is to suggest a new approach for simulating VFTs by directly solving Maxwell equations in time-domain on real-life 3D GIS geometries, to present the obtained results and to verify them by comparison with circuit simulations and measurements.

Two years ago ABB Switzerland Ltd was requested to design and deliver 1100kV GIS equipment for China's new UHV network [234]. This order resulted in the development of the new GIS type ELK-5 with 1100kV rated voltage<sup>3</sup>. Due to its high operating voltage, the topics related to the VFTs became of paramount importance for the dielectric design of ELK-5.

In January 2009, at China's Jingmen 1100 kV substation, Shiky/ABB's first ELK-5 was successfully installed and energized, and it has been in operation ever since. The VFT topics and concerns arising from the development of ELK-5 were main motivation and driver for our full-Maxwell simulations presented in this section.

The simplified 3D geometry of the GIS type ELK-5 is presented in Figure 5.52. In the same figure are also shown the modelling details, boundary conditions, and materials involved.

For 3D full-Maxwell wave simulations the commercially available electromagnetic field solver COMSOL was used [235]. The COMSOL is a modern vector FEM based full-Maxwell solver with a classical field formulation implemented based on the vector magnetic potential [235, 236]. The detailed description of the vector FEMTD approach for full-wave 3D analysis including the boundary value problem (BVP) and its FEM discretization by using vector elements is given in Section 3.3.2.

As presented in Figure 5.52, the simulation model consists of the disconnector region connected with the metallic bus-ducts surrounded by the pressurized SF<sub>6</sub> gas (light blue). The bus-ducts are mechanically supported by the spacers made of solid insulation material (green). Due to the high-frequency nature of VFTs all the metallic components are considered to be made of perfect electric conductor. Therefore, the volume of those components was not meshed and their outer surfaces are used as boundary conditions (BCs). The structure is considered to be connected to the network over a bushing and power transformer. For this reason the interface boundary with voltage input and surface wave impedance is introduced into the model (bottom-left).

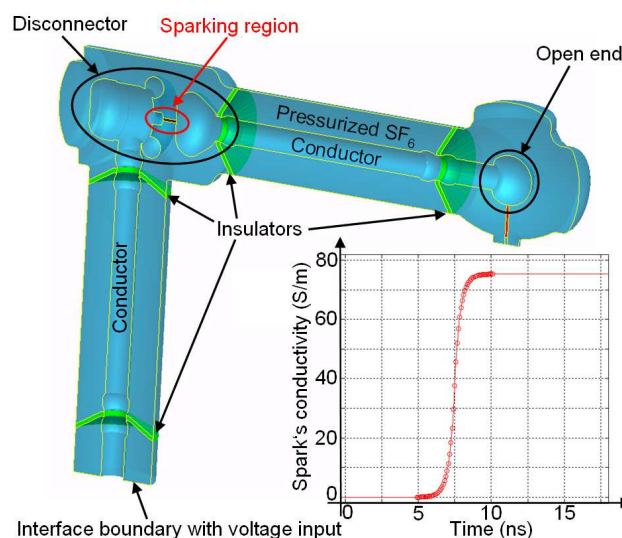


**Figure 5.52: The 3D simulation model of the new Shicky / ABB's GIS type ELK-5, 1100kV**

<sup>3</sup> Developed together with the Chinese switchgear manufacturer Xion Shiky Ltd.

The time-domain simulation followed the testing procedure of the GIS [237]. Namely, the horizontal metallic parts presented in Figure 5.52 (the tulip of the disconnecter, bus-duct, and open end) are considered to be at a floating potential because the high-voltage circuit breaker (connected to the open end) has already disconnected the service current [238]. The vertical metallic parts (the plug of the disconnecter and the adjacent bus-duct) are considered to be connected to the network. Hence they are at a potential that corresponds to the service voltage. At a certain distance between the disconnecter's plug and tulip (which is determined based on the worst-case scenario) the dielectric breakdown, i.e. electric spark occurs. This is in our simulation model represented by the abrupt but smooth time function of the electric conductivity of the cylindrical bridge (red) between the disconnecter's plug and tulip. This conductivity function is shown in Figure 5.52. The spark's rise time ( $\sim 5\text{ns}$ ) is determined by measurements [238]. The spark between the contacts of the disconnecter generates the electromagnetic waves that are propagating away from the disconnecter along the adjacent bus-ducts. Each geometrical and material discontinuity that the waves encounter along their path causes partial or total reflections of the waves. Therefore, the transient electromagnetic field within the GIS is a superposition of the large number of different electromagnetic waves and therefore has very complicated (non-harmonic) time dependence.

The results of the described time-domain simulation are presented in Figure 5.53. The electric field at the moment of time just before the spark ignition (top-left) and at three different instances after the spark ignition is visualized. To verify our results, the full-Maxwell results have been compared against the results of the circuit- equations-based EMTP-Rv simulation approach [239]) and against measurements<sup>4</sup>. This comparison is shown in Figure 5.54. To follow the VFTs testing procedure of ELK-5 the bushing was added into our simulation model. The voltage peak reached the value of 1500kV which is 35% higher than the rated voltage.

Evidently, major wave reflections are accurately computed as the number and timing of the dominant voltage peaks and dips corresponds well to the experiment. The average relative disagreement between the field simulation and experiment was 18.84%, which is acceptable, considering the geometrical complexity of the 3D real-life model, physical complexity of the phenomenon itself and anticipated measurement precision. The average error of the EMTP-Rv results was 15.66% which is slightly better than the accuracy of the field simulations. The reason for this is that the EMTP-Rv model takes into account the connected power transformer and network. However, the full-Maxwell simulations are much richer in details inside the GIS which is of paramount importance for improving design. Specifically, the voltage and field stress over the conductor surfaces and shields of GIS components are obtained by these simulations.

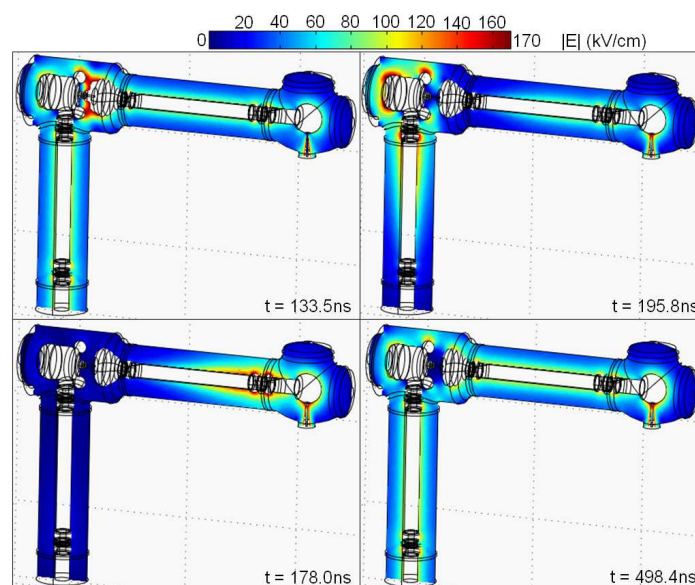


**Figure 5.53: The results of the VFT simulation of the new Shicky / ABB's GIS type ELK-5, 1100kV**

<sup>4</sup> Performed at STRI high-voltage lab. (STRI AB, Ludvika, Sweden).

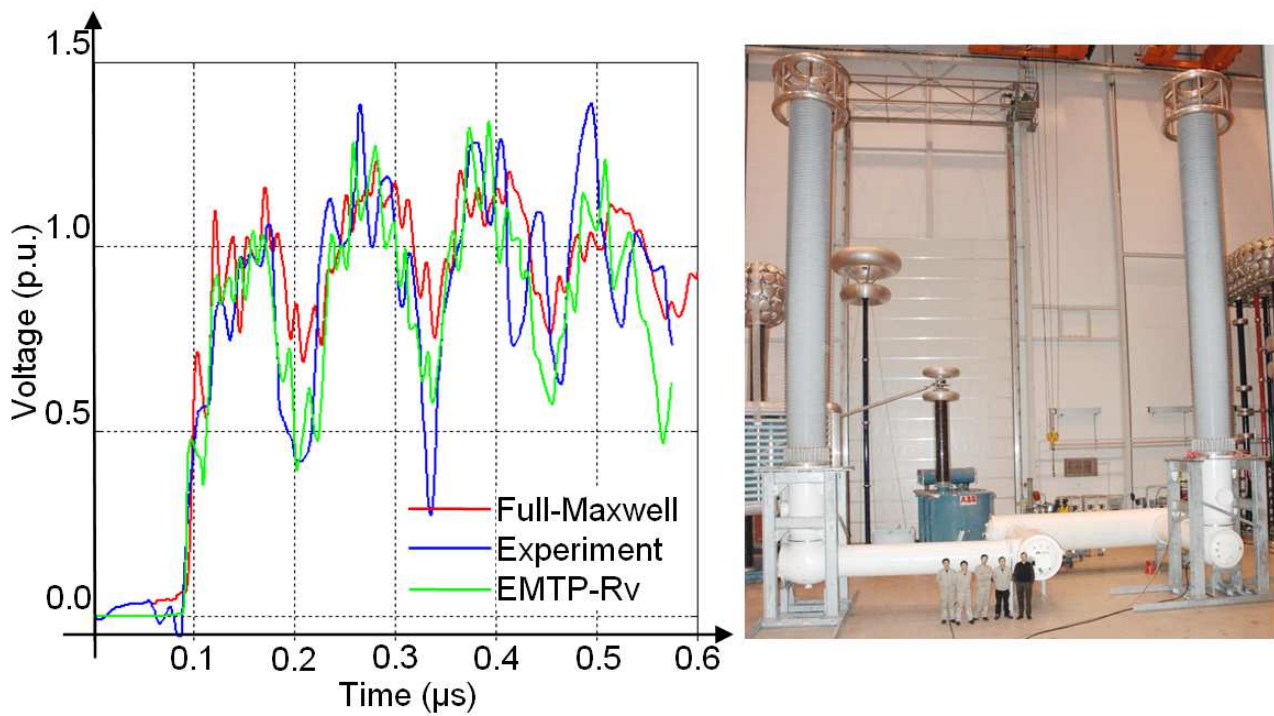


**Figure 5.54: The test set-up (right) for VFTO testing of ELK-5 and comparison of the numerical results (the voltage across the first insulator after the disconnector is compared)**

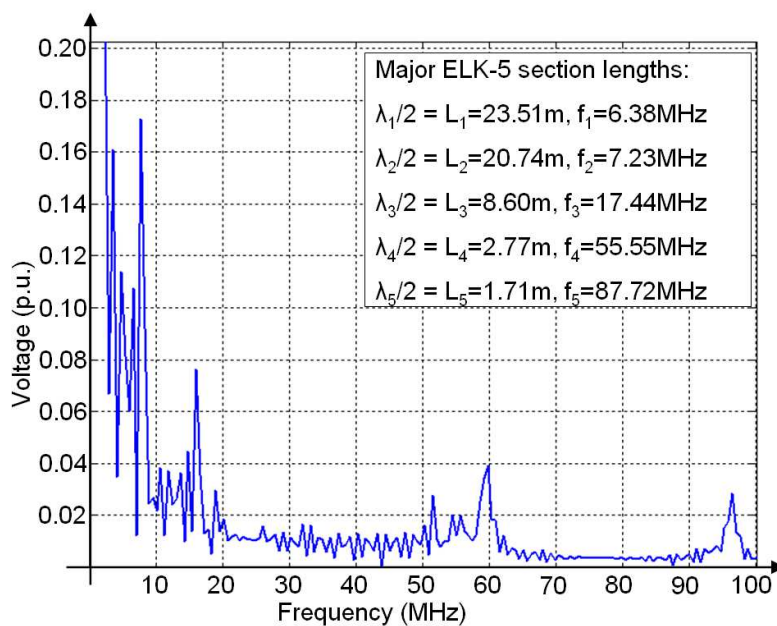


**Figure 5.55: The frequency spectrum of the VFTOs of ELK-5 that are shown in Figure 5.50**

The FFT analysis of the transient voltage presented in Figure 5.54 reveals the VFTs frequency range. This result is presented in Figure 5.55. As shown in this figure, the most dominant harmonic components of the VFTO match very well with the lengths of the main GIS sections.

The results presented in Figure 5.54 and 5.55 are obtained by solving the FEM models with around 2 million elements each. To solve such a model on a modern multi-core machine (Intel Xeon 2.5GHz, 32GB RAM) takes around 15 hours.

## 6 REPRESENTATIVE SIMULATION TOOLS

This chapter describes a non-exhaustive list of available software tools. The WG has tried to cover the majority of available simulation tools on the basis of the WG members who have expertise in terms of usage and comparison with previous developed codes, data and experimental measurements. It should be noted, however, that the approach provided by EMTP-type simulations is able to deliver satisfactory results for GIS users in order to determine the VFTO magnitude and waveshapes. Such an approach is also able to provide satisfactorily information for transformer manufactures in order to perform insulation coordination studies.

### 6.1 Numerical Electromagnetic Code (NEC)

The program was developed by Lawrence Livermore National Laboratory, US and is still under development. The NEC is based on MoM, and has been used all over the world. The program is obtained from: <http://www.ntis.gov>.

### 6.2 Virtual Surge Test Lab (VSTL)

The VSTL is developed by the Central Research Institute of Electric Power Industries (CRIEPI), Japan and is based on the FDTD. The program has been freely distributed to all the utilities in Japan and thus widely used in Japan. The VSTL can be available to an academic organisation as a royalty-free program by: <http://criepi.denken.or.jp>.

### 6.3 Parallel Finite Integral Transient Program (FIT3D-NOG/PFIT)

The program is also developed by the CRIEPI based on a finite integral technique, and is available in the same manner as the VSTL.

### 6.4 Current Distribution, Electromagnetic Fields, Grounding and Soil Structure Analysis (CDEGS)

The CDEGS is a commercial software developed by the Safe Engineering Service and Technology, Canada, that has been used for analyzing steady state and transient characteristics of a buried conductor including grounding electrodes and electromagnetic induction between a power transmission line and a gas/water pipe line. The program is based on the MoM in a frequency domain and can be found on: [www.sestech.com/products/SoftPackages/CDEGS.html](http://www.sestech.com/products/SoftPackages/CDEGS.html).

### 6.5 XFDTD

The code is developed by Remcom, US based on an FDTD method. The XFDTD is used in fields of micro-wave and harmonics propagation, scattering, and photonic in the world. The code can be obtained from: <http://www.remcom.com/xf7/>.

### 6.6 MAGNA/TDM

The code is developed by Itochu Solution Co., Japan based on an FDTD method. The program is applied to the field of antenna, waveguide, and micro-strip line, and also of an EMC field. The code can be obtained from: <http://www.engineering-eye.com/en/category/14/index.html>.

### 6.7 Transmission Line Matrix (TLM)

Transmission line matrix (TLM) is a time-domain space-discretized method in which the dynamic of the electromagnetic field is described by applying Huygens' principle. This method allows the modelling of 3-D electromagnetic structures with arbitrary geometry in a wide range of applications from electromagnetic compatibility to optics [240].



## 6.8 COMSOL (FEM)

The Comsol Multiphysics is a simulation environment produced by Comsol. It allows the integrated solution of multi-physics problems by making use of the Finite Element Method. Concerning the applications related to electromagnetics, it has a specific RF module that numerically integrates a weak-form representation of the time-domain wave equation of the magnetic vector potential [241]. More specifically, as reported in [242], the RF module covers electromagnetic fields and waves in two-dimensional and three-dimensional spaces along with traditional circuit based modelling of passive and active devices. All modelling formulations are based on Maxwell's equations or subsets and special cases of these together with material laws for propagation in various media. The RF module cover the modelling of electromagnetic fields and waves in

frequency domain, time domain, eigen-frequency and mode analysis.

## 6.9 Power Lines Lightning Performance Analysis Software (PLLP)

The PLLP is a commercial software developed by Tsinghua University, China, and has been used to analyse the lightning performance of transmission lines and distribution lines in power systems. The program is based on the leader propagation method [243] and full wave transient analysis method [244]. More details can be found on: [www.mfs-soft.com](http://www.mfs-soft.com).

## 6.10 Power System Grounding Analysis Software (PSGAS)

The PSGAS is a commercial software developed by Tsinghua University, China, and has been used for analyzing the performance of Grounding systems in substations and towers. The software includes three parts: Current Distribution, Soil Structure and Grounding Analysis. The main program is based on the MoM in a frequency domain [245]. More details can be found on: [www.mfs-soft.com](http://www.mfs-soft.com).

## 6.11 Sigma Slp

Sigma slp is a software for the determination of transmission and distribution line lightning performance, with special reference to the application of line arresters. The program is based on line-theory. More details can be found at [www.sadovic.com](http://www.sadovic.com).

# 7 CONCLUSION

This brochure has described the theory and application examples of NEA methods that are becoming powerful and effective approaches for the analysis of surge phenomena in power systems.

As known, conventional approaches for the numerical solution of surge phenomena in power systems are based on the use of EMTP-type simulation environments. These well-known approaches are based on the combined use of the transmission-line approximation integrated with the use of the circuit-theory for the representation of power systems components. In this respect, Chapter 2 has recalled the main aspects related to the implementation of the circuit-theory in EMTP-type simulation environments. In order to investigate and discuss the limits of the circuit-theory in relation to surge phenomena, Chapter 2 has also illustrated comparisons between EMTP-type and NEA simulations and field test results. The conclusion of Chapter 2 is that transients involving non-TEM propagation modes are handled with difficulties by EMTP-type approaches. However, the numerical complexity of NEA methods makes their application suitable for providing benchmark cases and to solve problems characterized by limited space domains (i.e. domains that contains a specific component like: transmission line towers, archons, grounding electrodes, breakers, transformers etc.).

In Chapter 3, the basic numerical formulation of the NEA methods has been first explained. Then various NEA methods have been classified and details of these methods have been finally described.

As NEA computations are largely dependent on the space and the time discretization, Chapter 4 has explained and discussed the computational requirements of these methods. In particular, this chapter has illustrated the link between computation resources (CPU time and memory) and the accuracy of the simulation results.

Chapter 5 has shows application examples of the NEA methods. In particular, this chapter contains applications of numerical electromagnetic computation methods to analyse electromagnetic surges to the cases listed below:

- surge characteristics of overhead transmission-line towers computed using: (i) MoM in time domain, (ii) FDTD method in time domain and (iii) PEEC methods in both frequency and time domain;
- surge characteristics of vertical grounding electrodes and horizontally-placed square-shape grounding electrodes computed using both FDTD and MoM methods;
- FDTD-computed surge characteristics of air-insulated substations;
- lightning-induced surges on overhead distribution lines computed using: MoM in frequency and time domains, 3D full-Maxwell FEMTD and FDTD method and PEEC methods in frequency domain;
- propagation characteristics of a power line carrier (PLC) along a power coaxial cable computed using the FDTD method;
- surge characteristics of a wind-turbine tower struck by lightning and its inside transient magnetic field computed using the FDTD method;
- 3D full-Maxwell FEMTD simulations of very fast transients (VFTs) in gas insulated switchgears (GIS).

As there are a few simulation environments able to implement NEA methods, Chapter 6 has summarized the representative ones that have been also used to carry out the benchmark cases illustrated in Chapter 5.

The brochure has classified the NEA methods either in time domain or in frequency domain. The latter one necessitates frequency to time transform such as Fourier transform to obtain a transient response. Also, the methods are classified by a given medium being partitioned by space or by the boundary between media.

In summary, the numerical electromagnetic analysis is an excellent tool to solve transients involving non-TEM mode propagation which is three-dimensional in general. It should be noted also that the numerical electromagnetic analysis is very useful to calculate the impedance and the admittance of a given circuit which are essential in a transient simulation by the circuit-theory approach, but often are not available. This suggests the adoption of the numerical electromagnetic analysis as a possible subroutine for calculating input data of the circuit-theory approach, when the data are not available.

As a final remark, it should be pointed out that the numerical electromagnetic analysis requires a large amount of computer resources, i.e. memory and CPU time. Also, existing NEA codes are not generally enough performing to deal with various types of transients especially concerning large networks, but - in addition to what above stated - they can also be used to appraise some 'reference' cases, which can serve as test for the adequacy of the more computationally-performing TL-based electromagnetic codes such as EMTP.

## 8 BIBLIOGRAPHY/REFERENCES

- [1] W. Scott-Meyer, EMTP Rule Book, B.P.A., 1980.4
- [2] H. W. Dommel, EMTP Theory Book, B.P.A., 1986.8
- [3] A. Ametani and T. Kawamura, A method of a lightning surge analysis recommended in Japan using EMTP, IEEE Trans. PWRD, vol.20, no.2, pp.867-875, 2005.4
- [4] A. Ametani, H. Motoyama, K. Ohkawara, H. Yamakawa and N. Suga, Electromagnetic disturbances of control circuits in power station and substation experienced in Japan, IET Proc. GTD, vol.3, no.9, pp.801-815, 2009
- [5] S. Sakaguch and M. Oyama, Application of Maxwell solvers to PD propagation Part III: PD propagation in GIS, IEEE EI Magazine, vol.19, no.1, pp.6-12, 2003

- [6] T. Mozumi, Y. Baba, M. Ishii, N. Nagaoka and A. Ametani, Numerical electromagnetic field analysis of arcon voltages during a back flashover on a 500kV twin-circuit line, IEEE Trans. PWRD, vo.18, no.1, pp.207-213, 2003.1
- [7] A. Ametani, T. Hoshino, M. Ishii, T. Noda, S. Okabe and K. Tanabe, Numerical electromagnetic analysis method and its application to surge phenomena, CIGRE 2008 General Meeting, Paper C4-108, 2008.8
- [8] IEE Japan WG, (convenor: A. Ametani), Numerical Transient Electromagnetic Analysis Methods, IEE Japan Guide Book, 2008.3
- [9] IEEE Working Group Report, A simplified method for estimating lightning performance of transmission lines, IEEE Trans., Vol. PAS-104, 919, 1985
- [10] CIGRE SC33-WG01, Guide to Procedures for Estimating Lightning Performance of Transmission Lines, Technical Brochure, Oct. 1991
- [11] IEEE Working Group Report, Estimating lightning performance of transmission lines, II-Update to analytical models', IEEE Trans., Vol. PWRD-8, 1254, 1993
- [12] IEEE Guide for Improving the Lightning Performance of Transmission Lines, IEEE Standard 1243-1997, 1997
- [13] A. Ametani, Distributed-Parameter Circuit Theory, Corona Pub. Co., Tokyo, 1990
- [14] IEE Japan WG Report, A new method of a lightning surge analysis in a power system, Technical Report No. 244, March 1987
- [15] Japanese standard, High-voltage testing method, JEC-0102-1994, IEE Japan, 1994
- [16] F. Heidler, Analytische Blitzstromfunktion zur LEMP-berechnung, Proc. of 18th ICLP, paper 1.9, pp. 63-66, Munich, Sept. 16-20, 1985
- [17] L. V. Bewley, Traveling Waves on Transmission Systems, Dover (N.Y.), 1963
- [18] M. Ishii, T. Kawamura, T. Kouno, E. Ohsaki, K. Shiokawa, K. Murotani and T. Higuchi, Multistory transmission tower model for lightning surge analysis, IEEE Trans. Power Delivery, vol.6, no.3, July, pp.1327-1335, 1991
- [19] T. Shindo and T. Suzuki, A new calculation method of breakdown voltage-time characteristics of long air gaps, IEEE Trans., Vol. PAS-104, 1556, 1985
- [20] N. Nagaoka, An archon flashover model by means of a nonlinear inductance, Trans. IEE Japan, Vol. B-111(5), 529, 1991
- [21] IEEE Working Group 3.4.11, Modeling of metal oxide surge arresters, IEEE Trans., Vol. PWRD-7(1), 302, 1992
- [22] I. Kim et al., Study of ZnO arrester model for steep front wave, IEEE Trans., Vol. PWRD-11(2), 834, 1996
- [23] P. Pinceti, M. Giannettoni, "A simplified model for zinc oxide surge arresters", IEEE Transactions on Power Delivery, vol. 14, no. 2, pp.393-398, 1999.
- [24] A. Ametani et al., Modeling of a buried conductor for an electromagnetic transient simulation, IEE Japan Trans. EEE, vol.1, no.1, pp.45-55, June 2006
- [25] R. B. Anderson and A. J. Eriksson, Lightning parameters for engineering application, Electra, No. 69, 65, 1980
- [26] S. Yokoyama, Development of lightning observation methods for current waveforms and discharge progressing manner, Asia-Pacific EMC, Beijing, China, Paper TH-PM-E1-1, April 2010.
- [27] W. Diesendorf, Insulation Co-ordination in High Voltage Electric Power Systems, Butterworths, 1974.
- [28] T. Yamada, T. Narita, T. Shioda, S. Okabe, E. Zaima, "Observation and analysis of lightning surges at substations connected with UHV designed transmission lines", IEEE Trans. Power Delivery, vol. 15, no. 2, pp. 675-683, April 2000.
- [29] T. Ueda, M. Yoda and I. Miyachi, Characteristics of lightning surges observed at 77kV substations, Trans. IEE Japan, Vol. 116-B(11), 1422, 1996
- [30] A. Ametani et al., Investigation of flashover phases in a lightning surge by new archon and tower models, Proceedings of IEEE PES T&D Conference 2002, Yokohama, pp. 1241-1246, 2002
- [31] A. Ametani et al., A frequency-dependent impedance of vertical conductors on a multiconductor tower model, IEE Proc.-GTD, Vol. 141(4), pp. 339-345, 1994



- [32] T. Hara, O. Yamamoto, M. Hayashi and C. Uesono, Empirical formulas of surge impedance for a single and multiple vertical cylinder, *Trans. IEEJ*, vol.B-110, pp.129-136, 1990
- [33] A. Ametani, et al., Wave propagation characteristics of iron conductors in an intelligent building, *Trans. IEE Japan*, Vol. 120-B(1), 31, 2000
- [34] A. Semlyen and A. Dabuleanu, Fast and accurate switching transient calculations on transmission lines with ground return using recursive convolutions, *IEEE Trans.*, Vol. PAS-95(5), 561, 1975
- [35] J. R. Marti, Accurate modeling of frequency-dependent transmission lines in electromagnetic transient simulations, *IEEE Trans.*, Vol. PAS-101(1), 147, 1982.
- [36] N. Nagaoka, Development of frequency-dependent tower model, *Trans. IEE Japan*, vol. 111-B, 51, 1991
- [37] M. Ishii and Y. Baba, Numerical electromagnetic field analysis of tower surge response, *IEEE Trans. PWRD*, vol.12, no.1, pp.483-488, Jan. 1997
- [38] A. K. Mishra, A. Ametani, Y. Baba, N. Nagaoka and S. Okabe, Nonuniform characteristics of a horizontal grounding electrode, *IEEE Trans. PWRD*, vol.22 (4), pp. 2327-2334, Oct. 2007
- [39] B.P.Gupta, B.Thapar : "Impulse Impedance of Grounding Systems", *IEEE PES Summer Power Meeting*, paper A 78563-9 (1978)
- [40] K. Tanabe, Novel method for analyzing dynamic behavior of grounding systems based on the finite-difference time-domain method, *IEEE Power Engineering Review*, vol.21, no.9, pp.55-57, 2001
- [41] L. Grcev and F. Dawalibi, An electromagnetic model for transients in power systems, *IEEE Trans.*, PWRD, vol.15, no.4, pp.1773-1781, 1990.
- [42] N. Nagaoka and A. Ametani, A lightning surge analysis considering multiphase flashovers, *IEE Japan, Research Meeting*, Paper HV-95-50, 1995. 10
- [43] CRIEPI, Visual Surge Test Lab. (VSTL), <http://criepi.denken.or.jp/jp/electric/substance/09.pdf>, 2007
- [44] A. Ametani, K. Adachi and T. Narita, An investigation of surge propagation characteristics on an 1100 kV transmission line, *IEEJ Trans. PE*, vol. 123(4), 513, 2003
- [45] J. R. Carson, Wave propagation in overhead wires with ground return, *Bell Syst. Tech. J.*, vol.5, pp539-554, 1926
- [46] F. Pollaczek, Uber das Feld einer unendlich langen wechselstromdurchflossenen Einfachleitung, *ENT*, Heft 9, Band 3, pp.339-359, July 1926
- [47] S. A. Schelkunoff, The electromagnetic theory of coaxial transmission line and cylindrical shields, *Bell Syst. Tech. J.*, Vol. 13, pp. 532-579, 1934
- [48] W. H. Wise, Propagation of high-frequency currents in ground-return circuits *Proc. IRE*, vol. 22, pp. 522, 1934
- [49] A. Ametani, T. Yoneda, Y. Baba and N. Nagaoka, An investigation of earth-return impedance between overhead and underground conductors and its approximation, *IEEE Trans. EMC*, vol.51, no.3, pp.860-867, Aug. 2009
- [50] A. Ametani, Wave propagation on a nonuniform line and its impedance and admittance, *Sci. Eng. Review*, Doshisha Univ., Vol. 43(3), 136, 2002
- [51] A. Ametani and A. Ishihara, Investigation of impedance and line parameters of a finite-length multiconductor system, *Trans. IEE Japan*, Vol. 113-B(8), 905, 1993.
- [52] A. Deri et al., The complex ground return plane : a simplified model for homogeneous and multi-layer earth return, *IEEE Trans.* Vol. PAS-100(8), 3686, 1981
- [53] L. M. Wedepohl and A. E., Wave propagation in transmission lines over lossy ground-A new complete field solution, *IEE proc.*, vol. 125(6), pp. 867-875, April 2005
- [54] A. Ametani and A. Ishihara, Impedance of a non-parallel conductor system and its circuit analysis, *IEE Japan, Research Meeting*, Paper PE-92-173, 1992. 10
- [55] M. Nakagawa, A. Ametani, and K. Iwamoto, Further studies on wave propagation in overhead lines with earth return-impedance of stratified earth, *Proc. IEE*, vol. 120(2), pp. 1521-1528, 1973
- [56] A. Ametani, Stratified effects on wave propagation, *IEEE Trans. PAS.*, vol. 93(5), pp. 1233-1239, 1974

- [57] G. C. Topp, J. L. Davis and A. P. Annan, "Electromagnetic determination of soil water content: Measurements in coaxial transmission lines", *Water Resource Reserch*, Vol. 16, No. 3, pp 574, 1980.
- [58] W. H. Wise, Potential coefficients for ground return circuits, *Bell Syst. Tech. J.*, vol. 27, pp. 365-371, 1948
- [59] M. Nakagawa, Further studies on wave propagation along overhead transmission on lines: Effect of admittance correction, *IEEE Trans. PAS*, vol. 100(7), pp. 3626-3633, 1981
- [60] F. Rachidi, S. Loyka, C. A. Nucci, and M. Ianoz, "A new expression for the ground transient resistance matrix elements of multiconductor overhead transmission lines," *Electr. Power Syst. Res. J.*, vol. 65, pp. 41–46, 2003.
- [61] M. Ohe, "A study on the Earth-Return Impedances/Admittances of Overhead and Underground Conductors", MSc. Thesis, Doshisha University, Feb. 2012, Japan, supervisor, Prof. A. Ametani.
- [62] E. Petrache, M. Paolone, F. Rachidi, C.A. Nucci, V. Rakov, M. Uman, D. Jordan, K. Rambo, J. Jerauld, M. Nyffeler, J. Schoene, "Lightning-Induced Currents in Buried Coaxial Cables: a Frequency Domain Approach and its Validation Using Rocket-Triggered Lightning", *Journal of Electrostatics*, vol. 65-5-6, May 2007, pp. 322-328.
- [63] Celia de Jusus and M. T. Correia de Barros, Modeling of corona dynamics for surge propagation studies, *IEEE Trans*, Vol, PWRD-9(3), 1564, 1994
- [64] J. F. Guiller, M. Poloujadoff and M. Rioul, Damping model of traveling waves by corona effect along extra high voltage three phase line, *IEEE Trans*. Vol. PWRD-10(4), 1851, 1995
- [65] A. Ametani, et al., A study of phase-wire voltage variations due to corona wave-deformation, *Proceeding of the IPST '99*, Budapest, Hungary, pp. 433-438, June, 1999
- [66] A. Ametani, et al., A basic investigation of substation entrance voltage variation due to corona wave deformation, *Trans. IEE Japan*, Vol. 120-B(3), 403, 2000
- [67] E. D. Sunde, *Earth Conduction Effects in Transmission Systems*, Dover Publications, New York, 1968
- [68] A. Ametani, T. Chikara, Y. Baba, N. Nagaoka and S. Okabe, A characteristic of a grounding electrode on the earth surface , *IWHV 2008/Kyoto*, Paper HV-08-76, 2008-10
- [69] A. Ametani, K. Oshio, N. Nagaoka and Y. Baba, *Lightning surge characteristics in a chemical plant*, EEUG 2010 / Helsinki, 2010.8
- [70] M. Van Baricum, and E. K. Miller, *TWTD --- A Computer Program for Time-Domain Analysis of Thin-Wire Structures*, UCRL-51-277, Lawrence Livermore Laboratory, California, 1972
- [71] R. Moini, B. Kordi and M. Abedi, Evaluation of LEMP effects on complex wire structures located above a perfectly conducting ground using electric field integral equation in time domain, *IEEE Trans. Electromagnetic Compatibility*, vol.40, no.2, May, pp.154-162, 1998
- [72] E. K. Miller, A. J. Poggio, and G. J. Burke, An integro-differential equation technique for the time-domain analysis of thin wire structures, *J. Computational Phys.*, vol. 12, pp. 24-48, 1973
- [73] H. Motoyama, K. Shinjo, Y. Matsumoto and N. Itamoto, Observation and analysis of multiphase back flashover on the Okushishiku test transmission line caused by winter lightning, *IEEE Trans. Power Delivery*, vol.13, no.4, October, pp.1391-1398, 1998
- [74] H. Motoyama, Development of a new flashover model for lightning surge analysis, *IEEE Trans. Power Delivery*, vol.11, no.2, April, pp.972-979, 1996
- [75] L. Dube and I. Bonfanti, MODELS: A new simulation tool in the EMTP, *European Trans. Electrical Power Engineering*, vol.2, no.1, January/February, pp.45-50, 1992
- [76] A. Ametani, *Distributed-Parameter Circuit Theory*, Corona Publishing Co., Ltd., 1990 (in Japanese).
- [77] A. Ametani, Y. Kasai, J. Sawada, A. Mochizuki and T. Yamada, Frequency-dependent impedance and a multiconductor tower model, *IEE Proc.-GTD.*, vol. 141, no. 4, pp. 339-345, July 1994.
- [78] A. K. Agrawal, H. J. Price and s. H. H. Gurbaxani, Transient response of multiconductor transmission lines excited by a non-uniform electromagnetic field, *IEEE Trans. Electromagn. Compat.*, vol.EMC-22, no.2, pp.119-129, 1980.
- [79] C. Paul, *Analysis of Multiconductor Transmission line*, A Wiley-Interscience Publication, John Wiley & Sons, 1994.

- [80] F. Rachidi, C. A. Nucci, M. Ianoz, and C. Mazzetti, Influence of a lossy ground on lightning-induced voltages on overhead lines, *IEEE Trans. Electromagn. Compat.*, vol. 38, no. 3, pp.250-264, Aug. 1996.
- [81] K. S. Yee, Numerical solution of initial value problems involving Maxwell's equations in isotropic media, *IEEE Trans. Antennas. Propagat.*, vol. 14, no.3, pp.302-307, May 1966.
- [82] R. Courant, K. Friedrichs, and H. Lewy, On the partial difference equations of mathematical physics, *IBM Journal*, pp.215-234, 1965 (English translation of the 1928 German original).
- [83] T. Noda and S. Yokoyama, Thin wire representation in Finite Difference Time Domain surge simulation, *IEEE Trans. Power Del.*, vol. 17, no. 3, pp.840-847, Jul. 2002.
- [84] Y. Taniguchi, Y. Baba, N. Nagaoka, and A. Ametani, An improved thin wire representation for FDTD computation, *IEEE Antennas. Propagat.*, vol. 56, no. 10, pp.3248-3252, Oct. 2008.
- [85] P. B. Johns and R. L. Beurle, "Numerical solution of 2-dimensional scattering problems using a transmission-line matrix," *Proc. Inst. Elec. Eng.*, vol. 118, no. 9, pp. 1203-1208, 1971.
- [86] P.B. Johns, "A symmetrical condensed node for the TLM method," *IEEE Trans. on Microwave Theory and Tech.*, vol. 35, no. 4, pp. 370-377, 1987.
- [87] J. A. Morente, J. A. Porte, and M. Khalladi, "Absorbing boundary conditions for the TLM method," *IEEE Trans. on Microwave Theory and Tech.*, vol. 40, no. 11, pp. 2095-2099, 1992.
- [88] Z. Chen, M. M. Ney, and W. J. R. Hoefer, "Absorbing and connecting boundary conditions for the TLM method," *IEEE Trans. on Microwave Theory and Tech.*, vol. 41, pp. 2016-2024, Nov. 1993.
- [89] N. Kukutsu and R. Konno, "Super absorption boundary condition for guided waves in the 3-D TLM simulation," *IEEE Microwave Guided Wave Lett.*, vol. 5, pp. 299-301, Sep. 1995.
- [90] C. Eswarappa, and W.J.R. Hoefer, "Implementation of Berenger absorbing boundary conditions in TLM by interfacing FDTD perfectly matched layers," *Electronics Letters*, vol. 31, no. 15, pp. 1264-1266, 1995.
- [91] N. Pena, and M. M. Ney, "Absorbing-boundary conditions using perfectly matched-layer (PML) technique for three-dimensional TLM simulations," *IEEE Trans. on Microwave Theory and Tech.*, vol. 45, no. 10 pp. 1749-1755, 1997.
- [92] Z. Shao, W. Hong, and H. Wu, "A Z-transform-based absorbing boundary conditions for 3-D TLM-SCN method," *IEEE Trans. on Microwave Theory and Tech.*, vol. 50, no. 1, pp. 222-225, 2002.
- [93] [http://www.cvel.clemson.edu/modeling/tutorials/techniques/tlm/transmission\\_line\\_matrix.html](http://www.cvel.clemson.edu/modeling/tutorials/techniques/tlm/transmission_line_matrix.html)
- [94] A. Hrennikoff, Solution of Problems of Elasticity by the Frame-Work Method, *ASME J. Appl. Mech.* 8, pp. 619-715, 1941.
- [95] R.L. Courant, Variational methods for the solution of problems of equilibrium and vibration, *Bulletin of the American Mathematical Society*, vol. 5, pp. 1-23, 1943.
- [96] A. M. Winslow, Magnetic Field Calculation in an irregular triangular mesh, Lowrence Radiation Laboratory, UCRL-7784-T, Rev. 1, Livermore, California, 1965.
- [97] P. Silvester, M. V. K. Chari, Finite element solution of saturable magnetic field problems, *IEEE Trans. On PAS*, PAS-89, pp. 1642-1651, 1970.
- [98] J. Jin, The finite element method in electromagnetics, Second Edition, John Wiley & Sons, New York, 2002.
- [99] J. C. Nedelec, Mixed Finite Elements in R3, *Numer. Math.*, Vol. 35, pp. 315-341, 1980.
- [100] H. Whitney, Geometric integration theory, Princeton University Press, Princeton, NJ, 1957.
- [101] A. Bossavit, J. C. Verite, A mixed FEM-BIEM method to solve 3-D eddy-current problems, *IEEE Trans. Magnetics*, Vol. MAG-18, pp. 431-435, 1982.
- [102] J. D. Jackson, Classical electrodynamics, John Wiley & Sons, New York, 1975.
- [103] J. Smajic, W. Halaus, J. Kostovic, U. Riechert, 3D Full-Maxwell Simulations of Very Fast Transients in GIS, Accepted for publication in *IEEE Transactions on Magnetics*, 2010.
- [104] B. Archambeault, C. Brench, and O. Rahami, *EMI/EMC Computational Modeling Handbook*, Kluwer Academic Publishers, 1998.
- [105] J. Volakis, A. Chatterjee, and L. Kempel, *Finite Element Method for Electromagnetics*, Hoboken, NJ:Wiley, 2001.

- [106] J. Webb, Edge elements and what they can do for you, *IEEE Trans. Magn.*, vol. 29, no.2, pp.1460–1465, Mar. 1993.
- [107] M. Barton and Z. Cendes, New vector finite elements for three- dimensional magnetic field computation, *J. Appl. Phys.*, vol. 61, pp.3919–3921, Apr. 1987.
- [108] J. Jin, *The finite Element Method in Electromagnetics*, Second edition. A John Wiley & Sons, Ltd., Publication, 2002.
- [109] R. Harrington, *Field Computation by Moment Methods*, Robert E. Krieger, 1987.
- [110] G. Burke, and A. Poggio, Numerical electromagnetic code (NEC)-method of moment, Technical document 116, Naval Ocean Systems Center, San Diego, 1980.
- [111] G. Burke, Numerical electromagnetic code (NEC-4)-method of moment, UCRL-MA-109338, Lawrence Livermore National Laboratory, California, 1992.
- [112] G. Mur : “Absorbing boundary conditions for the finite-difference approximation of the time-domain electromagnetic-field equation“, *IEEE Transaction on EMC*, Vol. EMC23, No.4, pp.377-382(1981)
- [113] R. L. Higdon : “Absorbing boundary conditions for difference approximations to the multi-dimensional wave equation“, *Mathematics of computation*, Vol. 47, No.176, pp.437-459(1986)
- [114] Z. P. Liao, H. L. Wong, B. P. Yang, Y. F. Yuan : “A transmitting boundary for transient wave analysis“, *Science Sinica, Series A*, Vol. 27, No. 10, pp. 1063-1076(1984)
- [115] J. P. Berenger : “Perfectly matched layer for the Absorption of electromagnetics waves“, *Journal of Computational Physics*, Vol. 114, No. 1, pp. 185-200(1994)
- [116] Z. S. Sacks, D. M. Kingsland, R. Lee, and J. F. Lee : “A perfectly matched anisotropic absorber for use an absorption boundary condition“, *IEEE Transaction on AP*, Vol. AP-44, No. 12, pp. 1460-1463(1995)
- [117] S. D. Gedney : “An isotropic perfectly matched layer-absorbing for the truncation of FDTD lattices“, *IEEE Transaction on AP*, Vol. Ap-44, No. 12, pp. 1630-1639(1996)
- [118] T. Kawamoto: “Development of Prototype Code for Three-Dimensional Electromagnetic Field Analysis Based on Finite Integration Technique- Application to Transient Analysis of Resistance for Grounding Systems –“, *CRIEPI* , No.T03025 (2004)
- [119] Sommerfeld, A. (1909), "Über Die Ausbreitung der Wellen in der Drahtlosen Telegraphie," *Annalen der Physik*, (4th Folge), Vol. 28, pp. 665-736.
- [120] Fang, D. G. Yang, J. J. and Delisle, G. Y. (1988), "Discrete Image Theory for Horizontal Electric Dipoles in a Multilayered Medium," *IEE Proceedings*, Pt. H, Vol. 135 No. 5, pp. 297-303.
- [121] Sarkar, T. K. and Pereira, O. (1995), "Using the Matrix Pencil Method to Estimate the Parameters of a Sum of Complex Exponentials," *IEEE Antennas and Propagation Magazine*, Vol. 37 No. 1, pp. 48-55.
- [122] Hua, Y. B. and Sarkar, T. K. (1989), "Generalized Pencil-of –Function Method for Extracting Poles of an EM System from Its Transient Response," *IEEE Trans. Antennas Propagat.*, Vol. 37 No. 2, pp. 229-234.
- [123] Bo Zhang, Xiang Cui, Zhibin Zhao, An Electromagnetic Approach to Analyze the Performance of the Substation’s Grounding Grid in High Frequency Domain, *COMPEL-The International Journal for Computation and Mathematics in Electrical and Electronic Engineering*, 2003, 22(3): 756-769.
- [124] P. Yutthagowith, A. Ametani, N. Nagaoka and Y. Baba., "Influence of a measuring system to a transient voltage on a vertical Conductor," *IEEJ. TEEE.*, vol. 5, no. 2, Mar. 2010.
- [125] P. Yutthagowith, A. Ametani, N. Nagaoka, and Y. Baba., "Lightning induced voltage over lossy ground by a hybrid electromagnetic-circuit model method with Cooray-Rubinstein formula," *IEEE Trans. Electromagn. Compat.*, vol. 51, no. 4, pp.975-985, Nov. 2009.
- [126] P. Yutthagowith, A. Ametani, N. Nagaoka, and Y. Baba., "Application of the partial element equivalent circuit method to analysis of transient potential rises in grounding systems," *IEEE Trans. Electromagn. Compat.*, vol. 53, no. 3, pp.726-736, Aug. 2011.

- [127] P. Yutthagowith, A. Ametani, N. Nagaoka, and Y. Baba., "Application of a partial element equivalent circuit method to lightning surge analyses," in *Proc. Conf. Asia-pacific on lightning protection*, pp. 809-812, Oct. 2011.
- [128] Shunchao Wang; Jinliang He; Bo Zhang; Rong Zeng; Zhanqing Yu; , "A Time-Domain Multiport Model of Thin-Wire System for Lightning Transient Simulation," *IEEE Transactions on Electromagnetic Compatibility*, vol.52, no.1, pp.128-135, Feb. 2010.
- [129] Shunchao Wang; Jinliang He; Bo Zhang; Rong Zeng, "Time-Domain Simulation of Small Thin-Wire Structures Above and Buried in Lossy Ground Using Generalized Modified Mesh Current Method," *IEEE Transactions on Power Delivery*, vol.53, no.1, Jan, 2011.
- [130] J. Mosig, "Arbitrarily shaped microstrip structures and their analysis with a mixed potential integral equation," *IEEE Trans. Microw. Theory Tech.*, vol. 36, no. 2, pp. 314–323, Feb 1988.
- [131] Mazzettie C, Veca G M. Impulse Behaviour of Grounding Electrodes. *IEEE Transactions on Power Apparatus and Systems*, Vol.102, N o.9, 1983, pp. 3148-3154
- [132] Liew A C, Darveniza M. Dynamic Model of Impulse Characteristics of Concentrated Earth. *Proc. IEE*, Vol.121, No.2, 1974, pp.123-135
- [133] Geri A, Garbagnati E, Veca G M, et al. Non-linear Behaviour of Ground Electrodes Under Lightning Surge Currents: Computer Modelling and Comparison with Experimental Results. *IEEE Transactions on Magnetism*, Vol.28, No.2, 1992, pp. 1442-1445
- [134] Leonid D G, Markus Heimbach. Frequency Dependent and Transiet Characteristics of Substation Grounding Systems. *IEEE Transactions on Power Delivery*, Vol.12, No.1 1997, pp. 172-178
- [135] Dawalibi F, Xiong W and Jinxi Ma. Transient Performance of Substation Structures and Associated Grounding Systems. *IEEE Transactions on Industry Applications*, Vol.31, No.3, 1995, pp. 520-527
- [136] M. Mousa, The Soil Ionization Gradient Associated with Discharge of High Currents into Concentrated Electrodes. *IEEE Transactions on Power Delivery*, Vol.9, No.3, July 1994, pp.1669-1677
- [137] H. G. Ufer, "Investigation and Testing of Footing-Type Grounding Electrodes for Electrical Installations", *IEEE Trans. Power Apparatus and Systems*, Vol. 83, pp. 1024-1048, 1964.
- [138] Gao, YQ, He, JL, Zou, J, et al. Fractal simulation of soil breakdown under lightning current. *JOURNAL OF ELECTROSTATICS*, 2004, 61 (3-4): 197-207
- [139] J. L. He, Y. Q. Gao, R. Zeng, J. Zou, X. D. Liang, J. B. Lee, S. H. Chang, "Effective length of counterpoise wire under lightning current," *IEEE Trans. Power Del.*, vol.20, no.2, pp. 1585-1591 April 2005.
- [140] Rong Zeng, Peng Kang, Bo Zhang, Jinliang He. Lightning Transient Performances Analysis of Substation Based on Complete Transmission Line Model of Power Network and Grounding Systems. *IEEE Transactions on Magnetism*, vol.42, no.4, pp.875-878, April 2006.
- [141] E. D. Sunde, "Earth Conduction Effects in Transmission System," New York: Dover Publication, Inc., 1949.
- [142] R. F. Harrington, *Field Computation by Moment Methods*, Macmillan Co., New York, 1968.
- [143] K. S. Yee, Numerical solution of initial boundary value problems involving Maxwell's equations in isotropic media, *IEEE Trans. Antennas and Propagation*, vol. 14, no. 8, pp. 302-307, May 1966.
- [144] T. Mozumi, Y. Baba, M. Ishii, N. Nagaoka, and A. Ametani, Numerical electromagnetic field analysis of archorn voltages during a back-flashover on a 500 kV twin-circuit line, *IEEE Trans. Power Delivery*, vol. 18, no. 1, pp. 207-213, Jan. 2003.
- [145] M. Van Blaricum and E. K. Miller, TWTD --- A computer program for time-domain analysis of thin-wire structures, Lawrence Livermore Lab., Tech. Rep. UCRL-51 277, 1972.
- [146] H. Motoyama, Development of a new flashover model for lightning surge analysis, *IEEE Trans. Power Delivery*, vol. 11, pp. 972–979, April 1996.
- [147] W. Scott-Meyer, *EMTP Rule Book*, Bonneville Power Administration, Portland, Oregon, 1977.
- [148] M. Ishii, T. Kawamura, T. Kouno, E. Ohsaki, K. Shiokawa, K. Murotani, and T. Higuchi, Multistory transmission tower model for lightning surge analysis, *IEEE Trans. Power Delivery*, vol. 6, no. 3, pp. 1327-1335, April 1991.



- [149] T. Noda, "A tower model for lightning overvoltage studies based on the result of an FDTD simulation," IEEJ Trans. Power and Energy, vol. 127-B, no. 2, pp. 379-388, Feb. 2007 (in Japanese).
- [150] P. Yutthagowith, A. Ametani, N. Nagaoka and Y. Baba, Application of the partial element equivalent circuit method to tower surge response calculations, IEEJ Trans. EEE., vol. 6, no. 4, July. 2011. (in press)
- [151] S. Visacro, and A. Soares, HEM: a model for simulation of lightning-related engineering problems, IEEE Trans. Power Delivery, vol. 20, no. 2, pp. 1206-1208, April 2005.
- [152] K. Tanabe, Novel method for analyzing dynamic behavior of grounding systems based on the finite-difference time-domain method, IEEE Power Engineering Review, vol. 21, no. 9, pp. 55-57, Sep. 2001.
- [153] K. Tanabe, A. Asakawa, M. Sakae, M. Wada, and H. Sugimoto, Verifying the computational method of transient performance with respect to grounding systems based on the FD-TD method, IEEJ Trans. Power and Energy, vol. 123, no. 3, pp. 358-367, Mar. 2003.
- [154] S. Miyazaki, and M. Ishii, Analysis of transient response of grounding system based on moment method, Paper presented at ISH 2005, Beijing, China, Aug. 2005.
- [155] Y. Baba, N. Nagaoka, and A. Ametani, Modeling of thin wires in a lossy medium for FDTD simulations, IEEE Trans. Electromagnetic Compatibility, vol. 47, no. 1, pp. 54-60, Feb. 2005.
- [156] L. D. Grcev, Computer analysis of transient voltages in large grounding systems, IEEE Trans. Power Delivery, vol. 11, no. 2, pp. 815-823, April 1996.
- [157] G. Ala, P. L. Buccheri, P. Romano, and F. Viola, Finite difference time domain simulation of earth electrodes soil ionisation under lightning surge condition, IET Science, Measurement and Technology, vol. 2, no. 3, pp. 134-145, 2008.
- [158] M. Darveniza, and A. C. Liew, Dynamic model of impulse characteristic of concentrated earths, Proc. IEE, vol. 121, no. 2, pp. 123-135, Feb. 1974.
- [159] Oettle E E, "A new estimation curve for predicting the impulse impedance of concentrated earth electrodes," IEEE Trans. Power Delivery, Vol. 3, No. 4, pp. 2020-2029, 1988.
- [160] Leonid D G, Markus Heimbach, "Frequency dependent and transient characteristics of substation grounding systems," IEEE Trans. Power Delivery, Vol. 12, No. 1, pp. 172-178, 1997
- [161] Geri, "Behaviour of grounding systems excited by high impulse currents: the model and its validation," IEEE Trans. Power Delivery, Vol. 14, No. 3, pp. 1008-1017, July 1999.
- [162] Jinliang He, Rong Zeng, Youping Tu, et al. "Laboratory investigation of impulse characteristics of transmission tower grounding devices," IEEE Trans. Power Delivery, Vol. 18, No. 3, July 2003
- [163] ZENG Rong, He Jinliang, Zhang Bo, et al. Lightning electromagnetic field generated by grounding electrode considering soil ionization. Progress in Natural Science, 2006, 16(9): 1002-1006+F44
- [164] Zhang, B, He, JL, Lee, JB, et al. Numerical analysis of transient performance of grounding systems considering soil ionization by coupling moment method with circuit theory. IEEE TRANSACTIONS ON MAGNETICS, 2005, 41 (5): 1440-1443
- [165] Bo Zhang, Jinliang He, Rong Zeng, and Jun Zou. Electromagnetic fields around buildings during near field lightning strokes. VIII International Symposium on Lightning Protection, São Paulo, Brazil, 21st-25th November 2005, pp. 582-586
- [166] T. Watanabe, K. Fukui, H. Motoyama, and T. Noda, The measurement and analysis of surge characteristics using miniature model of air insulated substation, Paper presented at IPST 2005, Montreal, Canada, June 2005.
- [167] R. M. S. de Oliveira, and C. L. S. Souza Sobrinho, Computational environment for simulating lightning strokes in a power substation by finite-difference time-domain method, IEEE Trans. Electromagnetic Compatibility, vol. 51, no. 4, pp. 995-1000, Nov. 2009.
- [168] Rong Zeng, Peng Kang, Bo Zhang, Jinliang He. Lightning Transient Performances Analysis of Substation Based on Complete Transmission Line Model of Power Network and Grounding Systems. IEEE Transactions on Magnetics, vol.42, no.4, pp.875-878, April 2006.
- [169] Working Group, "Modeling of metal oxide surge arresters," IEEE Trans. Power Del., vol. 7, pp. 301-309, Jan. 1992.

- [170] Z. J. Wang, "A model for transient analysis in large transformer windings," *Journal of Tsinghua Univ. (Sci. & Tech.)*, vol.32, no.1, pp.25-32, 1996.
- [171] X. Legrand, A. Xemard, P. Auriol, C. A. Nucci, C. Mouychard, "Modeling of Substation grounding for fast front over-voltages studies", IPST 2007, Lyon, France.
- [172] R. K. Pokharel, M. Ishii, and Y. Baba, Numerical electromagnetic analysis of lightning-induced voltage over ground of finite conductivity, *IEEE Trans. Electromagnetic Compatibility*, vol. 45, no. 4, pp. 651-656, Nov. 2003.
- [173] M. Ishii, K. Michishita, and Y. Hongo, Experimental study of lightning-induced voltage on an overhead wire over lossy ground, *IEEE Trans. Electromagnetic Compatibility*, vol. 41, no. 1, pp. 39-45, Jan. 1999.
- [174] A. K. Agrawal, H. J. Price, and H. H. Gurbaxani, Transient response of multiconductor transmission lines excited by a nonuniform electromagnetic field, *IEEE Trans. Electromagnetic Compatibility*, vol. 22, no. 2, pp. 119-129, May 1980.
- [175] Y. Baba, and V. A. Rakov, Voltages induced on an overhead wire by lightning strikes to a nearby tall grounded object, *IEEE Trans. Electromagnetic Compatibility*, vol. 48, no. 1, pp. 212-224, Feb. 2006.
- [176] F. H. Silveira, S. Visacro, J. Herrera, and H. Torres, Evaluation of lightning-induced voltages over a lossy ground by the hybrid electromagnetic model, *IEEE Trans. Electromagnetic Compatibility*, vol. 51, no. 1, pp. 156-160, Feb. 2009.
- [177] P. Yutthagowith, A. Ametani, N. Nagaoka, and Y. Baba, Lightning-induced voltage over lossy ground by a hybrid electromagnetic circuit model method with Cooray-Rubinstein formula, *IEEE Trans. Electromagnetic Compatibility*, vol. 51, no. 4, pp. 975-985, Nov. 2009.
- [178] A. E. Ruehli, Equivalent circuit models for three-dimensional multiconductor systems, *IEEE Trans. Microwave Theory and Technology*, vol. 22, no. 3, pp.216-221, Mar. 1974.
- [179] K. Michishita, M. Ishii, A. Asakawa, S. Yokoyama and K. Kami, Voltage induced on a test distribution line by negative winter lightning strokes to a tall structure, *IEEE Trans. Electromagn. Compat.*, vol. 45, no. 1, pp.135-140, Jan. 2003.
- [180] R. K. Pokharel, and M. Ishii, Applications of time-domain numerical electromagnetic code to lightning surge analysis, *IEEE Trans. Electromagnetic Compatibility*, vol. 49, no. 3, pp. 623-631, Aug. 2007.
- [181] R. Moini, B. Kordi, and M. Abedi, Evaluation of LEMP effects on complex wire structures located above a perfectly conducting ground using electric field integral equation in time domain, *IEEE Trans. Electromagnetic Compatibility*, vol. 40, no. 2, pp. 154-162, May 1998.
- [182] F. Napolitano, A. Borghetti, C. A. Nucci, M. Paolone and F. Rachidi, "Use of the Full-Wave Finite Element Method for the Numerical Electromagnetic Analysis of LEMP and its Coupling with Overhead Lines", *Proc. of the 7th Asia-Pacific International Conference on Lightning*, Nov. 1-4, 2011, Chengdu, China.
- [183] V. A. Rakov and M. A. Uman, *Lightning: Physics and Effects*. Cambridge, MA: Cambridge Univ. Press, 2003.
- [184] V. Cooray, "Mathematical modeling of return strokes," in *The Lightning Flash: Physical and Engineering Aspects*, V. Cooray, Ed. London, U.K.: IEE Press, 2003.
- [185] M. J. Master and M. A. Uman, "Transient electric and magnetic fields associated with establishing a finite electrostatic dipole," *Amer. J. Phys.*, vol. 51, pp. 118-126, 1983.
- [186] M. Rubinstein and M. A. Uman, "Methods for calculating the electromagnetic fields from a known source distribution: Application to lightning," *IEEE Trans. on EMC*, vol. 31-2, pp. 183-189, May 1989.
- [187] V. Cooray, "Horizontal fields generated by return strokes," *Radio Sci.*, vol. 27, pp. 529-537, 1992.
- [188] M. Rubinstein, "An approximate formula for the calculation of the horizontal electric field from lightning at close, intermediate, and long range," *IEEE Trans. on EMC*, vol. 38-3, pp. 531-535, Aug. 1996.
- [189] V. Cooray, "Some considerations on the 'Cooray-Rubinstein' approximation used in deriving the horizontal electric field over finitely conducting ground," *IEEE Trans. on EMC*, vol. 44-4, pp. 560-566, Nov. 2002.

- [190] F. Delfino, R. Procopio, and M. Rossi, "Lightning return stroke current radiation in presence of a conducting ground: 1. Theory and numerical evaluation of the electromagnetic fields," *J. Geophys. Res.*, vol. 113, pp. D05110-1–D05110-10, 2008.
- [191] F. Delfino, R. Procopio, M. Rossi, F. Rachidi, and C.A. Nucci, "Lightning return stroke current radiation in presence of a conducting ground: 2. Validity assessment of simplified approaches," *J. Geophys. Res.*, vol. 113, pp. 1–11, 2008.
- [192] A. Sommerfeld, "Über die ausbreitung der wellen in der drahtlosen telegraphie," *Ann. Phys.*, vol. 28, pp. 665–665, 1909.
- [193] A. Banos, "Dipole radiation in the presence of a conducting half-space", Pergamon Press, 1966.
- [194] C. Leteinturier, "Champ électromagnétique émis par une décharge orageuse: modèle théorique intégrant les variations de la résistivité du sol", Centre national d'étude de télécommunications, Note technique NT/LAA/RLM/66, Nov. 1980.
- [195] A. S. Podgorski and J. A. Landt, "Three dimensional time domain modeling of lightning," *IEEE Trans. on PWRD*, vol. 2-3, pp. 931–938, Jul. 1987.
- [196] R. Moini, B. Kordi, G. Z. Rafi, and V. A. Rakov, "A new lightning return stroke model based on antenna theory," *J. Geophys. Res.*, vol. 105, pp. 29693–29702, 2000.
- [197] Y. Baba and M. Ishii, "Numerical electromagnetic field analysis of lightning current in tall structures," *IEEE Trans. on PWRD*, vol. 16-2, pp. 324–328, Apr. 2001.
- [198] C. A. F. Sartori and J. R. Cardoso, "An analytical-FDTD method for near LEMP calculation," *IEEE Trans. on Magn.*, vol. 36-4, pp. 1631–1634, Jul. 2000.
- [199] C. Yang and B. Zhou, "Calculation methods of electromagnetic fields very close to lightning," *IEEE Trans. on EMC*, vol. 46-1, pp. 133–141, Feb. 2004.
- [200] Y. Baba and V. A. Rakov, "On the mechanism of attenuation of current waves propagating along a vertical perfectly conducting wire above ground: Application to lightning," *IEEE Trans. on EMC*, vol. 47-3, pp. 521–532, Aug. 2005.
- [201] A. Mimouni, F. Rachidi, Z. Azzouz, "A finite-difference time-domain approach for the evaluation of electromagnetic fields radiated by lightning to tall structures," *J. of Electrostatics*, vol. 866, pp. 504–513, 2008.
- [202] J.-M. Jin, D. J. Riley, *Finite element analysis of antenna and arrays*, John Wiley & Sons, inc., 2009.
- [203] A.K. Agrawal, H.J. Price, S.H. Gurbaxani, "Transient response of a multiconductor transmission line excited by a nonuniform electromagnetic field", *IEEE Trans. on EMC*, vol. 22-2, pp. 119-129, May 1980.
- [204] C. A. Nucci, F. Rachidi, M. Ianoz, and C. Mazzetti, "Lightning-induced overvoltages on overhead lines," *IEEE Trans. on EMC*, vol. 35-1, pp. 75–86, Feb. 1993.
- [205] F. Rachidi, C. A. Nucci, M. Ianoz, and C. Mazzetti, "Calculation of lightning-induced voltages on an overhead line over a homogeneous lossy ground," *IEEE Trans. on EMC*, vol. 38-3, pp. 250–264, Aug. 1996.
- [206] C. A. Nucci and F. Rachidi, "Interaction of electromagnetic fields generated by lightning with overhead electrical networks," in *The Lightning Flash*. London, U.K.: IEE Press, 2003, pp. 425–478.
- [207] RF Module User's Guide, October 2010, COMSOL AB.
- [208] R. Thottappillil, "Computation of electromagnetic fields from lightning discharge," in *The Lightning Flash: Physical and Engineering Aspects*, V. Cooray, Ed. London, U.K.: IEE Press.
- [209] V. Cooray and G. Cooray, "The Electromagnetic Fields of an Accelerating Charge: Applications in Lightning Return-Stroke Models", *IEEE Trans. on EMC*, vol. 52-2, pp. 944-955, Nov. 2010.
- [210] P. Degauque, "Current and voltage induced on telecommunications cable by a lightning return stroke," in *Lightning Electromagnetics*, R. L. Gardner, Ed. New York: Hemisphere, 1990, pp. 377–440.
- [211] A. Shoory, F. Rachidi, M. Rubinstein, R. Thottappillil, "On the Measurement and Calculation of Horizontal Electric Fields From Lightning", *IEEE Trans. on EMC*, vol. 53, no. 3, pp. 792-801, 2011.
- [212] J. R. Wait, "Concerning the horizontal electric field of lightning," *IEEE Trans. Electromagn. Compat.*, vol. 39, no. 2, p. 186, May 1997.



- [213] F. Rachidi, C. A. Nucci, M. Ianoz, and C. Mazzetti, "Importance of losses in the determination of lightning-induced voltages on overhead lines," *Int. Symp. Electromagn. Compat.*, Rome, Italy, 1996.
- [214] F. Rachidi, C.A. Nucci, M. Ianoz, "Transient analysis of multiconductor lines above a lossy ground", *IEEE Transactions on Power Delivery*, Vol. 14 , No. 1, pp. 294 – 302, January 1999 ,
- [215] M. Van Baricum, and E. K. Miller, "TWTD --- A Computer Program for Time-Domain Analysis of Thin-Wire Structures," UCRL-51-277, Lawrence Livermore Laboratory, California, 1972.
- [216] E. K. Miller, A. J. Poggio, and G. J. Burke, "An integro-differential equation technique for the time-domain analysis of thin wire structures," *J. Computational Phys.*, vol. 12, pp. 24-48, 1973.
- [217] A. S. Podgorski, and J. A. Landt, "Three dimensional time domain modeling of lightning," *IEEE Trans. Power Delivery*, vol. PWRD-2, no. 3, pp.931-938, July, 1987.
- [218] R. F. Harrington, "Field Computation by Moment Methods," Macmillan Co., New York, 1968.
- [219] G. J. Burke, and A. J. Poggio, "Numerical Electromagnetic Code (NEC) --- Method of Moments," Technical Document 116, Naval Ocean Systems Center, San Diego, 1980.
- [220] G. J. Burke, "Numerical Electromagnetic Code (NEC-4) --- Method of Moments," UCRL-MA-109338, Lawrence Livermore National Laboratory, California, 1992.
- [221] K. S. Yee, "Numerical solution of initial boundary value problems involving Maxwell's equations in isotropic media," *IEEE Trans. Antennas Propagat.*, vol. AP-14, no. 3, pp. 302-307, March, 1966.
- [222] T. Noda, A. Tatematsu, and S. Yokoyama, "Improvements of an FDTD-based surge simulation code and its application to the lightning overvoltage calculation of a transmission tower," *IPST05-138-24c*, Montreal, Canada, June 2005.
- [223] F. Heidler, "Analytische blitzstromfunktion zur LEMP-berechnung," in *Proc. 18th Int. Conf. Lightning Protection*, Munich, Germany, paper 1.9, pp 63–66, Sept. 1985.
- [224] C. A. Nucci, C. Mazzetti, F. Rachidi, and M. Ianoz, "On lightning return stroke models for LEMP calculations", *Proc. of the 19th Int. Conf. on Lightning Protection (ICLP)*, Graz, Austria, 1988.
- [225] V. Cooray, "Horizontal Electric Field Above- and Underground Produced by Lightning Flashes", *IEEE Trans. on EMC*, vol. 52-4, pp. 936-943, Nov. 2010.
- [226] Jinliang He, Yu Li, Rong Zeng, Bo Zhang, Weiguang Zhuo, Lichuan Wang, Yurong Deng. Lightning Performances of Transmission Lines Based on Whole Transmission Line Model. *The 28th International Conference on Lightning Protection*, Sept. 18-22, 2005, Kanazawa, Japan. Paper no.1138.
- [227] N. Okazima, Y. Baba, N. Nagaoka, A. Ametani, K. Temma, and T. Shimomura, Propagation characteristics of power line communication signals along a power cable having semiconducting layers, *IEEE Trans. Electromagnetic Compatibility*. (in press)
- [228] K. Yamamoto, T. Noda, S. Yokoyama and A. Ametani, Experimental and Analytical Studies of Lightning Overvoltages in Wind Turbine Generator Systems, *Electric Power Systems Research*, Vol. 79, Issue 3, pp. 436-442, ISSN:0378-7796, Mar. 2009.
- [229] K. Yamamoto, S. Yanagawa, K. Yamabuki, S. Sekioka and S. Yokoyama, Analytical Surveys of Transient and Frequency Dependent Grounding Characteristics of a Wind Turbine Generator System on the Basis of Field Tests, *IEEE Trans. on Power Delivery*, Vol. 25, Issue: 4, pp: 3035 – 3043, Oct. 2010.
- [230] A. Ametani and K. Yamamoto, A Study of Transient Magnetic Fields in a Wind Turbine Nacelle, *WE-AM-E2-5*, 2010 APEMC-Beijing – Symposium & Technical Exhibition, April 2010.
- [231] J. Meppelnik, K. Diederich, K. Feser, W. Pfaff, Very Fast Transients in GIS, *IEEE Transactions on Power Delivery*, Vol. 4, No. 1., pp. 223 - 233, 1989.
- [232] D. Povh, H. Schmitt, O. Völcker, R. Witzmann, Modelling and Analysis Guidelines for Very Fast Transients, *IEEE Transactions on Power Delivery*, Vol. 11, No. 4, pp. 2028 – 2035, 1996.
- [233] CIGRE Report, Guidelines for Representation of Network Elements when Calculating Transients, Working Group 02 of Study Comitee 33, Paris, 2000.
- [234] Y. Shu, "China Builds UHV Grid" in "Transmission & DistributionWorld", March 2007.  
[http://tdworld.com/overhead\\_transmission/power\\_china\\_uhv\\_grid/](http://tdworld.com/overhead_transmission/power_china_uhv_grid/)

- [235] COMSOL Multiphysics, [www.comsol.com](http://www.comsol.com).
- [236] J. Jin, The Finite Element Method in Electromagnetics, 2nd Edition, Wiley-IEEE Press, New York, 2002.
- [237] IEC 62271-203, "High-Voltage Switchgear and Controlgear", International Electrotechnical Commission, Geneva, Switzerland, 2003.
- [238] J. Smajic, W. Halaus, J. Kostovic, U. Riechert, 3D Full-Maxwell Simulations of Very Fast Transients in GIS, Accepted for publication in IEEE Transactions on Magnetics, 2010.
- [239] EMTP RV, EM transient program, <http://www.emtp.com>.
- [240] F. Rachidi and S. Tkachenko, Electromagnetic Field Interaction with Transmission Lines : From Classical Theory to HF Radiation Effects, WIT Press, Boston (USA), 2008.
- [241] J.-M. Jin, D. J. Riley, Finite element analysis of antenna and arrays, John Wiley & Sons, inc., 2009.
- [242] RF Module User's Guide, October 2010, COMSOL AB.
- [243] Jinliang He, Youping Tu, Rong Zeng, Jaebok Lee, Sughun Chang, Zhicheng Guan, "Numerical Analysis Model for Shielding Failure of Transmission Line under Lightning Stroke," IEEE Transactions on Power Delivery, vol.20, no.2, pp. 815-822, April 2005.
- [244] Shunchao Wang, Jinliang He, Bo Zhang, and Rong Zeng, "Time-Domain Simulation of Small Thin-Wire Structures Above and Buried in Lossy Ground Using Generalized Modified Mesh Current Method," IEEE Transaction on Power Delivery, vol.26, no.1, pp. 369-377, Jan. 2011.
- [245] Bo Zhang, Xiang Cui, Zhibin Zhao, Jinliang He, and Lin Li, "Numerical Analysis of the Influence Between Large Grounding Grids and Two-End Grounded Cables by the Moment Method Coupled With Circuit Equations," IEEE Transactions on Power Delivery, vol.20, no.2, pp. 731-737, April 2005.